

AD-A201 269

FILE COPY

ARO 21177.2 PH

(2)

OPTICALLY CONTROLLED ATTACHMENT STUDIES
FOR DIFFUSE DISCHARGE SWITCH APPLICATIONS

FINAL REPORT

P. J. CHANTRY, C. B. FREIDHOFF, C. L. CHEN, D. K. DAVIES,
and L. E. KLINE.

JUNE 1988

U. S. ARMY RESEARCH OFFICE

CONTRACT NO. DAAG29-84C-0003

WESTINGHOUSE R & D CENTER

APPROVED FOR PUBLIC RELEASE; DISTRIBUTION UNLIMITED.

DTIC
SELECTED
OCT 19 1988
S H D

68 10 2000

THE VIEWS, OPINIONS, AND/OR FINDINGS CONTAINED IN THIS REPORT ARE THOSE OF THE AUTHOR(S) AND SHOULD NOT BE CONSTRUED AS AN OFFICIAL DEPARTMENT OF THE ARMY POSITION, POLICY, OR DECISION, UNLESS SO DESIGNATED IN THE DOCUMENTATION.

UNCLASSIFIED
SECURITY CLASSIFICATION OF THIS PAGE

ADA 201269

REPORT DOCUMENTATION PAGE

1a. REPORT SECURITY CLASSIFICATION Unclassified		1b. RESTRICTIVE MARKINGS	
2a. SECURITY CLASSIFICATION AUTHORITY		3. DISTRIBUTION/AVAILABILITY OF REPORT Approved for public release; distribution unlimited.	
2b. DECLASSIFICATION/DOWNGRADING SCHEDULE		5. MONITORING ORGANIZATION REPORT NUMBER(S) ARO 21177-2-PH	
4. PERFORMING ORGANIZATION REPORT NUMBER(S)		7a. NAME OF PERFORMING ORGANIZATION Westinghouse R&D Center	
6a. NAME OF PERFORMING ORGANIZATION Westinghouse R&D Center	6b. OFFICE SYMBOL (If applicable)	7b. ADDRESS (City, State, and ZIP Code) 110 Beulah Road Pittsburgh, PA 15235	
8a. NAME OF FUNDING/SPONSORING ORGANIZATION U. S. Army Research Office	8b. OFFICE SYMBOL (If applicable)	9. PROCUREMENT INSTRUMENT IDENTIFICATION NUMBER DAAG629-84-C-0003	
8c. ADDRESS (City, State, and ZIP Code) P. O. Box 12211 Research Triangle Park, NC 27709-2211	10. SOURCE OF FUNDING NUMBERS		PROGRAM ELEMENT NO.
			PROJECT NO.
			TASK NO.
11. TITLE (Include Security Classification) OPTICALLY CONTROLLED ATTACHMENT STUDIES FOR DIFFUSE DISCHARGE SWITCH APPLICATIONS. (Unclassified)			
12. PERSONAL AUTHOR(S) P. J. Chantry, C. B. Freidhoff, C. L. Chen, D. K. Davies, L. E. Kline			
13a. TYPE OF REPORT Final	13b. TIME COVERED FROM 84-4-15 TO 88-3-31	14. DATE OF REPORT (Year, Month, Day) 88-8-5	15. PAGE COUNT 138
16. SUPPLEMENTARY NOTATION The view, opinions and/or findings contained in this report are those of the author(s) and should not be construed as an official Department of the Army position, policy, or decision unless so designated by other documentation.			
17. COSATI CODES		18. SUBJECT TERMS (Continue on reverse if necessary and identify by block number) Diffuse, Discharge, Switch, Attachment, Enhancement, Optical, Main, Gas	
19. ABSTRACT (Continue on reverse if necessary and identify by block number) The generic properties required of the gas medium of a diffuse discharge switch are reviewed, and applied to the selection of a suitable main gas, CH_4 , and a number of candidate attaching gas additives for increasing the rate of recovery of the switch. The constraints placed on the latter choice include the possibility that the attachment cross section be susceptible to optical enhancement by IR irradiation using a CO_2 laser. Based on a literature survey of available gases whose infrared absorption spectra overlap the output spectrum of efficient CO_2 lasers, we selected four gases for further experimental study. Two of the gases chosen, perfluoropropane (C_3F_8), and vinyl chloride ($\text{C}_2\text{H}_3\text{Cl}$), were known to have desirable attachment cross section shapes, but their cross section magnitudes were uncertain, and their temperature sensitivity unknown. In the present work we have determined that the room temperature total attachment cross section of C_3F_8 peaks at 2.8 eV with a value of $1.75 \times 10^{-17} \text{ cm}^2$. This is 14 times smaller than the only other measurement of this type we are aware of (Kurepa, 1965). There is much better agreement with two more recently reported			
20. DISTRIBUTION/AVAILABILITY OF ABSTRACT <input type="checkbox"/> UNCLASSIFIED/UNLIMITED <input type="checkbox"/> SAME AS RPT <input type="checkbox"/> DTIC USERS		21. ABSTRACT SECURITY CLASSIFICATION Unclassified	
22a. NAME OF RESPONSIBLE INDIVIDUAL A		22b. TELEPHONE (Include Area Code)	22c. OFFICE SYMBOL

DD FORM 1473, 84 MAR

83 APR edition may be used until exhausted.

All other editions are obsolete.

SECURITY CLASSIFICATION OF THIS PAGE

UNCLASSIFIED

10 to the minus 17.0 cm²

17.0 cm²

UNCLASSIFIED

SECURITY CLASSIFICATION OF THIS PAGE

1/24/81

values unfolded from swarm experiments (Hunter and Christophorou, 1984; Spyrou and Christophorou, 1985). We also made measurements of the total ionization cross section from threshold to 80 eV, and find it to be similar in general shape to Kurepa's, but with typically half the magnitude. An overall ionization cross section with a threshold at 13.3 eV is recommended, based on threshold data from photoelectron spectroscopy and the present data between 14 and 80 eV. In order to establish the potential for photoenhancement of its dominant dissociative attachment process, involving F^- production, the temperature dependence of this cross section was studied in a different apparatus using a mass filter and ion pulse counting. At 730 K the peak cross section has increased by ~60% and the threshold is lower by 1.1 eV.

This second type of measurement was used to study the predominant dissociative attachment process in C_2H_3Cl , involving Cl^- production. At 290 K this has a threshold at 0.85 eV and a peak at 1.35 eV of $3.2 \times 10^{-17} \text{ cm}^2$, in agreement with the recent work of Stricklett et al. (1986). At 850 K the cross section at the peak is x2.6 larger, and lower in energy by 0.3 eV, while at 0 eV it has reached $6 \times 10^{-18} \text{ cm}^2$. At higher temperatures effects ascribed to thermal dissociation of the C_2H_3Cl were observed.

The remaining two attaching gases, $F_3C.CF_2Cl$ and $(CF_3)_2CO$, were chosen for further study because of their relatively strong absorption at wavelengths well matched to the CO_2 laser, although concern existed that they would exhibit excessive attachment at low electron energies. The present attachment cross section measurements established that this is indeed the case, and it was determined that they did not warrant further investigation in the present context.

Photoenhancement studies were made of both Cl^- production from C_2H_3Cl , and F^- production from C_3F_8 . In this study measurements were also made of the photoenhancement of SF_5^- production from SF_6 to provide a reference against which to judge the observations. In the gases of present interest we were unable to observe any systematic changes in the attachment cross sections when the gases were irradiated under essentially the same conditions as used with SF_6 .

Methane was chosen as the most suitable main gas for use in a diffuse discharge switch, and a series of swarm measurements to provide definitive data over a wide range of E/N were performed. The derived values of the net ionization coefficient ($\alpha-n$) are in reasonably good agreement with earlier work of Cookson et al. (1966) and Heylen (1975), but severe discrepancies exist with the recent results of Hunter et al. (1986). The present and earlier measurements of ($\alpha-n$) at low E/N are incompatible with the available total attachment cross section measurements of Sharp and Dowell (1967), leading us to postulate that H^- suffers rapid detachment under the conditions of the swarm experiments.



Accession For	
NTIS	GRA&I <input checked="" type="checkbox"/>
DTIC TAB	<input type="checkbox"/>
Unannounced	<input type="checkbox"/>
Justification _____	
By _____	
Distribution/ _____	
Availability Codes	
Dist	Avail and/or Special
A-1	

UNCLASSIFIED

SECURITY CLASSIFICATION OF THIS PAGE

TABLE OF CONTENTS

	<u>PAGE</u>
LIST OF FIGURES AND TABLES	v
1. INTRODUCTION AND SUMMARY	1
1.1 Statement of the Problem and Approach	1
1.2 Summary of Results and Conclusions	4
2. SELECTION OF GASES TO BE STUDIED	7
2.1 Attaching Gas Additives	7
2.2 Main Carrier Gas	11
3. TEMPERATURE DEPENDENCE OF ATTACHMENT CROSS SECTIONS	13
3.1 Experimental Procedures	13
3.2 Perfluoropropane, C_3F_8	14
3.3 Vinyl Chloride, C_2H_3Cl	15
3.4 Hexafluoroacetone, $(CF_3)_2CO$	15
3.5 Chloropentafluorethane, C_3F_5Cl	24
3.6 Conclusions from the Temperature Dependence Measurements	24
4. PHOTO-ENHANCED ATTACHMENT MEASUREMENTS	28
4.1 Experimental Procedures	28
4.2 Reference Measurements in SF_6	35
4.3 Measurements in C_3H_3Cl	38
4.4 Measurements in C_3F_8	38

5. DRIFT TUBE MEASUREMENTS IN METHANE	44
6. PUBLICATIONS AND PRESENTATIONS	48
7. LIST OF PARTICIPATING PERSONNEL	49
8. ACKNOWLEDGMENTS	50
9. REFERENCES	51
10. APPENDICES	
10.1 Preprint: "Ionization and Temperature Dependent Attachment Cross Sections of C_3F_8 and C_2H_3Cl ." P. J. Chantry and C. L. Chen. To be submitted to J. Chem. Phys.	
10.2 Preprint: "Measurements of Swarm Parameters and Derived Electron Collision Cross Sections in Methane." D. K. Davies, L. E. Kline, and W. E. Bies. To be submitted to J. Appl. Phys.	

LIST OF FIGURES

Fig. 3.1 Comparison of the shapes of the appearance curves for SF_6^- from SF_6 and $(\text{CF}_3)_2\text{CO}^-$ from $(\text{CF}_3)_2\text{CO}$ at zero energy, measured using the RPD technique. The two sets of data have been normalized to the same peak height.

Fig. 3.2 Dissociative attachment cross sections for producing the ions indicated from $(\text{CF}_3)_2\text{CO}$ at room temperature. The F^- peak at 6.6 eV was calibrated against O^- production from N_2O and used to calibrate the remaining curves. See also Fig. 3.3.

Fig. 3.3 Dissociative attachment cross sections for producing the ions indicated from $(\text{CF}_3)_2\text{CO}$ at room temperature, calibrated against the F^- peak at 6.6 eV shown in Fig. 3.2.

Fig. 3.4 The cross section for parent negative ion production in $(\text{CF}_3)_2\text{CO}$. The open points were measured in the same way as the data of Figs. 3.2 and 3.3, at room temperature. The filled points were obtained at 730 K and were normalized together with the fragment ion data to give a peak total cross section of $9 \times 10^{-18} \text{ cm}^2$.

Fig. 3.5 The total attachment cross section of $(\text{CF}_3)_2\text{CO}$ at room temperature (o) and at 730 K (•). The room temperature curve is obtained by summing the individual curves shown in Figs. 3.2, 3.3, and 3.4. The 730 K curve was obtained by summing the individual signals and normalizing to the room temperature peak at 6.2 eV.

Fig. 3.6 Showing the dissociative attachment cross sections measured in $\text{C}_2\text{F}_5\text{Cl}$ at room temperature.

Fig. 3.7 The total attachment cross section for C_2F_5Cl at room temperature obtained by summing the individual cross sections shown in Fig. 3.6. The data above 4.5 eV have been smoothed.

Fig. 4.1 Showing the general principle of the trochoidal electron gun chosen to avoid interaction of the laser beam with the electron gun filament, and the interaction geometry of the collinear electron-laser beams with the neutral molecular beam.

Fig. 4.2 Detailed horizontal section of the electrode structure of the electron gun and beam deflector electrodes, keyed to Table 4.1.

Fig. 4.3 General layout of the experimental system shown from the side, approximately to scale.

Fig. 4.4 Side view of the molecular beam source assembly. The insulated high-current feedthrough shown in the figure obscures an identical second one mounted beside it.

Fig. 4.5 Electron retarding curve and its derivative measured in the presence of SF_6 and laser radiation at $10.63 \mu m$. The energy scale has been adjusted to represent the most probable electron energy.

Fig. 4.6 SF_5^- production from SF_6 measured with (•) and without (○) the laser beam ($10.63 \mu m$) at room temperature. The difference signal is shown by the filled squares.

Fig. 4.7 Cl^- production from $\text{C}_2\text{H}_3\text{Cl}$ measured with (•) and without (○) the laser beam (10.63 μm) at room temperature. The difference signal is shown by the filled squares.

Fig. 4.8 Cl^- production from $\text{C}_2\text{H}_3\text{Cl}$ measured with (•) and without (○) the laser beam (10.63 μm) at 700 K. The difference signal is shown by the filled squares.

Fig. 4.9 F^- production from C_3F_8 measured with (•) and without (○) the laser beam (9.66 μm) at room temperature. The difference signal is shown by the filled squares.

Fig. 4.10 F^- production from C_3F_8 measured with (•) and without (○) the laser beam (9.68 μm) at 700 K. The difference signal is shown by the filled squares.

LIST OF TABLES

Table 4.1 Parts list for the electrode structure shown in Fig. 4.2.

1. INTRODUCTION AND SUMMARY

1.1 STATEMENT OF THE PROBLEM AND APPROACH

Externally sustained diffuse discharge switches are potentially applicable in pulse power engineering as high-current interruption devices. The basic switch concept involves the use of a diffuse uniform plasma sustained by an external source of ionization. The latter is most likely to be a high-energy (~ 100 kV) large cross-section electron beam, injected into a gas at approximately one atmosphere pressure between plane parallel electrodes. The conductivity of the plasma is controlled by the e-beam intensity and depends on the balance of the volume electron production and loss processes in the gas. The electron kinetic processes involved in this balance depend significantly on the gases involved, and therefore the optimization of the gas or gas mixture is of major concern in the development of such a switch (Schoenbach et al., 1982). In order to maximize the conductivity of the switch during the "on" phase, it is clearly desirable to choose a gas or gas mixture having a high electron drift velocity, and low electron loss rates from electron-ion recombination and attachment.

It has long been known that certain gases or gas mixtures have anomalously high electron drift velocities over a restricted range of E/N , the density-reduced electric field, with the drift velocity being only weakly dependent on the field in this region, and in some cases decreasing with increasing field. This very desirable behavior is due to the presence of a Ramsauer minimum in the momentum transfer electron-scattering cross section, combined with a strong energy loss process starting at slightly higher energies. It follows that the desired

operating E/N of the switch should be such that the mean electron energy is at or close to the minimum in the scattering cross section, which is typically at a few tenths of an eV. Hence, in designing a suitable gas mixture one objective is to minimize the electron attachment rate at energies in the region of a few tenths of an eV.

When the switch is turned off, the volume ionization processes due to the e-beam are no longer present. For maximum switch efficiency it is desirable that the decay in conductivity be as rapid as possible. This decay is controlled by the volume recombination and attachment processes, with the effects of the latter being dominant below a certain level of ionization due to the quadratic nature of the former. A number of studies have shown that the presence of attachment during the switch recovery phase is essential if the switch is to have the desired fast turn-off (Kline, 1982). Hence, one is faced with the dilemma of designing a gas mixture which has little or no attachment during the "on" phase of the switch, but rapidly changes its behavior to being strongly attaching when the switch is turned "off".

A partial solution to the problem is available by choosing as one of the constituents a gas that has an attachment threshold which is above the operating mean energy of a few tenths of an eV, but within the range of the higher electron energies reached during the recovery phase, as higher circuit voltages develop across the increasing impedance of the switch. Hence, one is looking for a gas which has an attachment threshold above, say, 0.5 eV and with a rapidly increasing cross section above the threshold. A number of candidates has been identified having such attaching properties (Christophorou, 1982), and tests of related gas mixtures have been performed (Bletzinger, 1983).

The present work addresses the problem of designing a gas mixture which includes a gas meeting the above criteria regarding the "passive" attaching properties, but which also offers the possibility of further improving the switch performance by optically enhancing the attachment process during the switch recovery phase. Possible means of

achieving this are (i) by photodissociation causing formation of strongly attaching neutral fragments (Rossi et al., 1985; Kobayashi et al., 1987), (ii) by short wavelength optical excitation of higher energy electronic states having larger attachment cross sections (Christophorou et al., 1987), or (iii) by vibrational excitation of the attacher by tuned infrared irradiation (Chen and Chantry, 1979; Eisele, 1984; Schaefer et al., 1988). The work performed under this contract focussed exclusively on the third approach.

The overall approach taken was to first perform a literature survey of potentially suitable gases to establish a short list of candidates. The choice was based primarily on two criteria: (i) the absorption spectrum of the gas should provide adequate overlap with the available tuning range of high-power CO₂ lasers, and (ii) the attachment cross section of the unexcited gas should meet the requirements outlined in the discussion above. The next step in screening these candidates was to establish the sensitivity of their attachment cross sections to non-selective vibrational excitation, achieved by simply heating the gas. Finally, measurements were to be made on the most promising gas(es) to quantify the attachment cross sections and their sensitivity to CO₂ laser irradiation.

It was anticipated from the outset that the attaching gas(es) chosen by the above selection process would be used as a relatively low concentration additive to the main gas. In parallel with the above we also had the objective of choosing the main gas and defining its properties sufficiently well that the electron transport properties of the final mixture could be confidently predicted via a Boltzmann code analysis. To meet this objective we performed measurements of the relevant electron transport coefficients in the selected main gas to provide the data of sufficient accuracy for subsequent Boltzmann code analysis. Thus, these various components of the program were conceived to provide the necessary basic information required for properly optimizing the gas mixture and predicting its electron transport

properties both in the "cold" state, and under conditions of laser excitation of the attaching additive.

1.2 SUMMARY OF RESULTS AND CONCLUSIONS

Based on a literature survey of available gases whose infrared absorption spectra overlap the output spectrum of efficient CO_2 lasers, we selected four gases for further experimental study in order to determine the viability of using them as optically controlled attaching additives in diffuse gas discharge switch applications. Two of the gases chosen, perfluoropropane (C_3F_8) and vinyl chloride ($\text{C}_2\text{H}_3\text{Cl}$), were known to have desirable attachment cross-section shapes, but their cross-section magnitudes were uncertain and their temperature sensitivity unknown. In the present work we have determined that the room temperature total attachment cross section of C_3F_8 peaks at 2.8 eV with a value of $1.75 \times 10^{-17} \text{ cm}^2$. This is 14 times smaller than the only other measurement of this type we are aware of (Kurepa, 1965). There is much better agreement with two more recently reported values unfolded from swarm experiments (Hunter and Christophorou, 1984; Spyrou and Christophorou, 1985).

In view of the very large discrepancy with Kurepa's work regarding the attachment cross section, we also made measurements of the total ionization cross section from threshold to 80 eV. We find it to be similar in general shape to Kurepa's, but with typically half the magnitude. The ionization threshold cannot be accurately derived from these measurements, due to severe upward curvature immediately above threshold. The positive ion signal rises above the background at 13.0 ± 0.1 eV, to be regarded as a lower limit to the true threshold. An overall ionization cross section with a threshold at 13.3 eV is recommended, based on threshold data from photo-electron spectroscopy and the present data between 14 and 80 eV. In order to establish the potential for photo-enhancement of its dominant dissociative attachment

process, involving F^- production, the temperature dependence of this cross section was studied in a different apparatus using a mass filter and ion pulse counting. At 730 K the peak cross section has increased by ~60% and the threshold is lower by 1.1 eV.

This second type of measurement was used to study the predominant dissociative attachment process in C_2H_3Cl , involving Cl^- production. At 290 K this has a threshold at 0.85 eV and a peak at 1.35 eV of $3.2 \times 10^{-17} \text{ cm}^2$, in good agreement with the recent work of Stricklett et al. (1986). At 850 K the cross section at the peak is 2.6 times larger and lower in energy by 0.3 eV, while at 0 eV it has reached $6 \times 10^{-18} \text{ cm}^2$. At higher temperatures effects ascribed to thermal dissociation of the C_2H_3Cl were observed.

The remaining two attaching gases were chosen for further study because of their relatively strong absorption at wavelengths well matched to the CO_2 laser, although concern existed that they would exhibit excessive attachment at low electron energies. The present work established that this is indeed the case, and it was determined that they did not warrant further investigation in the present context.

The temperature dependence measurements suggested that both C_3F_8 and C_2H_3Cl might be susceptible to photo-enhancement of their attachment cross sections. Of the two, C_2H_3Cl was the more attractive in that its cross section is better situated in energy for the switch application, and the observed temperature sensitivity is greater. On the other hand, the effects of thermal decomposition observed in the present work indicate the possibility of similar chemical instability problems in the gas discharge environment.

Photo-enhancement studies were made of both Cl^- production from C_2H_3Cl and F^- production from C_3F_8 . In this study measurements were also made of the photo-enhancement of SF_5^- production from SF_6 to provide a reference against which to judge the observations. The effects observed in SF_6 are consistent with our earlier study of this effect (Chen and Chantry, 1979) but are less well resolved due to the

lower energy resolution achieved in the present study. In the gases of present interest we were unable to observe any systematic changes in the attachment cross sections when the gases were irradiated under essentially the same conditions as used with SF₆. The absence of an observable effect may be due to the much smaller optical absorption cross sections of approximately 10⁻¹⁹ cm² for these gases, compared to approximately 10⁻¹⁷ cm² for SF₆.

Methane was chosen as the most suitable main gas for use in a diffuse discharge, based on existing analysis (Kline, 1982) and experiment (Bletzinger, 1983). In view of the known difficulties of reconciling the existing information on measured cross sections and measured electron transport coefficients, we performed a series of swarm measurements to provide definitive data over a wide range of E/N. The derived values of the net ionization coefficient ($\alpha-\eta$) are in reasonably good agreement with earlier work of Cookson et al. (1966) and Heylen (1975), but severe discrepancies exist with the recent results of Hunter et al. (1986). The present and earlier measurements of ($\alpha-\eta$) at low E/N are incompatible with the available total attachment cross-section measurements of Sharp and Dowell (1967), leading us to postulate that H⁻ suffers rapid detachment under the conditions of the swarm experiments.

2. SELECTION OF GASES TO BE STUDIED

2.1 ATTACHING ADDITIVE CANDIDATES

Engineering feasibility of optically enhancing the electron attachment process by infrared excitation of the molecular vibrational modes requires that an efficient infrared source be available to supply the required fluence at the required wavelength. The requirement of wavelength tunability, and other issues regarding depositing the power uniformly in the active gas volume situated remotely from the optical source, can probably only be met by a laser. The decision was made to restrict the selection of gases to those whose absorption spectra have reasonable overlap with the output of efficient CO₂ lasers. These operate on either the 001-100 or the 001-020 vibrational transitions, each of which gives two branch series of rotationally spaced lines.

The power obtainable from such a laser is typically a maximum for the transitions in the vicinity of P20, at 10.6 μm , but use of a tuning element such as a reflecting grating at one end of the optical cavity allows the output to be tuned over the four branches, from below 9.2 μm to above 10.8 μm with gaps in the region of 9.4, 9.9, and 10.4 μm . Detailed tabulations of the usable laser wavelengths are readily available (Handbook of Lasers), but similarly fine detail is typically not available in the published absorption spectra. For the present purposes, information on the IR absorption properties of the gases of interest was usually available from the Matheson Gas Products Gas Data File, and was usually adequate in the form provided. This reference was also a useful source of important other information such as chemical

stability and toxicity, which were also of concern in the present screening process.

The only other criterion applied in selecting the gas concerns its electron attaching behavior. The desirable type of behavior is discussed in some detail in Section 1. Only in the case of SF_6 was information available on all aspects of the attachment behavior (Kline et al., 1979; Chen and Chantry, 1979), and this gas is necessarily disqualified for the present application because of its extremely strong attachment of low-energy electrons in both the "cold" and "hot" states. In a few instances information was available regarding the temperature dependence of the attachment, but many of these were disqualified for other reasons. These included N_2O , which in many respects is a very attractive candidate for this application. When cold it has an attachment threshold in the vicinity of 0.4 eV, and is known to have an attachment cross section which is extremely sensitive to vibrational excitation (Chantry, 1969a). Unfortunately, its absorption spectrum is inaccessible with the CO_2 laser, and for this reason it was not considered further in the present context.

In other cases the "room temperature" attachment information was reasonably complete, meaning that either the electron energy dependence of the attachment cross section had been measured, or the E/N dependence of the attachment coefficient. In those many instances where such data were not available, some inferences regarding the attaching behavior could be drawn from measurements of the relative dielectric strength of the gas. This particular information was useful primarily as a disqualifier, in that very good dielectrics almost invariably are strongly attaching over a wide range of electron energy, and have attachment coefficients which decrease with E/N, in contrast to the behavior required in the present context.

Based on their absorption spectra, consideration was given to the following gases:

Chlorotrifluorethylene (F₂C:CFCl) has an absorption peak at 9.5 μm , where the absorption cross section is approximately $5 \times 10^{-19} \text{ cm}^2$. This is well situated relative to the laser wavelengths. The gas was disqualified because of its reactivity and toxicity.

1.1-Difluorethylene (H₂C:CF₂) has an absorption peak at 9.4 μm , where the absorption cross section is approximately $2.5 \times 10^{-19} \text{ cm}^2$. The attachment threshold is at 1.6 eV, but the process is very weak. Main attachment process peaks at 7.3 eV (Thynne and MacNeil, 1971).

1.1-Difluoro-1-chloroethane (H₃C:CF₂Cl) has an absorption peak of $3.3 \times 10^{-19} \text{ cm}^2$ at 10.3 μm . No information found on attachment.

Vinyl Fluoride (H₂C:CHF) has an absorption peak of $1.4 \times 10^{-19} \text{ cm}^2$ at 10.6 μm . Dissociative attachment is very weak and peaks at 2.2 eV with a threshold at 1.6 eV (Olthoff et al., 1985).

Nitrogen Trifluoride (NF₃) has an absorption peak of approximately $1 \times 10^{-19} \text{ cm}^2$ at 9.7 μm . Dissociative attachment is strong, peaking at 1.6 eV with a cross section of $1.2 \times 10^{-16} \text{ cm}^2$ (Chantry, 1982). Measured attachment rate coefficient is weakly dependent on temperature (Trainor and Jacob, 1979). Photo-enhancement of attachment attempted in a discharge, but no effect was observed (Eisele, 1984).

Chloropentafluorethane (FC 115), (F₃C:CF₂Cl) has a strong absorption peak of approximately $5 \times 10^{-17} \text{ cm}^2$ at 10.2 μm . We found no detailed information on electron attachment, but this gas is known to have good electrical strength (Wootton et al., 1980).

Hexafluoroacetone (F₃C:CO:CF₃) has a reasonably strong absorption peak of approximately $5 \times 10^{-18} \text{ cm}^2$ at 10.3 μm . Electron attachment occurs predominantly by production of CF_3^- and F^- with thresholds in the region

of 3 eV (Harland and Thynne, 1970). Many other fragment ions are also formed, with thresholds in the same region or higher. The parent ion was also observed at zero energy, but anomalies were found in its intensity dependence in the presence of SF₆. The cross section for its formation was measured to be 60 times smaller than that for SF₆⁻ production from SF₆.

Perfluoropropane (C₃F₈) has an absorption peak of approximately $3 \times 10^{-18} \text{ cm}^2$ at 9.9 μm , which unfortunately is in one of the gaps in the CO₂ laser spectrum. A secondary peak of approximately $7 \times 10^{-20} \text{ cm}^2$ is well situated at 9.7 μm . Available attachment data included a cross-section measurement (Kurepa, 1965), which indicates this is an interesting candidate from this aspect (Christophorou et al., 1982). Recovery tests of discharges containing this additive have been made (Bletzinger, 1983).

Vinyl Chloride (H₂C:CHCl) has an absorption peak of approximately $1.6 \times 10^{-19} \text{ cm}^2$ at 10.7 μm . The first dissociative attachment measurements (Kauffel et al., 1984) showed Cl⁻ peaking at 1.2 eV, but later works give 1.35 eV with the threshold being at 0.8 eV. Recent attachment coefficient measurements (Rossi et al., 1985) show a steep dependence on E/N. Very recent unpublished data (Schaefer et al., 1988), on photo-induced impedance changes in gas discharges, show effects ascribed to photo-enhanced attachment.

Based on this information we chose to do exploratory measurements on the last four gases, starting with C₃F₈. The choice of this gas was primarily based on its desirable "cold" attachment behavior (Christophorou et al., 1982) and its established chemical stability. It was not so appealing on the basis of the IR absorption, but the hope existed that adequate absorption could be achieved by working at the long wavelength limit of the P branch of the 001-020 transition, in the region of 9.8 μm , or at the subsidiary absorption peak at 9.7 μm .

The decision to investigate $\text{F}_3\text{C}.\text{CF}_2\text{Cl}$ was based on its very strong absorption at a wavelength-matching well to the laser, despite misgivings regarding the high dielectric strength. The intention was to first document the energy dependence of the attachment cross section to establish how much of this strength involved low-energy processes, which in the present context are very undesirable.

Similar reasoning applied to the choice of $(\text{CF}_3)_2\text{CO}$, except that more information was already available regarding the energy dependence of the attachment. Inconsistencies present in the previous work needed to be resolved, and we therefore decided to make at least a preliminary investigation of this gas.

The decision to investigate $\text{C}_2\text{H}_3\text{Cl}$ came from a number of factors, including its attachment peak position which is better situated than that of C_3F_8 . Its IR absorption is well matched to the laser, but relatively weak. However, in private discussions, Burrow pointed out that vibrational excitation of this molecule causing out-of-plane distortion of the Cl would be expected to increase the dissociative attachment cross section. Also, Schaefer et al. were obtaining evidence of photo-enhanced attachment in gas discharge impedance measurements in work which has subsequently been submitted for publication (Schaefer et al., 1988). With these inputs we decided to promote this molecule to the top of the short list of molecules to be investigated.

2.2 MAIN CARRIER GAS

The selection of the main gas was relatively straightforward, in that considerable work had been previously performed regarding the desired properties (Kline, 1982), and experiments had already demonstrated the adequacy CH_4 in this application (Bletzinger, 1983). However, there were known to be difficulties in reconciling published measurements of attachment cross sections (Sharp and Dowell, 1967) with measured net ionization coefficients. The establishment of a reliable

cross section set for this molecule required that this issue be resolved, and the decision was made to perform swarm measurements of the various electron transport coefficients in order to provide definitive data for subsequent analysis. These measurements involved entirely different equipment to the work on attaching additives and proceeded in parallel.

3. TEMPERATURE DEPENDENCE OF ATTACHMENT CROSS SECTIONS

3.1 EXPERIMENTAL PROCEDURES

A complete description of the experimental approach appears in Section 10.1, which is an Appendix consisting of a preprint of a paper describing these measurements in C_3F_8 and in C_2H_3Cl . Only a brief summary is given here.

Measurements were performed with two types of apparatus. The first apparatus permits measurements of the total ion current as a function of the absolute pressure in the collision chamber. Comparison of these signals with others obtained similarly using a gas for which the cross section is known, provides a measure of the absolute cross section. The second type of measurement employs a "high-temperature tube" having a heatable collision chamber which allows us to measure the dependence of the ion production processes on the gas temperature. In both cases the electron beam is produced by a directly heated filament and an electron gun employing the retarding potential difference (RPD) technique (Chantry, 1969b) to enhance the energy resolution. With either apparatus, mass-analyzed ion detection can be performed using a quadrupole mass filter employing ion-counting techniques. In the measurements reported here this feature was used exclusively with the high-temperature tube.

3.2 PEFLUOROPROPANE, C_3F_8

The cross-section measurements, and the study of their temperature sensitivity, are described in detail in Section 10.1. Only a brief summary is given here. When starting the present study we anticipated confirming the validity of the earlier measurement of the attachment cross section (Kurepa, 1965) and moving quickly to the study of the temperature sensitivity of the process. However, our initial cross-section measurements revealed a surprisingly large discrepancy, exceeding an order of magnitude, in the peak magnitude. Because of this we determined that a more extensive series of room temperature measurements was needed to provide more definitive cross-section data for both total attachment and total ionization.

Our total ionization cross section is similar in general shape to Kurepa's, but with typically half the magnitude. The ionization threshold cannot be accurately derived from our measurements, due to severe upward curvature of the cross section immediately above threshold. The positive ion signal rises above the background at 13.0 ± 0.1 eV, to be regarded as a lower limit to the true threshold. An overall ionization cross section with a threshold at 13.3 eV is recommended, based on threshold data from photo-electron spectroscopy (Dewar and Worley, 1969) and the present data between 14 and 80 eV. The present measurement of the room temperature total attachment cross section peaks at 2.8 eV with a value of $1.75 \times 10^{-17} \text{ cm}^2$. This is 14 times smaller than Kurepa's peak value.

There is much better agreement with two more recently reported peak attachment cross-section values unfolded from swarm experiments (Hunter and Christophorou, 1984; Spyrou and Christophorou, 1985), although discrepancies exist regarding the detailed shape. These discrepancies may be due in part to the difficulties in separating the contributions of non-dissociative and dissociative attachment to the swarm results.

The temperature dependence of the predominant dissociative attachment process, involving F^- production, was measured at a series of temperatures up to 730 K. At the highest temperature the peak cross section has increased by ~60% and the threshold is lower by 1.1 eV. This result is in reasonable agreement with that of Spyrou and Christophorou (1985), taken at 750 K, regarding the peak magnitude. Significant discrepancies are present regarding the shape, but these too may be related to the difficulty mentioned above regarding the separation of the two processes involved in the swarm measurement. There was no evidence of thermal dissociation detected in these measurements.

3.3 VINYL CHLORIDE, C_2H_3Cl

Previous work (Kaufel et al., 1984) had established that Cl^- is the dominant ion formed by dissociative attachment to C_2H_3Cl . The measurements made to determine the cross section for this process at room temperature and higher are described in detail in Section 10.1. The results are summarized here. At 290 K F^- production has a threshold at 0.85 eV and a peak at 1.35 eV, having a FWHM of 0.6 eV and an amplitude of $3.2 \times 10^{-17} \text{ cm}^2$. These results are in good agreement with recent work elsewhere (Olthoff et al., 1985; Dressler et al., 1985; Stricklett et al., 1986). At 850 K the cross section at the peak is 2.6 times larger and lower in energy by 0.3 eV, while at 0 eV it has reached $6 \times 10^{-18} \text{ cm}^2$. At temperatures above 850 K the signal measured for production of the parent positive ion decreased significantly faster than normal. This effect was ascribed to thermal dissociation of the C_2H_3Cl at these higher temperatures.

3.4 HEXAFLUOROACETONE, $(CF_3)_2CO$

The available attachment data on this gas (Harland and Thynne, 1970) were not encouraging, in that there was definite evidence for parent ion production at very low energies. There were, however, reasons to question the validity of the cross section, which had been

measured relative to that of SF_6 , in that unexplained anomalies were observed in the mixture experiments. The main objective of the present measurements was to confirm the presence of the low-energy process and its magnitude relative to the higher energy processes. This would establish whether or not this gas deserved further consideration in the present context.

Most of the data were taken at nominally room temperature, which in this case means the gas is close to 300 K. Throughout the measurements on this gas we experienced difficulties with the operation of the electron gun. The electron emission from the filament was quite severely depressed by this gas, which precluded the use of transmitted "retarded" currents larger than 10^{-7} A. The behavior of the gun suggested that the filament was not emitting efficiently over the relevant area, i.e., there is a "hot spot" of emission not aligned well with the gun axis. Consequently, the performance of the electron gun was adequate but below par for this particular series of measurements.

The shape of the low-energy parent ion peak was measured using the RPD technique, and the results are compared in Fig. 3.1 with the shape of the equivalent peak measured similarly in SF_6 . The two measurements have been normalized to the same peak height to facilitate this comparison of the shapes. In contrast to the work of Harland and Thynne, we find that the peaks are significantly different, with that for $(CF_3)_2CO^-$ production being measurably broader in energy than that for SF_6^- . The electron energy scale for this plot was obtained by adding 0.05 to the measured accelerating voltage scale so that the peak ion signals appear at a small (<0.05 eV) positive energy. The resulting scale, representing the "most probable energy" of the distribution, is essentially identical to that obtained from the steepest part of the "difference" current-retarding curves taken with this data.

The magnitude of the zero-energy parent ion peak was estimated approximately from the known magnitude of the SF_6^- peak by comparing

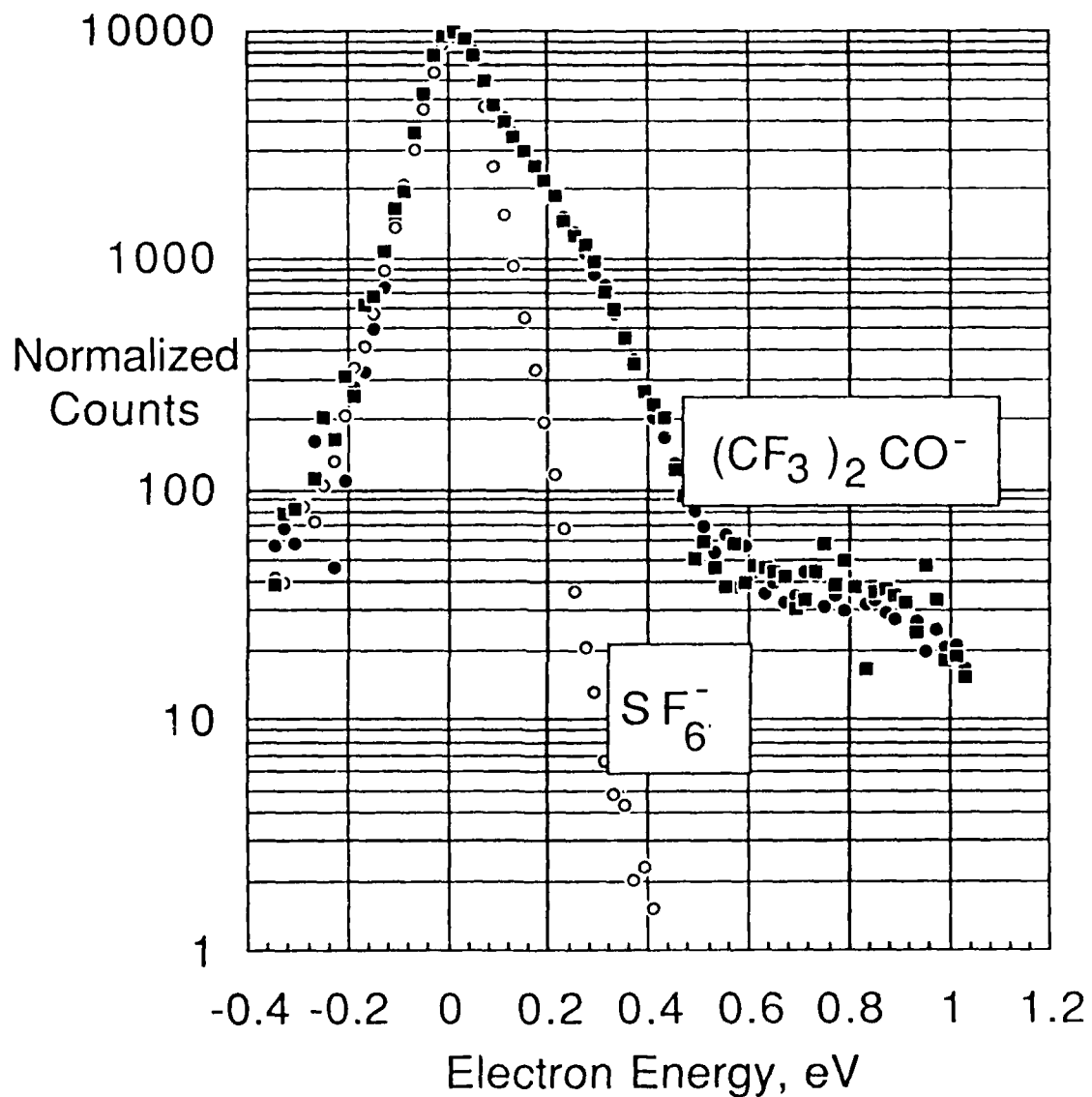


Figure 3.1 — Comparison of the shapes of the appearance curves for SF_6 from SF_6 and $(\text{CF}_3)_2\text{CO}^-$ from $(\text{CF}_3)_2\text{CO}$ at zero energy, measured using RPD technique. The two sets of data have been normalized to the same peak height.

these signals measured separately as a function of pressure. In recording this data, care was taken to use the same retarded electron current (5×10^{-10} A) obtained from the same unretarded current (15×10^{-10} A). This procedure was adopted to ensure that the electron energy distributions used for the two sets of measurements were as nearly the same as possible. The ratio of the measured peak signals would then give a true measure of the ratio of the cross sections, if they have the same shape. In the present case the latter is only approximately so, the $(CF_3)_2CO^-$ cross section having a measurable high-energy tail, as shown in Fig. 3.1. It follows that the peak cross section of $(CF_3)_2CO^-$ is likely to be overestimated relative to that of SF_6^- , and the conclusion from these particular data is that the SF_6^- cross section exceeds that for $(CF_3)_2CO^-$ by at least a factor of 30. Using a previously measured (Kline et al., 1979) value of $(5.5 \pm 2.0) \times 10^{-14} \text{ cm}^2$ for SF_6^- , we conclude that the $(CF_3)_2CO^-$ production cross section is less than $(1.8 \pm 0.7) \times 10^{-15} \text{ cm}^2$.

In order to determine the total dissociative attachment cross section, it was necessary to measure the individual cross sections for the various fragment ions formed in this gas. Because of the difficulties of operating the gun mentioned above, and to avoid spending an excessive time acquiring appearance curves for the many ions involved, most curves were measured without using the RPD technique. This has no significant effect on the accuracy of the cross-section measurements for the fragment ions, whose appearance curves in general have structure substantially larger than the effective energy spread of the "retarded" distribution used. This is approximately 0.4 eV FWHM, judging from the electron beam-retarding curves and the SF_6^- appearance curve obtained under these conditions.

The room temperature results are summarized in Figs. 3.2 and 3.3. The cross-section magnitudes have been obtained by measuring the peak F^- signal at 6.6 eV as a function of pressure and comparing it with similar measurements of the O^- signal from N_2O . The peak F^- cross

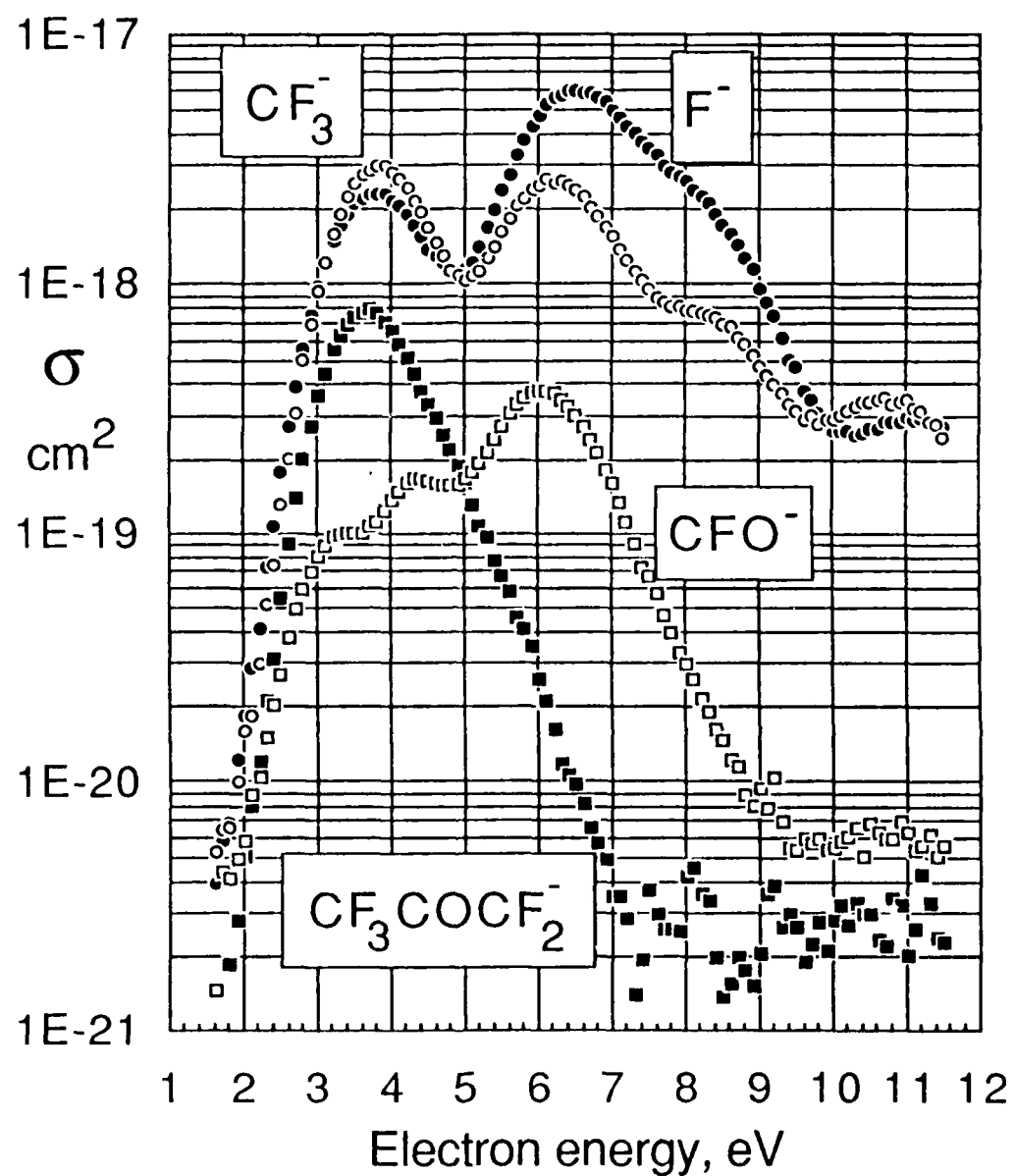


Figure 3.2 — Dissociative attachment cross sections for producing the ions indicated from $(\text{CF}_3)_2\text{CO}$ at room temperature. The F^- peak at 6.6 eV was calibrated against O^- production from N_2O and used to calibrate the remaining curves. See also Fig. 3.3.

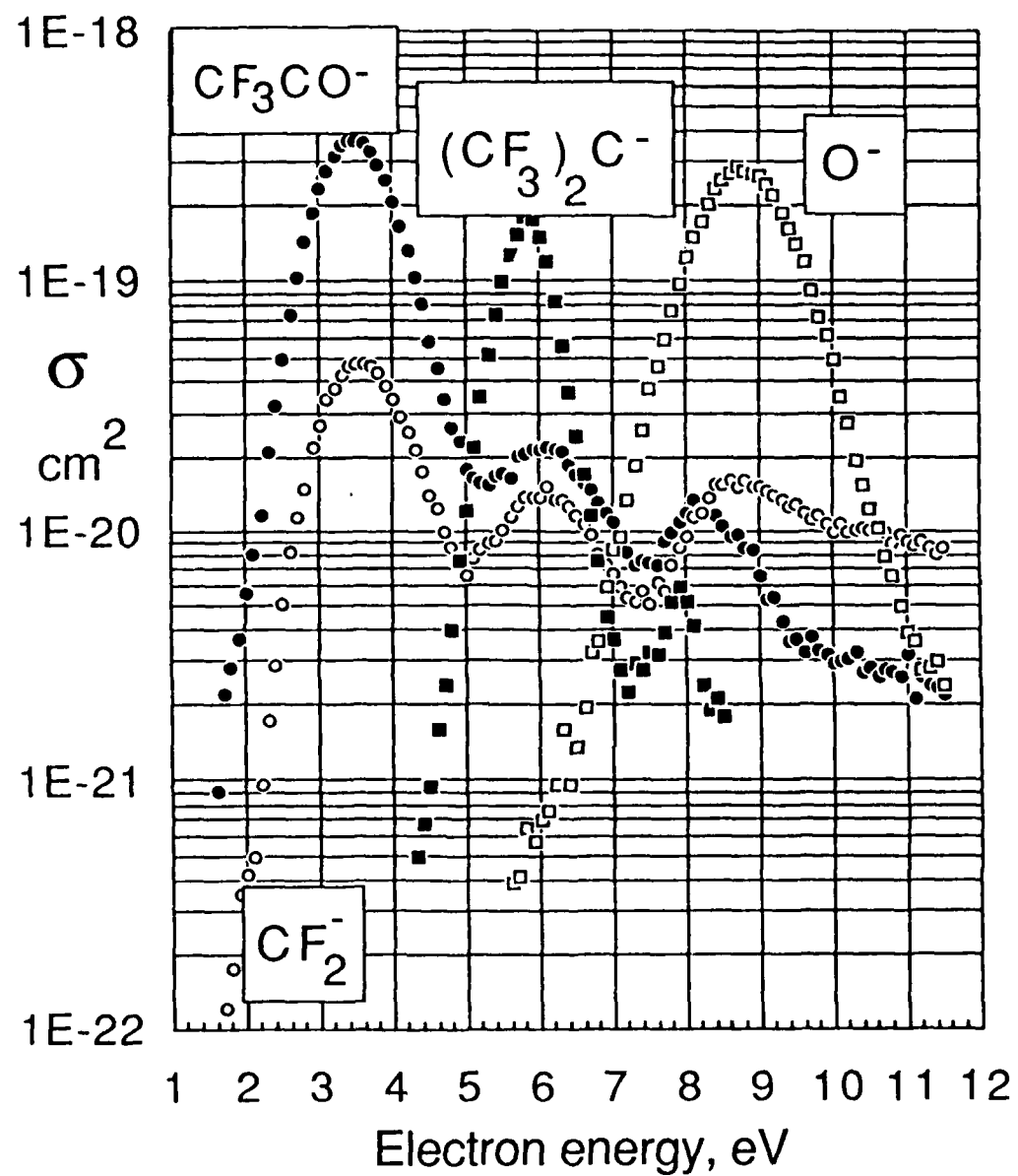


Figure 3.3 — Dissociative attachment cross sections for producing the ions indicated from $(CF_3)_2CO$ at room temperature, calibrated against the F^- peak at 6.6 eV shown in Fig. 3.2.

section determined in this way, $6 \times 10^{-18} \text{ cm}^2$, was then used as a secondary standard to calibrate the other fragment ion signals at their respective peaks. When this same approach was used to measure the cross section for production of the parent ion, we obtained the data shown in Fig. 3.4. The signal detected at energies greater than 2 eV must be interpreted with caution since it may arise from the capture of inelastically scattered electrons (Chantry, 1971).

The peak cross section of $7.5 \times 10^{-16} \text{ cm}^2$ given in Fig. 3.4 is almost certainly an underestimate due to the inadequate energy resolution in this case, the data having been taken without use of the RPD technique. Hence, we can place upper and lower limits of 1.8×10^{-15} and $7.5 \times 10^{-16} \text{ cm}^2$ for the cross section for production of $(\text{CF}_3)_2\text{CO}^-$ at zero energy at room temperature. In Figs. 3.2 and 3.3 the electron energy scale was obtained from a set of measurements performed with a mixture of N_2O and $(\text{CF}_3)_2\text{CO}$, using the known position of the $\text{O}^-/\text{N}_2\text{O}$ peak at 2.25 eV. The resulting scale is consistent within 0.05 eV with that obtained from the retarding curve.

Having measured the individual cross sections, we can obtain the total attachment cross section by summing the individual contributions. The result is shown in Fig. 3.5. Here and in Fig. 3.4 we show the results of measurements made at room temperature and at 730 K. The changes due to the increased temperature were not measured in absolute terms. We have chosen to normalize the measurements at both temperatures to the same peak value of the total cross section of $9 \times 10^{-18} \text{ cm}^2$ at 6.2 eV. We see from Fig. 3.5 that the direction of the effect of increasing temperature on the total cross section depends on the electron energy. This reflects very complicated behavior of the individual cross sections. The dissociative cross sections tend to increase with temperature, with the exception of $(\text{CF}_3)_2\text{C}^-$, while parent ion production decreases dramatically by a factor of at least 20 at zero energy. At the higher temperature a number of the fragment ions

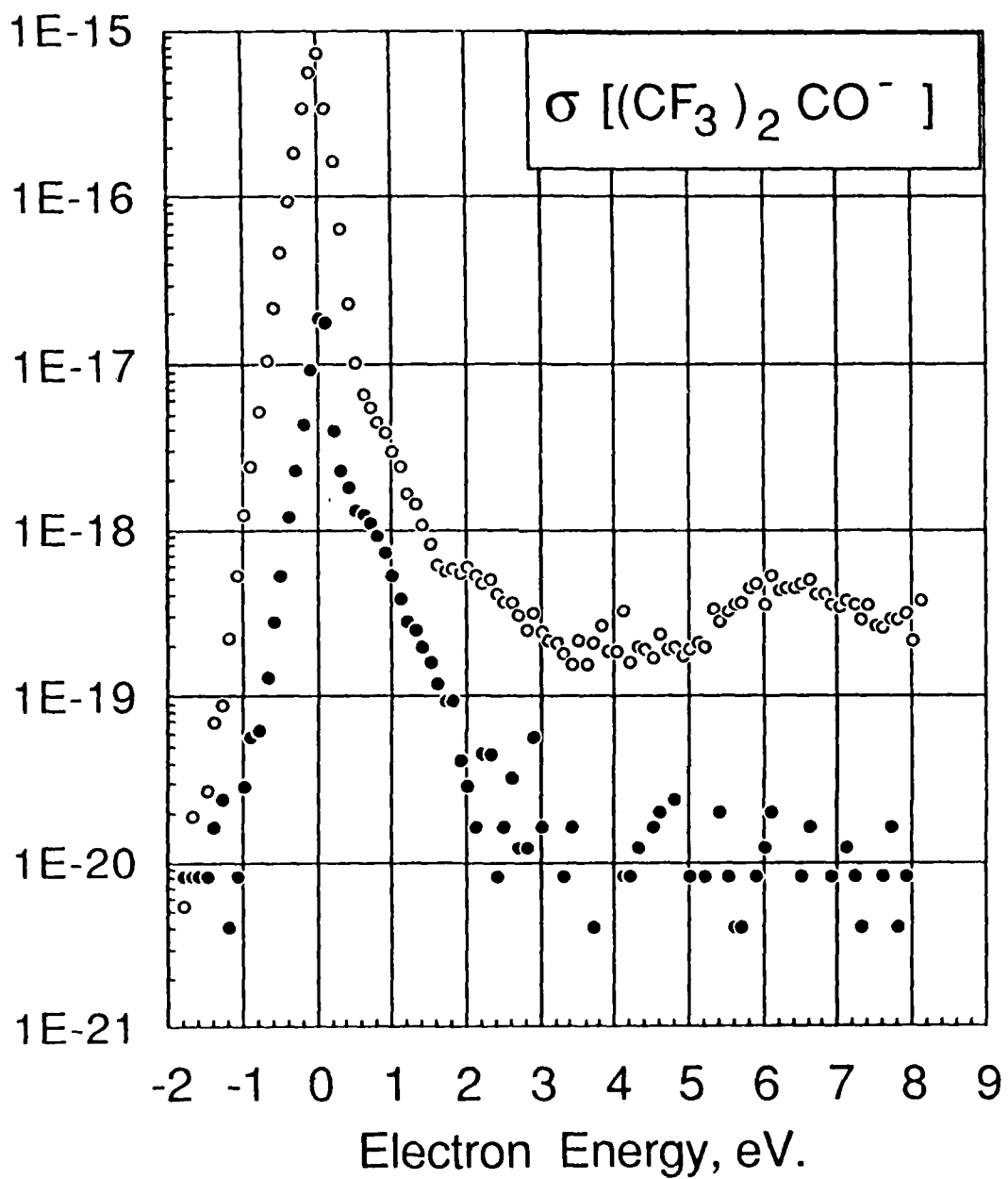


Figure 3.4 — The cross section for parent negative ion production in $(CF_3)_2CO$. The open points were measured in the same way as the data of Figs. 3.2 and 3.3, at room temperature. The filled points were obtained at 730 K and were normalized together with the fragment ion data to give a peak total cross section of $9 \times 10^{-18} \text{ cm}^2$.

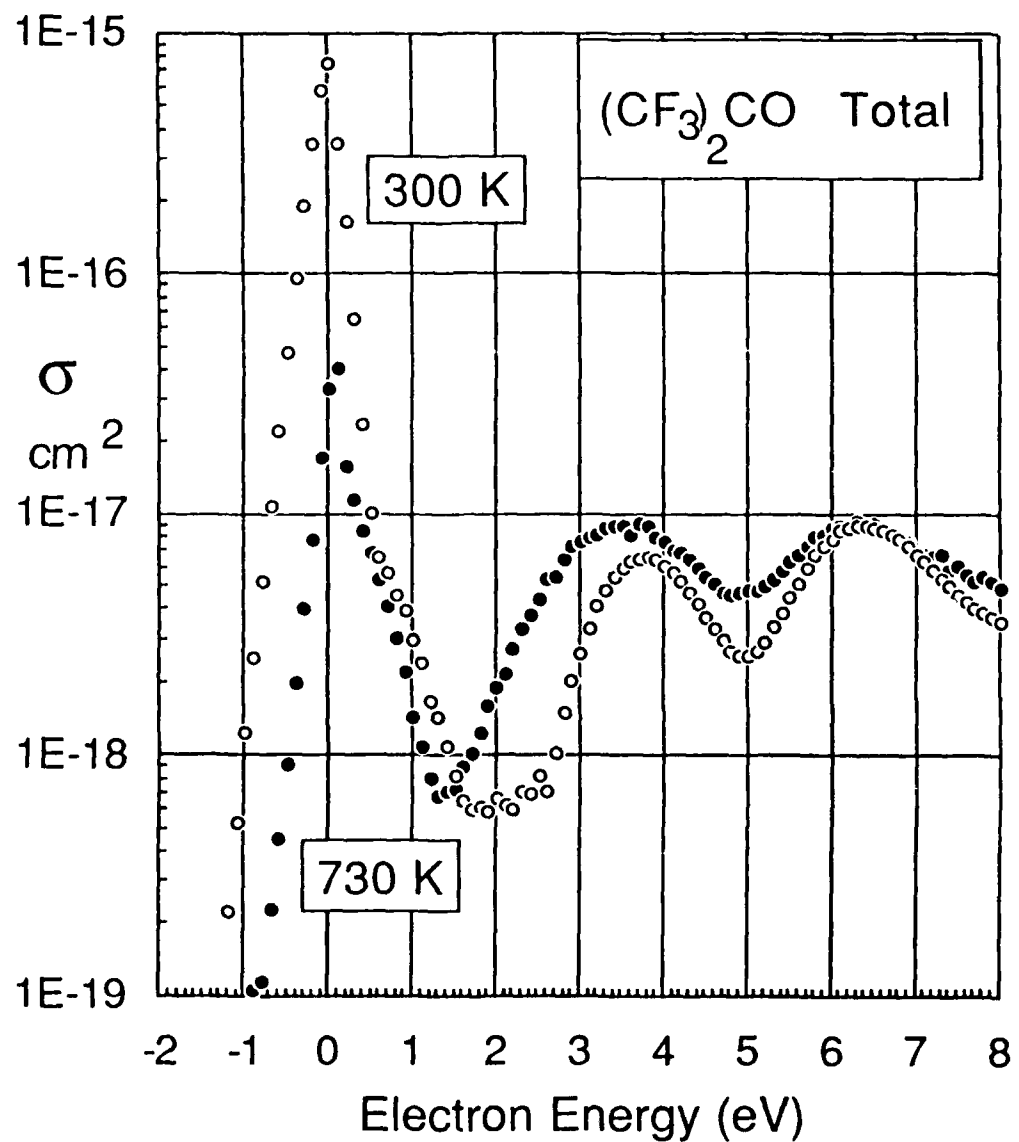


Figure 3.5 — The total attachment cross section of $(CF_3)_2CO$ at room temperature (o) and at 730 K (•). The room temperature curve is obtained by summing the individual curves shown in Figs. 3.2, 3.3, and 3.4. The 730 K curve was obtained by summing the individual signals and normalizing to the room temperature peak at 6.2 eV.

are produced at zero energy with cross sections in the region of $1 \times 10^{-17} \text{ cm}^2$.

The presence of a large attachment cross section at essentially zero energy, confirmed in the present work, precludes the use of this gas as a constituent of a diffuse discharge switch.

3.5 CHLOROPENTAFLUORETHANE, $\text{C}_2\text{F}_5\text{Cl}$

As discussed in Section 2.1, the issue to be resolved with this molecule concerned the energy dependence of the total attachment cross section. In particular we are interested in the extent to which the relatively high dielectric strength involves low-energy attachment, which is highly undesirable in the presence context. Measurements were performed at room temperature following the same procedure as was used for $(\text{CF}_3)_2\text{CO}$, and the results are summarized in Figs. 3.6. The total attachment cross section obtained by simply summing the data in this figure is shown in Fig. 3.7, where the data have been smoothed above 4.5 eV. We note that below 2 eV, the cross section for Cl^- dominates and remains large down to zero energy. This observation effectively disqualifies this molecule from further consideration, and for this reason no attempt was made to investigate the temperature sensitivity of its cross sections.

3.6 CONCLUSIONS FROM THE TEMPERATURE DEPENDENCE MEASUREMENTS

Overall, the measurements described in this section were discouraging. The molecule having the strongest IR absorption, $\text{C}_2\text{F}_5\text{Cl}$, was disqualified due to its unsuitable "cold" attachment behavior, as was $(\text{CF}_3)_2\text{CO}$, which has the next strongest absorption. Of the remaining two candidates, $\text{C}_2\text{H}_3\text{Cl}$ appears the more promising, in that it showed a stronger temperature dependence for the low-energy attachment cross section than did C_3F_8 , has a better situated attachment threshold and

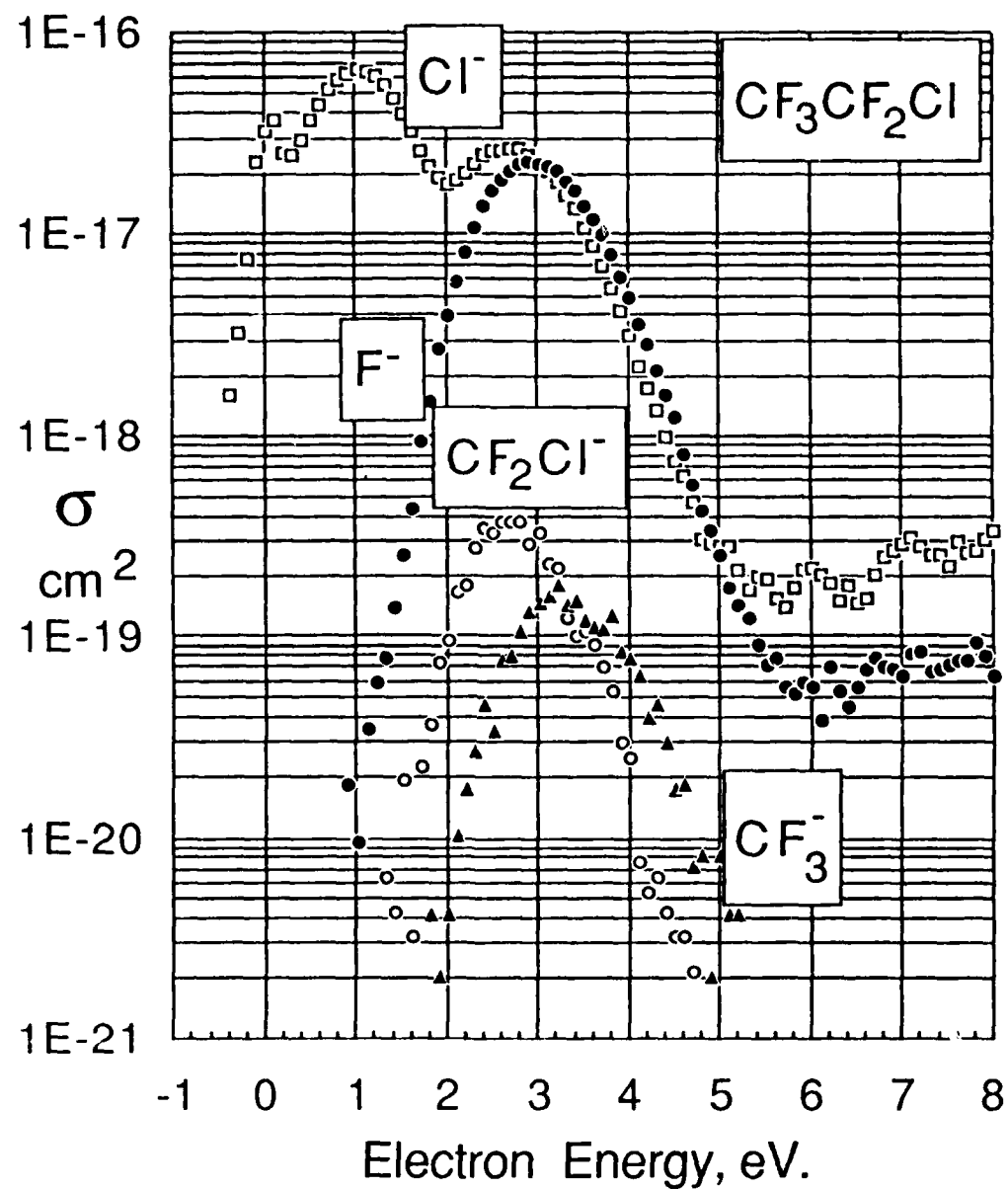


Figure 3.6 — Showing the dissociative attachment cross sections measured in $\text{C}_2\text{F}_5\text{Cl}$ at room temperature.

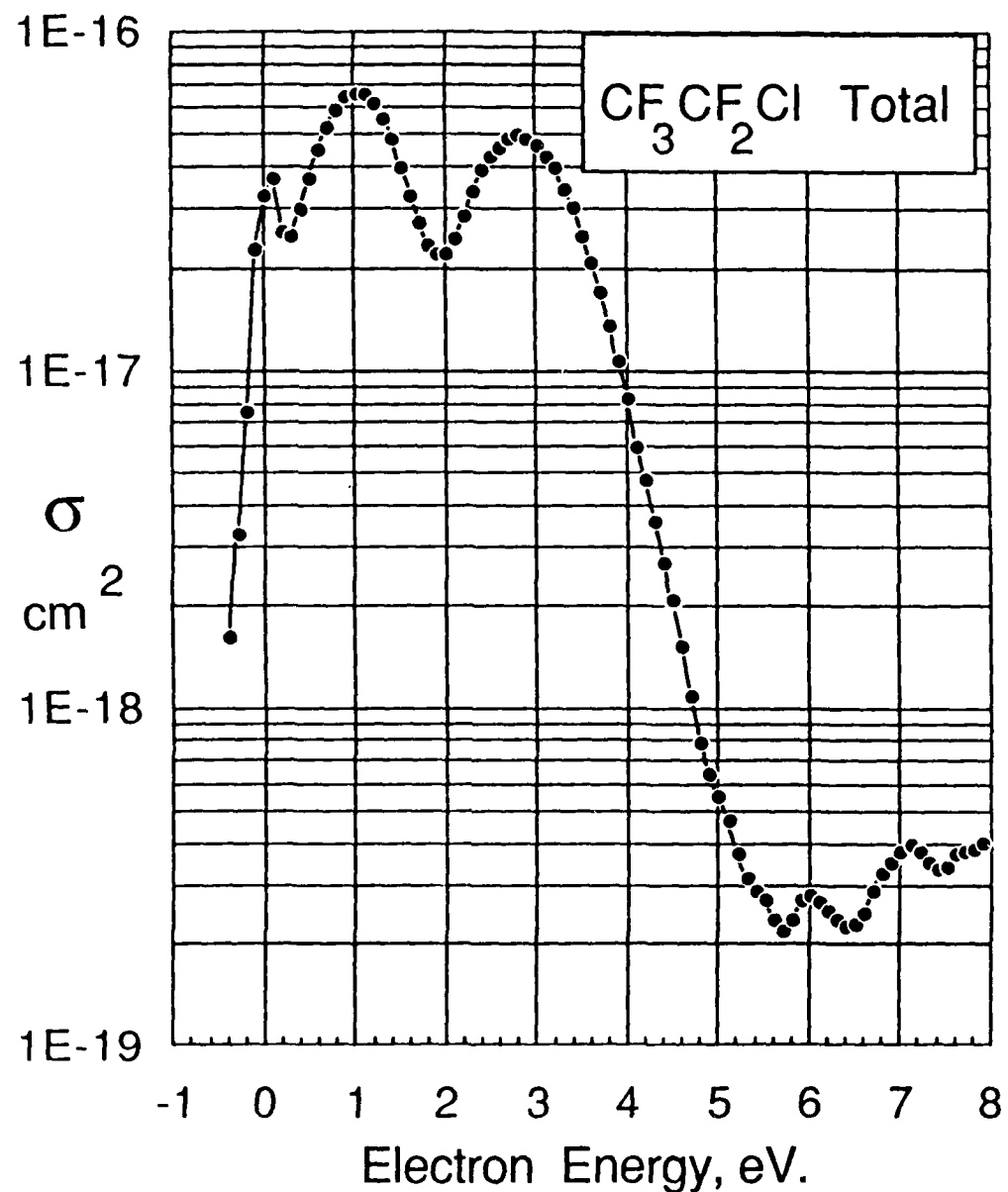


Figure 3.7 — The total attachment cross section for C_2F_5Cl at room temperature obtained by summing the individual cross sections shown in Fig. 3.6. The data above 4.5 eV have been smoothed.

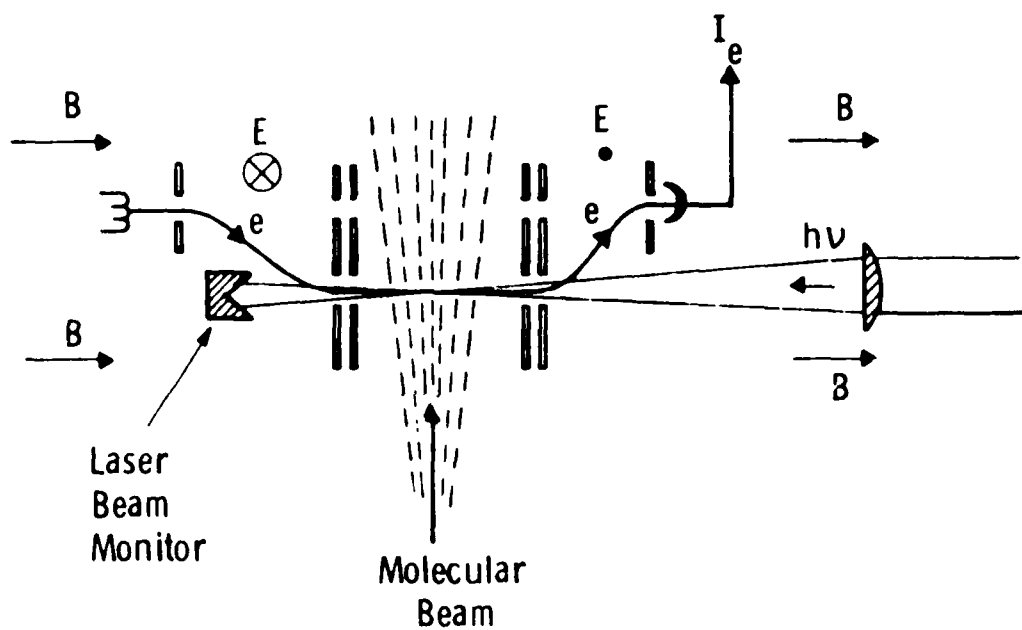
peak position, and is more strongly absorbing at wavelengths accessible to the CO₂ laser. Against this must be weighed the concern that it might be chemically unstable in a discharge environment, particularly since evidence was found in the present work for thermal dissociation at temperatures above 850 K. The decision was made to investigate laser enhancement of the attachment processes in both C₃F₈ and in C₂H₃Cl. The results of those measurements are reported in the next section.

4. PHOTO-ENHANCED ATTACHMENT MEASUREMENTS

4.1 EXPERIMENTAL PROCEDURES

The principle of the experiment is shown in Fig. 4.1. In the regions immediately before and after the collision chamber, the electron beam passes through crossed electric and magnetic fields which serve to deflect the beam. In this way optical access is provided for irradiation of the molecular beam in a region collinear with the electron beam. This arrangement successfully overcomes a severe problem caused by the laser beam interacting with the electron gun filament, experienced in earlier measurements of this type (Chen and Chantry, 1979). A scale diagram of the electrode structure used to control the electron beam, and the extraction of the product ions, is shown in Fig. 4.2. The numbered items in this figure are listed in Table 4.1. The general layout of the whole system is shown approximately to scale in Fig. 4.3. The liquid nitrogen-cooled beam trap was not used in the present study. The gas or gas mixture under study is admitted to the collision region as a crudely collimated molecular beam, generated by passing the gas through a cluster of platinum capillary tubes. Details are shown in Fig. 4.4. By situating the capillary cluster in the end of a directly joule heated platinum furnace, we are able to inject gas at either room temperature or a controllable higher temperature. A number of thermocouples are attached directly to the furnace to monitor its temperature. Tests with N_2O , involving the use of the appearance curve of O^- as a gas thermometer (Chantry, 1969a), confirmed that the thermocouple situated at the exit end of the furnace gave an acceptable measurement of the gas temperature. The coaxial furnace design

Dwn. 6420A03



Beam geometry for electron - photon - molecule interaction

Figure 4.1 — Showing the general principle of the trochoidal electron gun chosen to avoid interaction of the laser beam with the electron gun filament, and the interaction geometry of the collinear electron-laser beams with the neutral molecular beam.

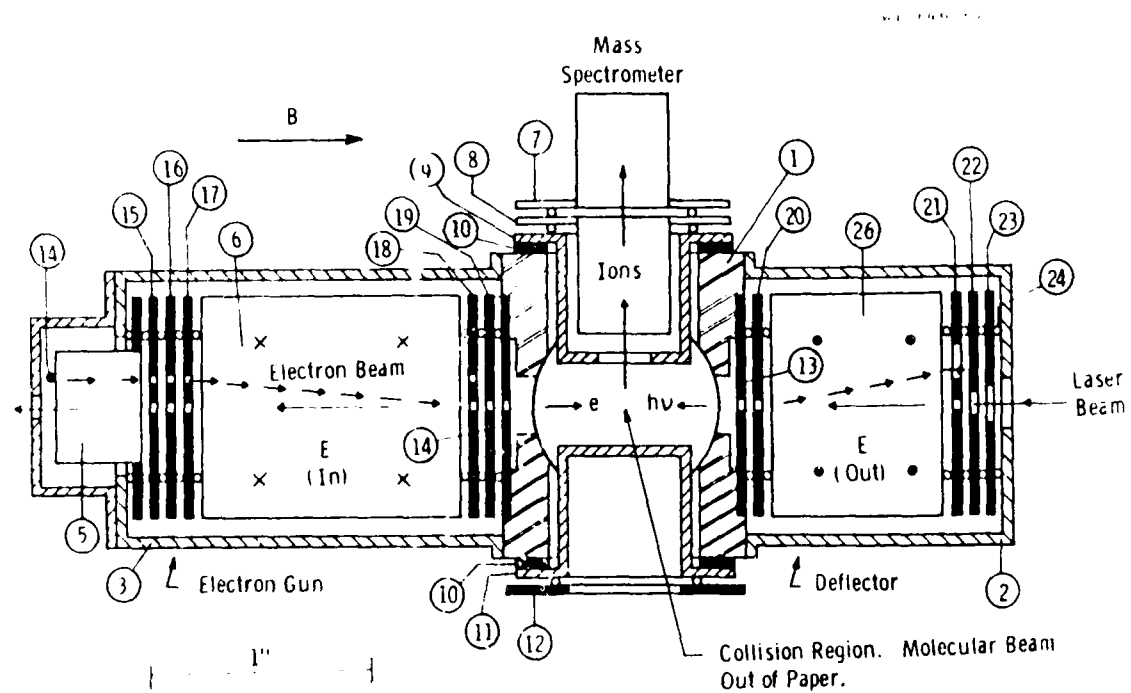


Figure 4.2 — Detailed horizontal section of the electrode structure of the electron gun and beam deflector electrodes, keyed to table 4.1.

Table 4.1 — Parts List for Electron Gun
Refer to Fig. 4.2

Part No.	Description of Part
1	Molybdenum Block - defines collision region
2	"Hat" Compressing Deflector Electrodes
3	"Hat" Compressing Electron Gun Electrodes
4	Filament
5	Filament Support (1 of 2)
26	Deflector Electric Field Electrode (1 of 2)
7	Compression Plate for Attractor Electrode and Extraction Electrodes
8	Cross-Field Extraction Electrode (1 of 2)
9	Attractor Electrode
10	Insulating Ring
11	Repeller Electrode
12	Compression Plate for Repeller Electrode
13-23	Electrode Discs to Define Electron and Laser Beams
24	Sapphire Insulator Balls
25	Filament Cover
6	Monochromator Electric Field Electrode (1 of 2)

Fig. 6-3HA 9

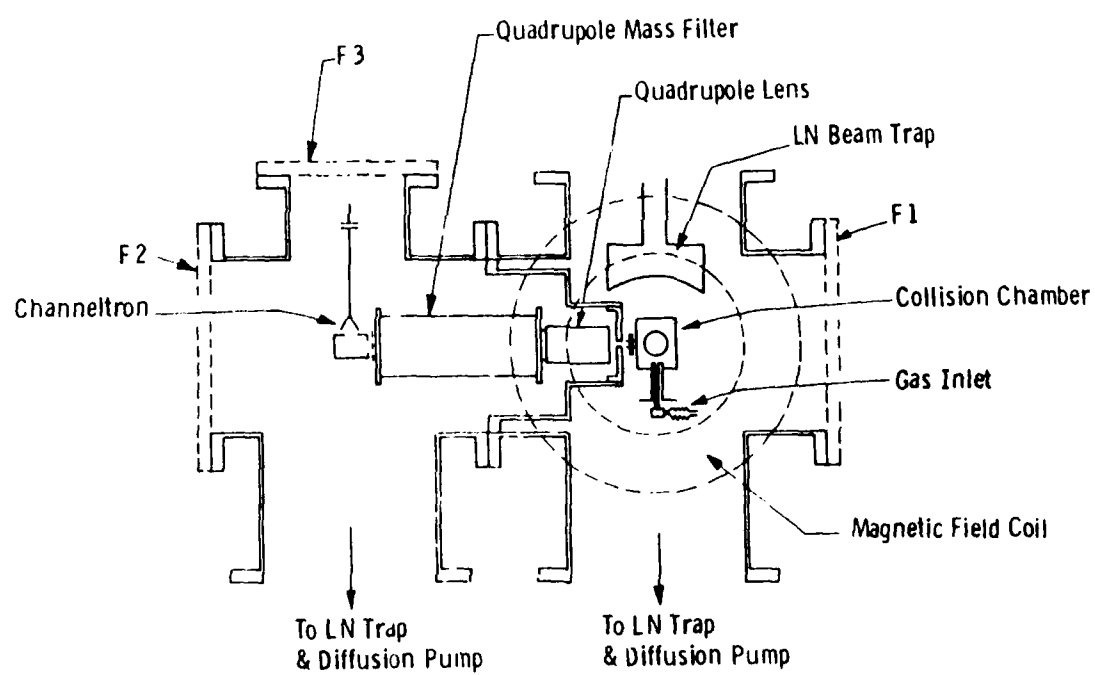


Figure 4.3 — General layout of the experimental system shown from the side, approximately to scale.

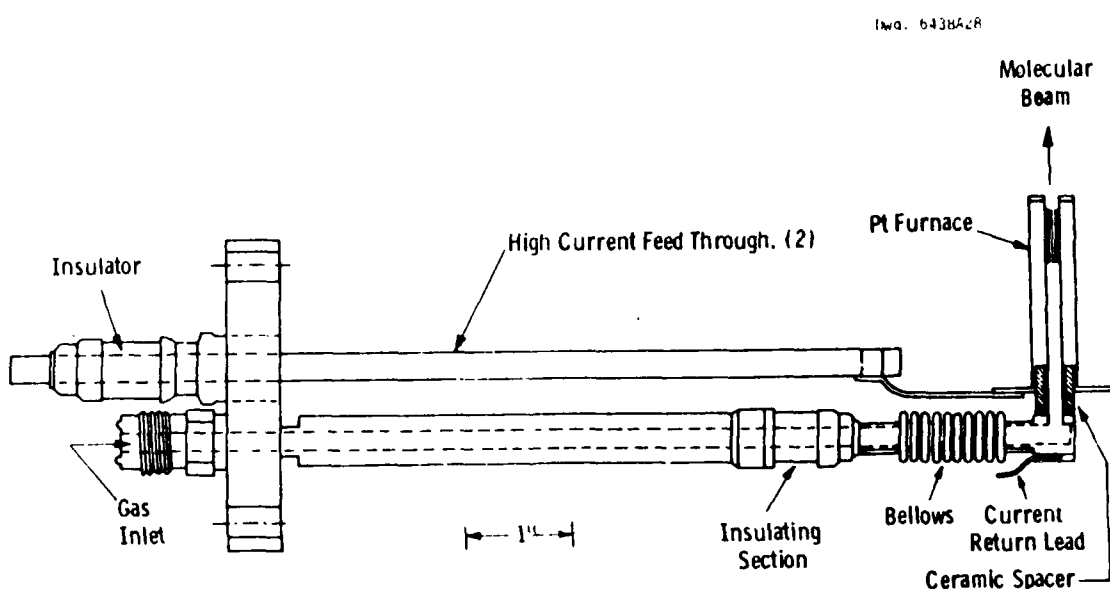


Figure 4.4 — Side view of the molecular beam source assembly. The insulated high-current feedthrough shown in the figure obscures an identical second one mounted beside it.

minimizes the magnetic field generated by the heating current in the region of the electron beam. Realignment of the magnetic field provided for control of the electron beams was not required when the furnace current of up to 18 A was turned on.

The CO_2 laser used in the present work is a modified version of a commercial laser, Molelectron Model No. C250. It provides a grating tunable cw beam of typically 10 watts for the strongest lines at the entrance window of the vacuum system. The laser beam is focussed through the system using a simple ZnSe lens of focal length 19 cm mounted with X-Y control of its position adjacent to the BaF_2 inlet window of the vacuum system. The axial position of the lens was such that the beam waist should be situated approximately 1 cm beyond the center of the region of interaction between the three beams. Beam power and profile measurements have been performed external to the collision chamber using the same lens and window, together with apertures to simulate the effects of the electron gun electrodes through which the optical beam must pass in order to reach the collision region. These indicate that the entrance window transmits 0.84 of the beam, and the apertures 0.72, for an overall transmission of 0.60 to the collision chamber. We were unable to detect any absorption in the lens. Beam profile measurements taken at various axial points indicate that at the center of the collision chamber the beam has an e-folding radius of 0.024 cm, and an axial power density of $0.32 \text{ kW/cm}^2/\text{Incident Watt}$. At the strongest lines this gives 3.2 kW/cm^2 for the axial power density. Power measurements made on the exiting beam gave values of typically 2 watts for these same lines. Checks were performed with SF_6 to ensure that in focussing and aligning the beam to give maximum transmitted power we were indeed optimizing the interaction between the optical beam, the electron beam, and the molecular beam. Note that the laser beam monitor shown schematically in Fig. 4.1 is in practice situated outside the vacuum chamber, immediately beyond the exit window.

4.2 REFERENCE MEASUREMENTS IN SF₆

In order to establish that the system was operating properly, and to provide reference data against which to judge any observed photo-enhancement effects, we first performed a number of measurements in SF₆ with the objective of reproducing the behavior observed previously (Chen and Chantry, 1979). Examples of the electron-retarding curve and its derivative, obtained with SF₆ present, are shown in Fig. 4.5. Unfortunately, the electron energy resolution achieved with the present electron gun (0.2 eV) does not match that used in the previous work, and as a result the observed effect is less dramatic. Nevertheless, we were able to record the effect very reproducibly and show that it had the same type of wavelength dependence as was previously measured.

Examples of the SF₅⁻ appearance curves recorded with and without the laser beam are shown in Fig. 4.6. In this case we used the P(24) line with the measured transmitted power of 1.6 watts. The measured peak heights are very close, and in the figure both measurements have been normalized by the same factor to give a peak height close to unity for both curves. The difference between the two signals is shown by the filled squares and shows an enhancement effect of 12% of the peak signal. As in the earlier work (Chen and Chantry, 1979), the effect occurs only at the zero energy peak of the SF₅⁻ cross section, which in the present work is unresolved. Similar data were obtained at the P(26) line with an enhancement effect of 20%. In the subsequent search for similar effects in C₂H₃Cl and C₃F₈, curves of this type were routinely measured either immediately before or after the measurement on the gas under study in order to check that the absence of an observable effect was not due to some instrumental problem, such as optical beam misalignment. The data in Fig. 4.6 show one such measurement.

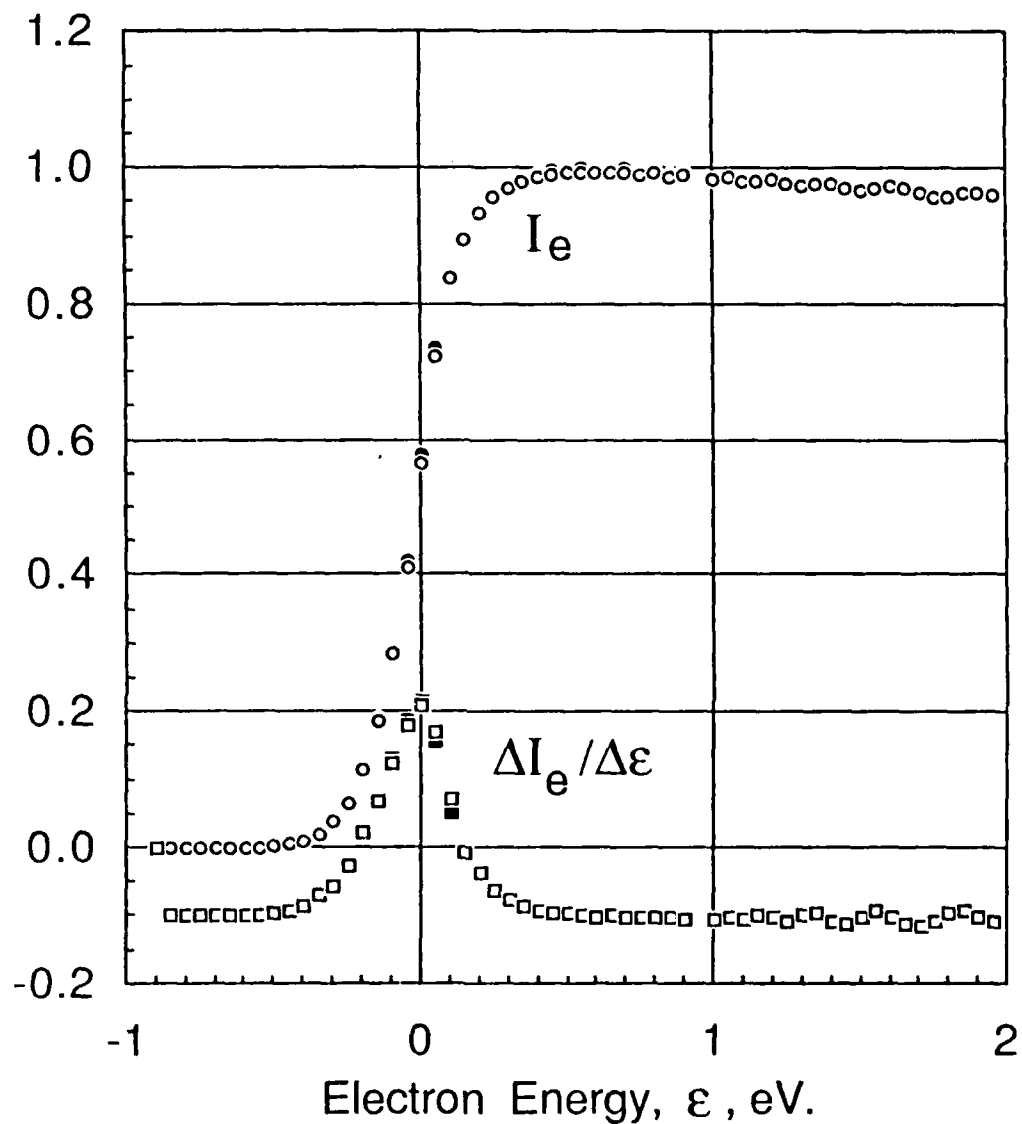


Figure 4.5 — Electron retarding curve and its derivative measured in the presence of SF_6 and laser radiation at $10.63 \mu\text{m}$. The energy scale has been adjusted to represent the most probable electron energy.

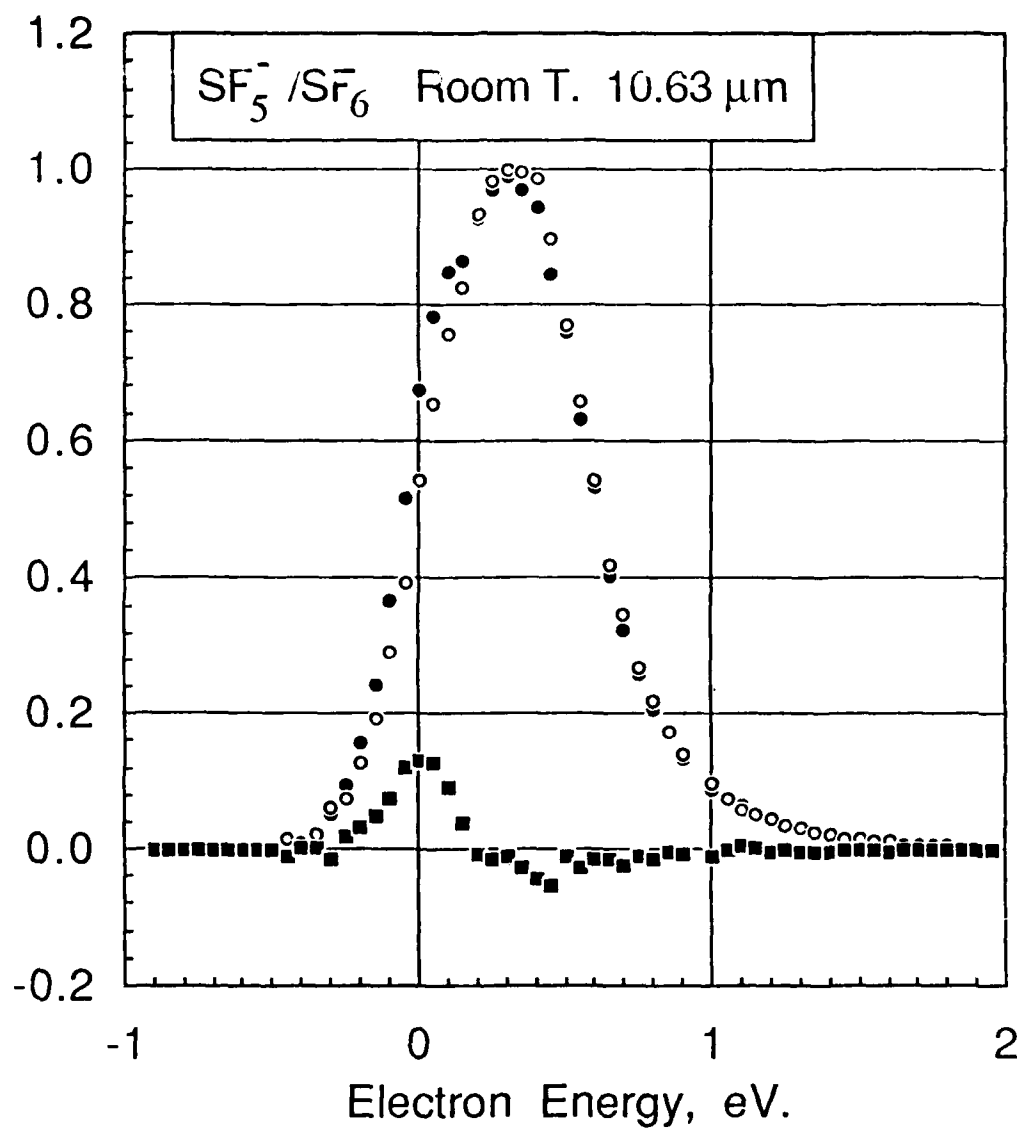


Figure 4.6 — SF_5^- production from SF_6 measured with (•) and without (○) the laser beam ($10.63 \mu\text{m}$) at room temperature. The difference signal is shown by the filled squares.

4.3 MEASUREMENTS IN C_2H_3Cl

The type of measurements described in the preceding subsection were repeated systematically in C_2H_3Cl over the full range of available laser wavelengths, and no effect of photo-enhancement was found. Particular attention was paid to the region of P(22) and P(24) where the strongest effects were found by Schaefer et al. (1988). Examples of data taken at room temperature with the P(24) line are shown in Fig. 4.7, and at 700 K in Fig. 4.8. In both cases the measured transmitted laser power was 1.4 W. In both cases the difference between the two curves, shown by the filled squares, is not significant. When it differed systematically from zero, the effect usually came from small differences in the electron beam intensity between the two runs and could be of either sign. We reluctantly reached the conclusion that we could not detect any evidence for photo-enhancement of Cl^- production from C_2H_3Cl at either temperature.

4.4 MEASUREMENTS IN C_3F_8

The same procedure was adopted in searching for photo-enhanced attachment as described above. Examples of data taken at room temperature with the P(32) line of the 001-020 transition ($9.66 \mu m$) are shown in Fig. 4.9, and similar data taken at the adjacent P(34) line ($9.68 \mu m$) at 700 K are shown in Fig. 4.10. Again, the differences between the signals recorded with and without the laser are not considered significant. Measurements of this type were performed at laser wavelengths extending from $9.66 \mu m$ to $10.59 \mu m$, covering the regions where optimum overlap with the absorption spectrum was expected. In all cases we were unable to detect any significant effect on the F^- production cross section at either temperature.

The absence of an observable effect of photo-enhanced attachment in these two gases may be due to their much smaller optical absorption

cross sections, of approximately 10^{-19} cm^2 , compared to approximately 10^{-17} cm^2 for our reference gas, SF_6 .

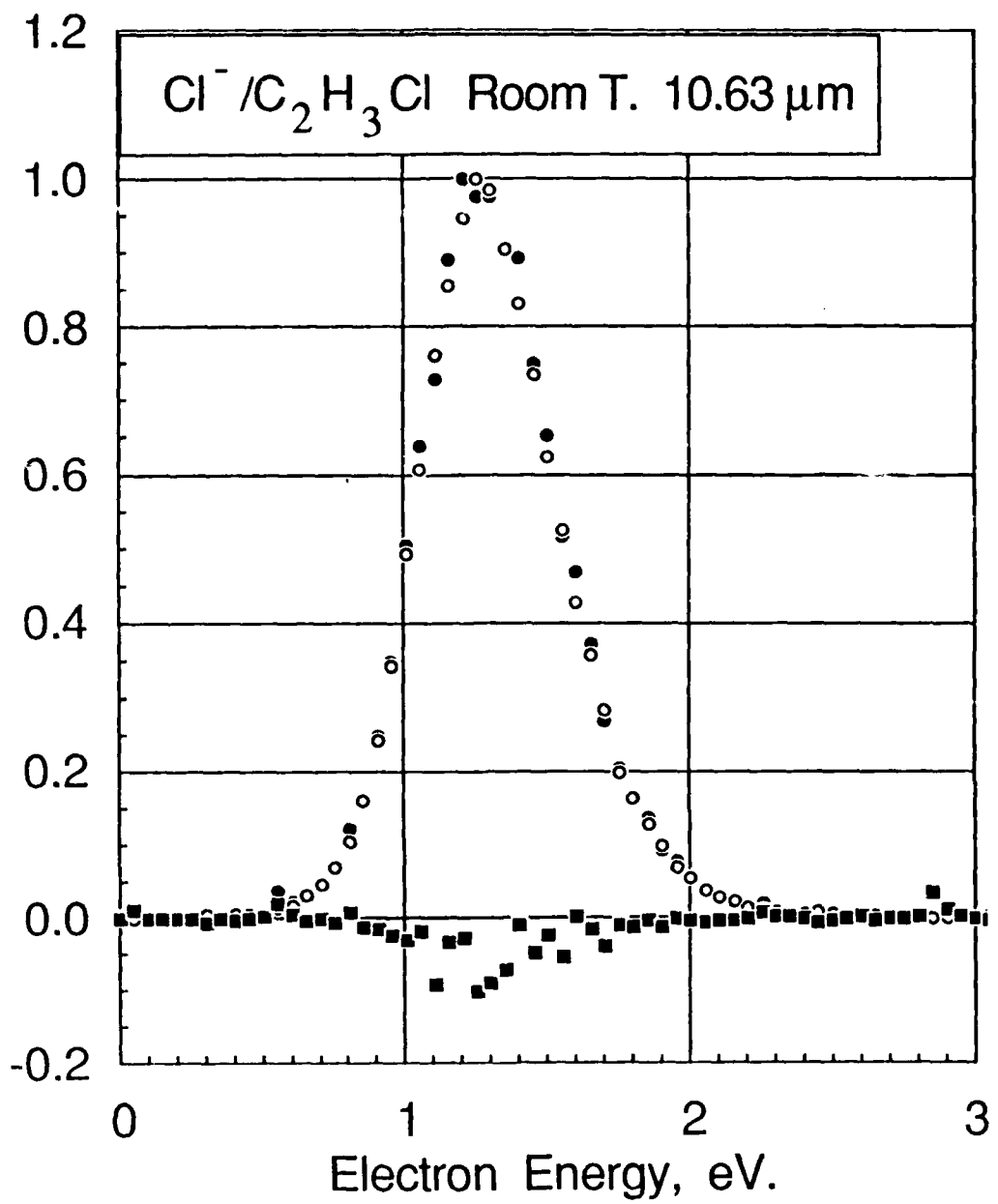


Figure 4.7 — Cl^- production from $\text{C}_2\text{H}_3\text{Cl}$ measured with (•) and without (○) the laser beam ($10.63 \mu\text{m}$) at room temperature. The difference signal is shown by the filled squares.

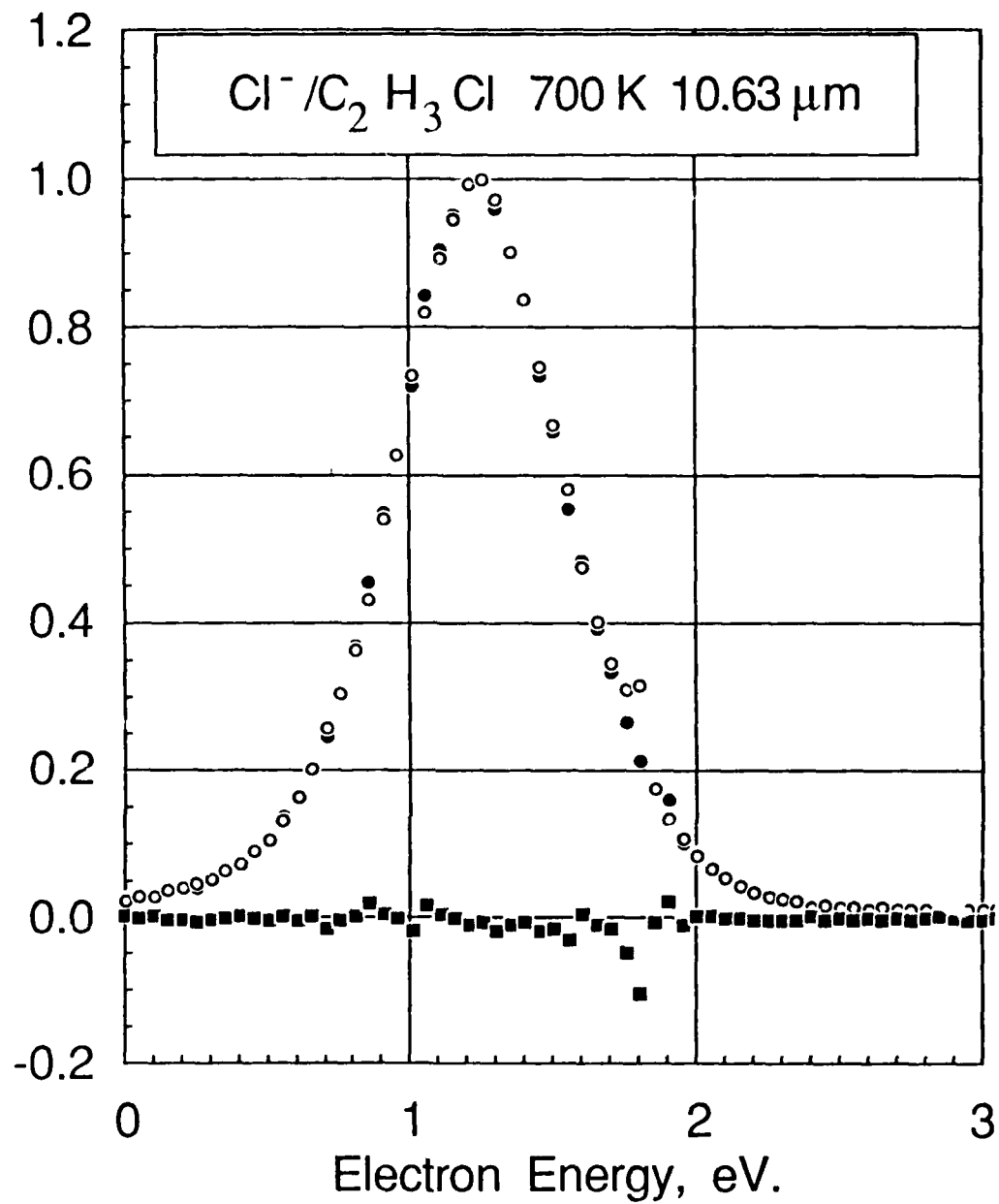


Figure 4.8 — Cl^- production from $\text{C}_2\text{H}_3\text{Cl}$ measured with (•) and without (o) the laser beam (10.63 μm) at 700 K. The difference signal is shown by the filled squares.

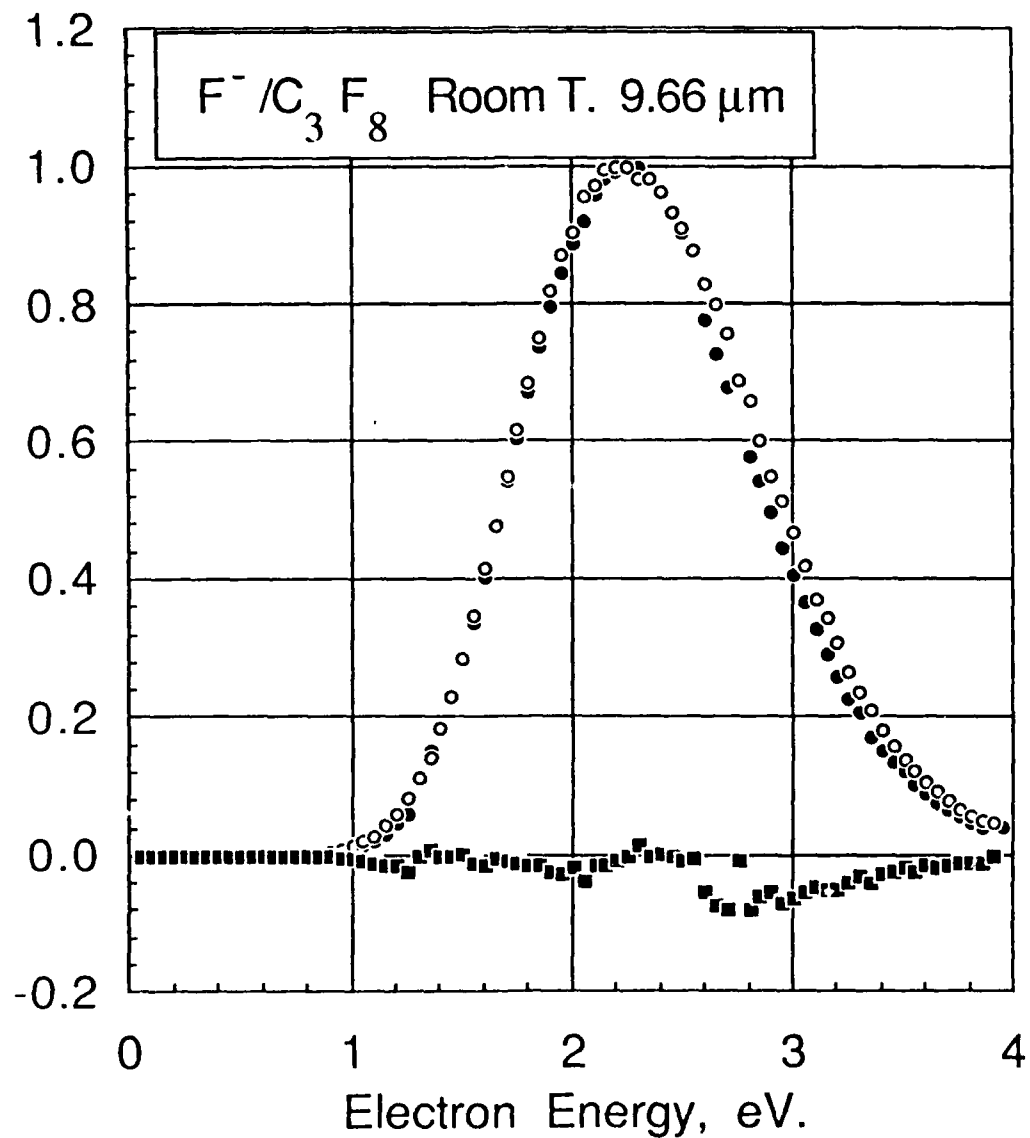


Figure 4.9 — F^- production from C_3F_8 measured with (●) and without (○) the laser beam ($9.66 \mu m$) at room temperature. The difference signal is shown by the filled squares.

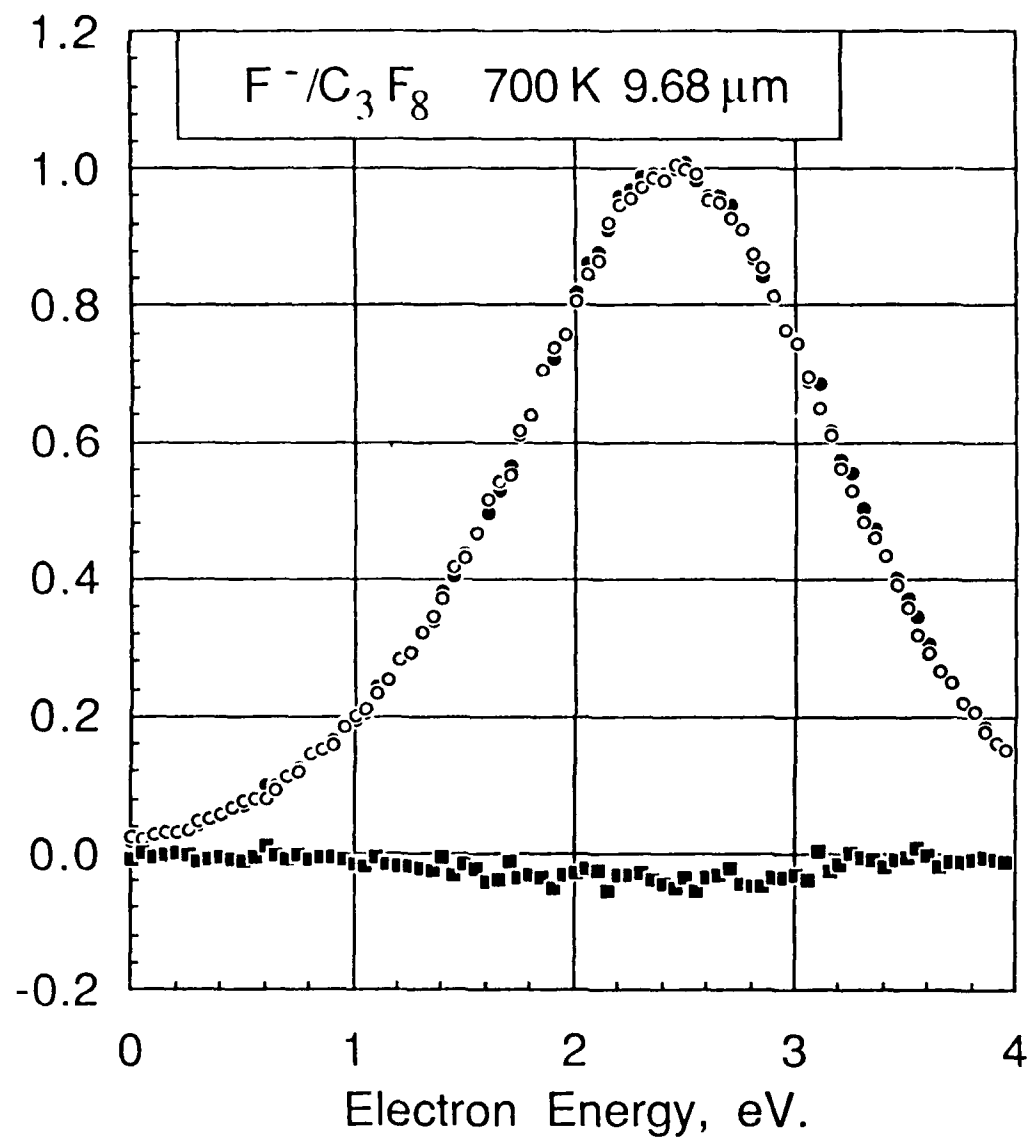


Figure 4.10 — F^- production from $C_3 F_8$ measured with (●) and without (○) the laser beam ($9.68 \mu\text{m}$) at 700 K. The difference signal is shown by the filled squares.

5. SWARM MEASUREMENTS IN METHANE

A fuller description of the work performed under this contract to measure transport parameters in CH_4 appears in Appendix 10.2, a preprint of a paper which also includes an account of Monte Carlo simulations used to reconcile the measurements with a set of cross sections. The analysis work was not performed under this contract, but the results from it, namely a cross section set believed to be the best available at this time, would be applicable to computer modelling of a diffuse discharge switch medium employing CH_4 as the main carrier gas. In this section we give only a brief summary of the swarm measurements, further details being available in the Appendix.

The drift tube consists of a uniform-field region maintained between cathode and anode by a set of ten annular guard rings whose centers are spaced 0.5 cm apart. Measurements were performed over an E/N range from 10 to 1000 Td. Both anode and cathode are electrically shielded from the drift region by a highly transparent grid (87% optical transparency) located 0.1 cm from each electrode. The cathode contains a sapphire insert centered along the axis of the drift tube whose face adjacent to the drift region is coated with a thin gold film. The anode and its associated screen structure are coupled to the chamber envelope via a linear bellows drive, enabling the drift distance to be varied. The tube is designed so that either cathode or anode may be connected to high potential, enabling current transients to be measured at either one.

Research grade (Grade 4.2) methane, supplied by Airco with a minimum specified purity of 99.992%, has been used for the measurements. Back illumination of the semitransparent cathode by a pulse of uv

radiation from an externally mounted source releases a pulse of electrons into the drift region. The resulting time-resolved current collected at either the anode or the cathode is amplified and fed to a waveform digitizer and signal averager, and stored on nine-track tape. Waveforms are accumulated in the signal averager at a repetition rate $\sim 30-100 \text{ s}^{-1}$ until the signal/noise ratio has attained a satisfactory value; typically, this requires the summation of between 10^4 and 10^5 digitized current waveforms.

The currents measured at the electrically shielded cathode and anode collectors are associated with the motion of charge carriers between each collector and its adjacent screen. Thus, in the general case where a mixture of electrons, negative ions, and positive ions are present in the drift region as a result of electron-molecule collisions, all three components of the total current can be resolved directly. At the anode, the attenuated or amplified (depending on E/N) electron signal together with the negative-ion signal are recorded, while at the cathode the initial electron signal (produced as a result of the pulsed uv irradiation) and subsequent positive-ion signal are recorded.

The estimated uncertainties in our measured values of the electron drift velocity are $\pm 1\%$ for $E/N \leq 300 \text{ Td}$ and $\pm 2\%$ for $E/N > 300 \text{ Td}$. In regions of overlap, the present data are in closest agreement (to within the combined uncertainties) with those of Haddad (1985) and of Pollock (1968).

The positive-ion drift velocity is determined from the slope of a plot of the arrival time of the peak of the positive-ion component of the cathode current as a function of drift distance at each fixed value of E/N. The present data have an estimated uncertainty of $\pm 1\%$. The present ion mobility values refer to the slowest ion (the only clearly resolvable ion), and probably to the more massive of the two dominant product ions, C_2H_5^+ .

The anode current waveforms do not show any negative-ion component despite the fact that dissociative attachment has been

observed (Sharp and Dowell, 1967) under single collision conditions, leading to the formation of H^- and CH_2^- ions. The net ionization coefficient ($\alpha-\eta$) has been determined from the electron and positive-ion charge waveforms collected at the cathode. Since we have been unable to detect significant attachment, these measurements give equivalently the ionization coefficient α/N . The estimated uncertainties in these values are $\pm 3\%$ for $E/N \geq 100$ Td and $\pm 4\%$ for $E/N < 100$ Td.

There is generally good agreement among the various measurements of ($\alpha-\eta$) over the range $150 \leq E/N \leq 600$ Td. For $E/N > 600$ Td, the present data lie up to 20% below previous values. However, of particular interest is the comparison of the data sets for $E/N < 150$ Td. In this region, Hunter et al. (1986) have recently reported significantly lower values of net ionization which they attribute to the occurrence of attachment. We have been unable to detect a significant negative-ion current for values of E/N down to 80 Td, and for $E/N < 150$ Td our results are in good agreement with the only other previous measurements (Cookson et al., 1966; Heylen, 1975) in this range. Although the experimental methods were different, the analysis of the raw data which were used by both Cookson et al. and Heylen is similar to that used in the present study, and also gives unambiguous values of the net ionization coefficient. On the other hand, Hunter et al. have used a curve-fitting routine for extracting the coefficients α and η directly from the raw data. It is our contention that the discrepancies between the values of the ionization and attachment coefficients deduced by Hunter et al. compared with the present and previous values are largely due to the methods of analysis of the raw data. It has been pointed out (Davies, 1988) that the coefficient which is most accurately determined from either spatial or temporal current growth measurements is the net ionization coefficient, i.e., the coefficient which appears in the exponent of the current growth expression, and that values of the individual coefficients are subject to much larger uncertainty,

particularly in the range of E/N where the net coefficient becomes small.

From the present measurements we place an upper bound for $\eta/N = 5 \times 10^{-21} \text{ cm}^2$ at $E/N = 80 \text{ Td}$, a factor of 21 less than that reported by Hunter et al. (1986). In fact, we note that for $E/N = 80 \text{ Td}$, the value of the net ionization coefficient reported by Hunter et al. is negative (i.e., $\alpha < \eta$), which is completely incompatible with our raw data and evidently with those of Cookson et al. and Heylen. Thus, we identify our measurements of the net ionization coefficient with the true ionization coefficient α/N . Over the range of E/N from 80 to 600 Td, our values of α/N are represented to within $\pm 4\%$ by the expression

$$\alpha/N = 251 \exp[-624/(E/N)]$$

where α/N is expressed in units of 10^{-18} cm^2 and E/N is in Td.

The discrepancy between the measured η/N upper bounds and the values predicted from the measured cross sections is largely accounted for if one postulates that H^- suffers rapid collisional detachment under the conditions of the swarm measurements. The H^- ions are particularly susceptible to detachment since they have a relatively low binding energy, are probably formed with appreciable kinetic energy, and can readily gain energy from the applied field.

6. PUBLICATIONS AND PRESENTATIONS

"Ionization and temperature Dependent Attachment Cross Section Measurements in C_3F_8 and C_2H_3Cl ." P. J. Chantry and C. L. Chen. To be submitted to J. Chem. Phys. See Appendix 10.1 for preprint.

"Measurements of Swarm Parameters and Derived Electron Collision Cross Sections in Methane." D. K. Davies, L. E. Kline, and W. E. Bies. To be submitted to J. Appl. Phys. See Appendix 10.2 for preprint.

An additional publication is planned of the cross-section measurements in $(CF_3)_2CO$ and C_2F_5Cl but has not yet been prepared.

"Measurements of Swarm Parameters And Derived Electron Collision Cross Sections in Methane." D. K. Davies and L. E. Kline. Presented at the 5th International Seminar on Swarm Experiments, July 1987, Birmingham, England. This paper appeared in the program of the meeting provided for all attendees.

"Cross Section Measurements in C_3F_8 and C_2H_3Cl ." P. J. Chantry and C. L. Chen. Presented at the 40th Annual Gaseous Electronics Conference, October 1987, Atlanta, Georgia. Abstract appeared in Bull. Am. Phys. Soc. 33, 152 (1988).

"Electron Collision Cross Sections for CH_4 from Measured Swarm Data." L. E. Kline, D. K. Davies, W. E. Bies and T. V. Congedo. Presented at the 40th Annual Gaseous Electronics Conference, October 1987, Atlanta, Georgia. Abstract appeared in Bull. Amer. Phys. Soc. 33, 151 (1988).

7. PARTICIPATING PERSONNEL

The following people participated in the work supported by this contract:

P. J. Chantry was the principal investigator and participated in all the electron beam measurements of temperature dependence and photo-enhancement of attachment cross sections.

C. L. Chen participated in the cross-section measurements in C_3F_8 .

C. B. Freidhoff participated in the cross-section measurements in $(\text{CF}_3)_2\text{CO}$ and $\text{C}_2\text{F}_5\text{Cl}$, and in the photo-enhancement experiments.

D. K. Davies performed all of the drift tube measurements on CH_4 .

L. E. Kline participated in the selection of gases to be studied and performed all of the cross-section analysis of CH_4 .

All the above participants are listed as co-authors of this report.

8. ACKNOWLEDGMENTS

We wish to acknowledge the technical assistance of W. M. Uhlig, R. L. Fry, and L. D. Kurtz in the construction and maintenance of the experiments. A number of informative and stimulating discussions were held with P. D. Burrow and with G. Schaefer, both of whom kindly provided information regarding directly relevant work prior to its publication.

9. REFERENCES

Bletzinger, P. (1983), Proc. 4th Pulse Power Conf., Albuquerque, p. 37-40.

Chantry, P. J. (1969b), Rev. Sci. Instrum. 40, 884-889.

Chantry, P. J. (1969a), J. Chem. Phys. 51, 3369-3379.

Chantry, P. J. (1971), J. Chem. Phys. 55, 1851-1860.

Chantry, P. J. (1982). See ch. 2 of "Gas Lasers," E. W. McDaniel and W. L. Nighan, Ed. Academic Press, NY.

Chen, C. L. and Chantry, P. J. (1979), J. Chem. Phys. 71, 3897.

Christophorou, L. G., Hunter, S. R., Pinnaduwage, L. A., Carter, J. G., Christodoulides, A. A., and Spyrou, S. M. (1987), Phys. Rev. Lett. 58, 1316.

Christophorou, L. G., Hunter, S. R., Carter, J. G., and Mathis, R. A. (1982), Appl. Phys. Lett. 41, 147.

Cookson, A. H., Ward, B. W., and Lewis, T. J. (1966), Br. J. Appl. Phys. 17, 891.

Davies, D. K. (1988), "Drift Tube for Measurement of Swarm Parameters in Electronegative Gases," submitted to Rev. Sci. Instrum.

Dewar, M. J. S. and Worley, S. D. (1969), J. Chem. Phys. 50, 654-667.

Dressler, R., Allan, M., and Haselbach, E. (1985), CHIMIA 39, 385-389.

Eisele, F. L. (1984), Final Report AFWAL-85-2015.

Haddad, G. N. (1985), Austr. J. Phys. 38, 677.

Harland, P. and Thynne, J. C. J. (1970), J. Phys. Chem. 74, 52-59.

Heylen, A. E. D. (1975), Int. J. Electron. 39, 653.

Hunter, S. R., Carter, J. G., and Christophorou, L. G. (1986), *J. Appl. Phys.* 60, 24.

Hunter, S. R. and Christophorou, L. G. (1984), *J. Chem. Phys.* 80, 6150.

Kaufel, R., Illenberger, E., and Baumgartel, H. (1984), *Chem. Phys. Lett.* 106, 342-346.

Kline, L. E. (1982), *IEEE Trans. Plasma Sci.* PS-10, 224.

Kobayashi, O., Sasagawa, T., and Obara, M. (1987), *Appl. phys. Lett.* 51, 2103-2105.

Kurepa, M. V. (1965), *3rd Cz. Conf. Electr. Vac. Phys.*, p. 107-115.

Olthoff, J. K., Tossell, J. A., and Moore, J. H. (1985), *J. Chem. Phys.* 83, 5627-5634.

Pollock, W. J. (1968), *Trans. Faraday Soc.* 64, 2919.

Rossi, M. J., Helm, H. and Lorents, D. C. (1985), *Appl. Phys. Lett.* 47, 576.

Schaefer, G., Giesselmann, M., Pashaie, B., and Kristiansen, M. (1988). "CO₂ Laser Enhanced Electron Attachment in Externally Sustained Diffuse Gas Discharges Containing Vinyl Chloride," submitted to *J. Appl. Phys.*

Schoenbach, K. H., Schaefer, G., Kristiansen, M., Hatfield, L. L., and Guenther, A. H. (1982), *IEEE Trans. Plasma Sci.* PS-10, 246 (1982).

Sharp, T. E. and Dowell, J. T. (1967), *J. Chem. Phys.* 46, 1530.

Spyrou, S. M. and Christophorou, L. G. (1985), *J. Chem. Phys.* 83, 2829.

Stricklett, K. L., Chu, S. C., and Burrow, P. D. (1986), *Chem. Phys. Lett.* 131, 279.

Thynne, J. C. J. and MacNeil, K. A. G. (1971), *J. Phys. Chem.* 75, 2584-2591.

Trainor, D. W. and Jacob, J. H. (1979), *Appl. Phys. Lett.* 35, 920-922.

Wootton, R. E., Dale, S. J., and Zimmerman, N. J. (1980), "Gaseous Dielectrics II," Pergamon Press, p. 137-148.

APPENDIX 10.1

IONIZATION AND TEMPERATURE DEPENDENT ATTACHMENT CROSS SECTION MEASUREMENTS IN C_3F_8 AND C_2H_3Cl

P. J. Chantry and C. L. Chen*
Westinghouse R&D Center
1310 Beulah Road
Pittsburgh, Pennsylvania 15235

ABSTRACT

Total ionization and attachment cross sections have been measured in C_3F_8 at 330°K using an electron beam and a total ion collection technique, calibrated by similar measurements on N_2O and Xe. Our total ionization cross section is similar in general shape to a previous measurement of this type, but with typically half the magnitude. The ionization threshold cannot be accurately derived from these measurements, due to severe upward curvature immediately above threshold. The positive-ion signal rises above the background at 13.0 ± 0.1 eV, to be regarded as a lower limit to the true threshold. An overall ionization cross section with a threshold at 13.3 eV is recommended, based on threshold data from photo-electron spectroscopy

*Present address: Brookhaven National Laboratory

and the present data between 14 and 80 eV. The room temperature total attachment cross section peaks at 2.8 eV with a value of 1.75×10^{-17} cm². This is 14 times smaller than the only other measurement of this type we are aware of. There is much better agreement with two more recently reported values unfolded from swarm experiments. The temperature dependence of the predominant dissociative attachment process, involving F⁻ production, was studied in a different apparatus using a mass filter and ion pulse counting. At 730°K the peak cross section has increased by ~60% and the threshold is lower by 1.1 eV. This second type of measurement was used to study the predominant dissociative attachment process in C₂H₃Cl, involving Cl⁻ production. At 290°K this has a threshold at 0.85 eV and a peak at 1.35 eV of 3.2×10^{-17} cm², in good agreement with recent work elsewhere. At 850°K the cross section at the peak is x 2.6 larger, and lower in energy by 0.3 eV, while at 0 eV it has reached 8×10^{-18} cm². At higher temperatures effects ascribed to thermal dissociation of the C₂H₃Cl were observed. The implications of the present results regarding the use of these gases in diffuse discharge switches are discussed.

1. INTRODUCTION

The primary objective of the work reported here was to measure the attachment cross sections for the subject gases and establish their sensitivity to gas temperature. Our interest in these gases stems from their possible use as optically controlled attaching additives in an externally sustained diffuse gas discharge switch.¹ In this application the switch medium is required to cause minimal electron loss rate when the switch is in the conducting phase, but to recover its insulating properties as rapidly as possible when the external source of ionization is turned off. During the recovery the electron density in the medium must decrease while the switch voltage, and consequently the electric field experienced by the electrons, is increasing. At the gas pressures employed the electrons remain essentially in equilibrium with the field during the switch recovery, and as a consequence their mean energy increases from typically a few tenths of an eV to a few eV. It is therefore desirable that the medium's net attachment rate be small for low electron energies, and increase rapidly with mean energy above a few tenths of an eV. With these and other considerations in mind, possible candidates can be identified² for consideration and further testing³ as attaching additives.

Additional improvement in switch performance can in principle be realized by optically enhancing the attachment rate in the medium during the recovery phase. Possible means of achieving this are (i) by photodissociation causing formation of strongly attaching neutral fragments,⁴ (ii) by short-wavelength optical excitation of higher energy electronic states,⁵ or (iii) by vibrational excitation of the attacher by tuned infrared irradiation.^{6,7} In the present work we investigate two possible candidates for the third of these approaches. They were chosen on the basis of the existing knowledge regarding their attaching properties, such that they would be expected to have the type of passive attachment behavior described above, and from their infrared absorption spectra,⁸ which are such that one may plan to use a CO₂ laser as an efficient source for the excitation. As a first step in screening these and other candidates, it is important to establish the sensitivity of their attachment cross sections to non-selective vibrational excitation, achieved by simply heating the gas. In addition, it is important to establish the shape and magnitude of the attachment cross section for the "cold" gas in order that the electron transport properties of the switch medium may be properly modeled by a Boltzmann or Monte-Carlo code analysis.

There is considerable prior literature on the attachment properties of C₃F₈, including a total attachment cross-section measurement⁹ made by the classical Tate and Smith¹⁰ technique. When starting the present study we anticipated confirming the validity of that measurement, and moving quickly to the study of the temperature

sensitivity of the process. However, our initial cross-section measurements revealed a surprisingly large discrepancy, exceeding an order of magnitude, in the peak magnitude. Because of this we determined that a more extensive series of room temperature measurements was needed to provide more definitive cross-section data, for both total attachment and total ionization. The results of that study, and subsequent measurements conducted at elevated gas temperatures, are reported here. Since the initiation of this study, swarm experiments conducted elsewhere^{11,12} have yielded C_3F_8 attachment cross-section data with which the present results may be compared.

The information available on C_2H_3Cl included a number of recent electron beam studies of both negative ion production^{13,14,15,16} and electron scattering.^{16,17} In the present context the paper of Stricklett et al.¹⁶ is particularly interesting in that it implicitly contains a measurement of the peak attachment cross section, relative to the known value for O^- production from CO_2 . Also, these authors argue, and proceed to demonstrate, that the process of dissociative attachment in the chloroethylenes should be enhanced by out-of-plane positioning of the Cl atom. By analogy, Burrow¹⁸ has suggested that excitation of internal vibrational modes causing such a distortion in C_2H_3Cl could lead to significant enhancement of its attachment cross section. Based on this information and the known IR absorption properties, this molecule was clearly of sufficient interest to be included in the study.

In Section 2 we describe the experimental techniques used for the present measurements, the results being presented in Section 3. The

relation of these results to other available data, and the implications regarding the possibilities of employing these gases as attaching additives, are discussed in Section 4. The results and conclusions drawn from this study are summarized in Section 5.

2. EXPERIMENT

In the present study measurements were performed with two types of apparatus. The first apparatus permits measurements of the total ion current as a function of the absolute pressure in the collision chamber. Comparison of these signals with others, obtained similarly using a gas for which the cross section is known, provides a measure of the absolute cross section. The second type of measurement employs a "high-temperature tube" having a heatable collision chamber which allows us to measure the dependence of the ion production processes on the gas temperature. In both cases the electron beam is produced by a directly heated filament and an electron gun employing the retarding potential difference (RPD) technique^{19,20} to enhance the energy resolution. With either apparatus mass-analyzed ion detection can be performed using a quadrupole mass filter employing ion-counting techniques. In the measurements reported here this feature was used exclusively with the high-temperature tube. These techniques are described here only briefly, details being given only of those aspects which have not been described in previous publications.

(i) Total Ion Collection Cross Section Measurements

We have used this approach in the past to measure attachment cross sections in various gases including CO^{21} , SF_6^{22} , F_2 and NF_3^{23} , and some of the details of the technique may be found in these references.

The collision chamber and ion collection electrode geometry used for these measurements is shown to scale in Fig. 1, which represents a section perpendicular to the electron beam through the center of the collision chamber. The chamber is machined from a stainless steel block and is gold plated. All associated electrodes are supported directly from the block, including those constituting the electron gun and electron beam collector electrodes which are not shown in this view. The electron beam enters and leaves the chamber through ample apertures whose potentials are nominally identical to the chamber potential. Ions formed within the chamber by the electron beam experience a transverse extraction field applied by the parallel plate repeller and attractor electrodes. The dependence of the collected ion signal on the magnitude of this field is recorded for each process studied. Subsequent quantitative measurements of the ion current are made with the extraction field set at a value adequate for the signal to be only weakly dependent on the field. Care is also taken to adjust the repeller and attractor potentials relative to the chamber potential such that the electron beam has its minimum energy within the chamber. This ensures that we are able to operate the beam down to essentially zero electron energy, and that the electron-retarding curve will provide a

reliable zero energy scale calibration point. An externally controlled magnetic field of a few hundred gauss is imposed parallel to the electron beam. This serves to align the beam and constrain it to an essentially equipotential surface within the chamber. The magnetic field also serves the Wien velocity filter, but the latter was not used significantly in the present study.

Two holes in the top of the collision chamber match similar holes in the stainless steel base of a Dewer vessel to which it is connected in good thermal contact. There are two metal tube connections to the collision chamber. One allows gas to be fed to the chamber, while the other allows the chamber pressure to be measured using a Baratron capacitance manometer. The gas and collision chamber temperature can be controlled by use of appropriate fluids in the Dewer vessel.

(ii) Mass Resolved and Elevated Temperature Measurements

We have used this "high-temperature tube" in the past to measure both positive and negative fragment ion cross sections in various gases including N_2O^{24} and SF_6^{22} , and to study the temperature dependence of such reactions. Details of the technique may be found in Chantry,²⁴ and reference may be made particularly to Fig. 3 therein. In this case the collision chamber consists of an iridium tube of length 5 cm. Gas admitted to the collision chamber escapes through two apertures used to pass the electron beam through the collision chamber, and a third slit

in the sidewall which allows a sample of the ions to escape perpendicularly to the electron beam.

The electron beam is aligned by an externally applied magnetic field of about 500G. The collision chamber is rigidly mounted to a glass plate and can be heated by passing a high (0-100A) direct current through the collision chamber. A platinum, platinum/rhodium thermocouple is spot welded to the outer surface of the collision chamber wall opposite the ion exit slit and is used to monitor the chamber temperature.

The electron gun and electron beam collection optics assemblies are mounted on a U-bracket which is placed around the collision chamber. The U-bracket independently maintains the alignment of the gun and collection optics, and provides a convenient means to align the electron gun system to the collision chamber.

The collision chamber is surrounded by a similar tube of larger dimension which acts as a radiation shield (RS). The radiation shield can be biased relative to the collision chamber to permit extraction of the proper polarity ions through an aperture in the side of the collision chamber. Two planar grids outside of the ion extraction aperture are situated so that an electric field, perpendicular to the magnetic field, can be produced to prevent deflection of the extracted ions by the fringing magnetic field used to align the electron beam. The extracted ion sample is subsequently focussed through a differential pumping aperture into a chamber housing the quadrupole mass filter. The mass-selected ions impinge on a channeltron multiplier used in a pulse-

counting mode. Care is taken to saturate the ion count rate by operating the channeltron at sufficient voltage, and the mass filter such that the ion signal strength is not significantly dependent on the mass resolution. With these measures the mass discrimination of the system is minimized.

3. RESULTS

(i) Perfluoropropane, C_3F_8 , Measurements

An example of data obtained with C_3F_8 in the total collection tube is shown in Fig. 2. The three curves indicate "difference" signals of the transmitted electron beam, the negative-ion signal collected at the positively biased electrode, and the positive-ion signal collected at the opposing electrode, all measured under identical operating conditions of the tube. The energy scale, obtained in this case by setting zero at the steepest part of the electron beam-retarding curve, gives the expected threshold for Xe^+ production, 12.13 eV, to within the target accuracy of ± 0.1 eV.

In order to place the total ion current measurements on a cross-section scale, calibration measurements of the type illustrated in Fig. 3 were performed. The peak attachment cross section in C_3F_8 is here calibrated against the known peak cross section for O^- production from N_2O . The two signals are measured under the same collision chamber conditions, with the extraction electrode potentials chosen as described above. The ratio of the slopes (2.03) is multiplied by $8.6 \times 10^{-18} \text{ cm}^2$, the known cross section for O^- production from N_2O^{25} , to give the value of the peak attachment cross section of C_3F_8 , $1.75 \times 10^{-17} \text{ cm}^2$.

Similar calibration measurements were performed for the positive ion signals, using Xe as the calibrant gas, together with the cross-section measurements of Rapp and Englander-Golden.²⁶ In Fig. 4(a) the full curve shows the cross-section shape, measured by scanning the electron energy at a fixed pressure, and normalized to the points at 40, 60, and 80 eV obtained from pressure scans of the type shown in Fig. 3. Figure 4(b) shows a more-detailed view of the data recorded in the region immediately above threshold. The severe curvature makes a determination of the true threshold somewhat difficult. We obtain from our measurements a value of 13.0 ± 0.1 eV.

Our total negative ion measurements at $T = 330^{\circ}\text{K}$ give the calibrated attachment cross-section data for C_3F_8 shown on a linear plot in Fig. 5. This same result is plotted semilogarithmically as the full curve in Fig. 6, together with two recently published results.^{11,12}

Additional mass-resolved data were taken using the "high-temperature tube." With no direct heating the collision chamber has a normal operating temperature close to 290°K , with the electron gun operating. This is slightly below room temperature due to its location above a large liquid nitrogen-cooled trap. Under these "room temperature" conditions, measurements were made of the F^- appearance curve and of the O^- appearance curve using mixtures of C_3F_8 and N_2O in the collision chamber. The separation of these peaks confirmed the position of the F^- peak at 2.8 eV.

The data on F^- from C_3F_8 obtained at room temperature and at various elevated temperatures using the high-temperature tube are shown

in Fig. 7 as the family of full curves. These curves were placed on an absolute magnitude scale by setting the room temperature peak value equal to the value of $1.75 \times 10^{-17} \text{ cm}^2$ determined above. The relative magnitudes of the curves taken at different temperatures were determined by also measuring at each temperature the strength of the CF_3^+ signal produced by 97 eV electrons, and assuming that production of this ion from C_3F_8 is temperature insensitive at this energy.

(ii) Vinyl Chloride, $\text{C}_2\text{H}_2\text{Cl}$, Measurements

Measurements on vinyl chloride were performed only in the high-temperature tube. As reported previously by others,^{13,14} the only ion formed in significant amounts is Cl^- . The strength of the mass-resolved peak Cl^- signal was measured under "room temperature" conditions as a function of the gas pressure in the line supplying the collision chamber. Comparison of these measurements with similar measurements of the O^- signal produced from N_2O gave a value of $3.2 \times 10^{-17} \text{ cm}^2$. The position of the peak at 1.35 eV was determined relative to the steepest point of the electron-retarding curve. This energy calibration procedure could not be routinely relied on but was found to be satisfactory provided the collision chamber was cleaned by prior heating. The resulting cross-section curve is shown as a linear plot in Fig. 8. The peak has a FWHM of 0.60 eV.

The results of measurements performed at room temperature and at various elevated temperatures are summarized in the semilog plot in

Fig. 9. These curves were placed on a magnitude scale by setting the 290°K peak equal to the value of $3.2 \times 10^{-17} \text{ cm}^2$ determined above. The relative magnitudes of the curves taken at different temperatures were determined by also measuring at each temperature the strength of the parent positive-ion signal, produced by 38 eV electrons, and assuming that this ion production process is temperature insensitive. At temperatures above 850°K we found the reference $\text{C}_2\text{H}_3\text{Cl}^+$ signal decreased significantly, and tentatively ascribed this to thermal dissociation of the vinyl chloride. An instrumental effect, such as a temperature dependent bypass leak from the collision chamber, was ruled out by repeating the measurements with a fixed ratio mixture of $\text{C}_2\text{H}_3\text{Cl}$ and Ne flowing through the collision chamber, and monitoring both the $\text{C}_2\text{H}_3\text{Cl}^+$ and the Ne^+ signals as the temperature was raised. The anomalous drop in the $\text{C}_2\text{H}_3\text{Cl}^+$ signal was not present in the Ne^+ signal. Thus, we conclude that the highest temperature data, shown in Fig. 9 as a broken curve, is taken in the presence of thermal dissociation of the $\text{C}_2\text{H}_3\text{Cl}$. The direction of the additional uncertainty attached to this curve is not obvious, since we have no independent knowledge of the Cl^- production processes from the thermal dissociation products. In the event that the products do not produce Cl^- at these energies, the broken curve would represent a lower limit to the $\text{C}_2\text{H}_3\text{Cl}$ cross section at this temperature.

4. DISCUSSION

The determination of ion appearance potentials from ion appearance curves is in essence a deconvolution problem. Normally it is possible to adopt the simple approach of linearly extrapolating the curve measured immediately above threshold. For confidence to be placed in the extrapolated threshold determined in this way it is necessary that the range of the linear fit be at least a few times the energy resolution of the measurement, and that the residual curvature at the "toe" of the curve be consistent with the known energy resolution of the measurements.²⁷ The appearance curve for positive ions from C_3F_8 measured in the present work does not meet these criteria, due to the severe upward curvature, and consequently it is difficult to place reasonable confidence limits on the determined value of 13.0 eV. This number corresponds to most probable electron beam energy at which the signal reached significantly above the background. Given the sensitivity of these measurements, and the possible presence of "hot-bands," it is reasonable to regard this value as a lower limit to the true value with the possible error being at least as large as the energy resolution, in this case 0.1 eV.

The difficulty of making this determination is inherent in the process and is no doubt partly responsible for the wide range of

previously measured values. Lifschitz and Grajower²⁸ used a mass spectrometer to measure a threshold of 13.4 eV for the production of CF_3^+ . These authors list prior values ranging to 14.65 eV, not including Kurepa's value of 14.7 eV, and calculate a value of 13.3 eV to be expected from known heats of formation. The value of 13.38 eV obtained by photo-electron spectroscopy²⁹ appears to be the most reliable. For the purposes of computing ionization rates in a discharge environment, we would therefore recommend use of our determined cross section down to an electron energy of approximately 14 eV, and matching this curve to one going to zero at 13.3 eV.

The present room temperature cross sections for C_3F_8 determined by total ion current measurements may be compared with the results of Kurepa,⁹ who used the same general technique. His positive ionization cross-section data are not reported in sufficient detail to compare them with the present results in the threshold region. There is reasonably good agreement regarding the general shape up to 80 eV, which was the limit of the present measurements. However, Kurepa's cross section is approximately a factor of two larger than the present measurement. Discrepancies of this magnitude between measurements of this type are not normally encountered, and we can offer no explanation in this case.

Comparison with Kurepa's total attachment cross section is best made by plotting the data semilogarithmically, as in Fig. 6. To this end, Fig. 4 of Ref. 9 was replotted and overlayed on the present Fig. 6. The shapes of the two measured cross sections are found to be in excellent agreement over most of the main peak, but compared to the main

peak we find the amplitude of the second peak to be smaller by a factor of 39, while Kurepa's data indicate a factor of 22. More serious is the disagreement regarding the position and magnitude of the main attachment peak. Kurepa's data show this to have a magnitude of $2.3 \times 10^{-16} \text{ cm}^2$ occurring at 3.3 eV, compared with the present values of $1.75 \times 10^{-17} \text{ cm}^2$ and 2.8 eV. We are unable to explain these discrepancies.

In Fig. 6 the present data may be compared directly with the "swarm-unfolded" attachment cross sections derived from measurements^{12,11} of the attachment coefficient in dilute mixtures of C_3F_8 in N_2 or Ar. At the pressures used in both these studies there is a contribution to the measured attachment from the initial transient parent negative-ion species. This contribution is included in the data of Hunter and Christophorou,¹¹ and for this reason their curve is expected to lie above the present data at the lower energies. At higher energies parent ion production is much less likely, and the differences seen above 4 eV may indicate a real discrepancy. Better overall agreement is found with the data of Spyrou and Christophorou.¹² In this case the basic data also included a contribution to the measured attachment rate from the transient parent ion, and they similarly derived an unfolded cross section which included this contribution. In addition, on the basis of their temperature dependence measurements, these authors assigned relative contributions to the two processes and derived cross sections for the dissociative contribution at each of the temperatures studied. It is this cross section which is reproduced in Fig. 6. The agreement between these data and the present result is

already fairly good, and would clearly be improved for energies below 3 eV if a larger fraction of the measured total attachment coefficient was assigned to the dissociative process.

In Fig. 7 the cross section obtained in the present work at 730°K may be compared with the data from Ref. 12 taken at 750°K, where we have again plotted their derived cross section for the dissociative contribution to the measured attachment rate. The agreement in the peak magnitude is very good, considering the difficulties involved in both determinations, and as in the room temperature data the agreement could clearly be improved below 2 eV if a larger fraction of the measured total attachment rate was assigned to the dissociative process. It should perhaps be emphasized that the present type of measurement normally will measure the shape of the cross section with very high confidence levels, as evidenced by comparing results from various laboratories.

The room temperature measurements of Cl^- production from $\text{C}_2\text{H}_3\text{Cl}$ may be compared directly with recent high-resolution electron beam measurements from a number of sources.^{15,13,14,16} These papers also provide comparisons of the dissociative attachment processes in a number of chemically related compounds and discuss the implications regarding the molecular states involved. Including the present work, all these measurements find the same peak energy for Cl^- production from $\text{C}_2\text{H}_3\text{Cl}$ within the combined error bars, and all but one¹⁵ place it between 1.31 and 1.37 eV. Similar agreement exists regarding the peak FWHM (0.60 eV).

The present measurement of the peak cross-section magnitude, $3.2 \times 10^{-17} \text{ cm}^2$, is in excellent agreement with the value of $3.5 \times 10^{-17} \text{ cm}^2$ implicit in the results of Stricklett et al.¹⁶ We note that these authors performed a total ion collection measurement, in contrast with the present measurement performed with a mass filter. In general the latter type of measurement has significantly greater uncertainties due to the possible presence of mass or ion translational energy discrimination effects. In this case we note that Dressler et al. have shown that the Cl^- fragment is formed with little translational energy, typically 0.1 eV, independent of the electron energy used. Olthoff et al. report a similar result. In these circumstances the discrimination effects associated with a mass filter are greatly reduced, and with care can be eliminated. Greater reliance can then be placed on cross-section measurements performed in this way.

It is clear from Figs. 7 and 9 that in both these gases the dissociative attachment process is significantly dependent on gas temperature, and thus both these gases are of interest regarding possible photo-enhancement of this process by IR absorption. Of the two, $\text{C}_2\text{H}_3\text{Cl}$ has the stronger dependence on temperature and for this reason might be considered the better candidate. However, it must be kept in mind that in the application of present interest, discussed in the Introduction, the attaching species must be reasonably stable in the discharge. In the present work C_3F_8 demonstrated greater stability against thermal dissociation, and similar differences might well be found in the discharge environment. Thus, the present results do not

significantly favor one candidate over the other in choosing an attaching discharge additive. The results of experiments to determine the possibility of enhancing their attachment by irradiation at CO₂ laser wavelengths, as was achieved previously in SF₆⁶, will be reported elsewhere.

5. SUMMARY AND CONCLUSIONS

The measurements reported above provide ionization and attachment cross sections for C_3F_8 which are much smaller than previously reported measurements⁹ which used essentially the same technique. Based on the present measurements of the general shape and magnitude of the ionization cross section, and a more reliable threshold value determined by photo-electron spectroscopy,²⁹ we recommend an ionization cross section up to 80 eV which incorporates the best information available at this time.

There is relatively good agreement between the present measurements of the C_3F_8 attachment cross section at room temperature and at elevated temperatures, and the results obtained from swarm experiments.^{12,11} The present results suggest that, in the interpretation of the swarm measurements, a smaller fraction of the overall attachment rate should be assigned to the parent ion process at the lower electron energies. The C_3F_8 attachment cross section is significantly dependent on gas temperature, but not dramatically so in the way that has been observed with some molecules.²⁴ There were no effects of thermal dissociation of the C_3F_8 apparent in the present study.

The present room temperature measurement of the cross section for Cl^- production from $\text{C}_2\text{H}_3\text{Cl}$ gives a peak at 1.35 eV with a FWHM of 0.6 eV, and a peak value of $3.2 \times 10^{-17} \text{ cm}^2$. These numbers agree well with a number of recent determinations of the shape and position in energy of the peak, and also with a total attachment cross-section measurement¹⁶ which gave a value of $3.5 \times 10^{-17} \text{ cm}^2$.

The effects of increased temperature on the attachment cross section are significantly greater in the case of $\text{C}_2\text{H}_3\text{Cl}$ than with C_3F_8 . At 850°K the peak cross section has increased by a factor of 2.6 and occurs lower in energy by 0.3 eV. The threshold has moved from 0.85 eV to zero energy, where its value becomes $6 \times 10^{-18} \text{ cm}^2$. At higher temperatures the interpretation of the data becomes uncertain due to the presence of effects ascribed to thermal dissociation of the $\text{C}_2\text{H}_3\text{Cl}$.

The presently measured temperature sensitivities of the attachment processes in both these gases, and their known IR absorption spectra, make them interesting candidates for use as attaching additives in optically controlled discharges, but does not clearly identify the better choice. The effect of temperature is significantly greater for $\text{C}_2\text{H}_3\text{Cl}$, but the effects of thermal dissociation observed in the present work indicate the possibility of similar chemical stability problems in the gas discharge environment.

6. ACKNOWLEDGEMENTS

We wish to acknowledge the technical assistance of W. M. Uhlig and L. D. Kurtz in the construction and maintenance of the apparatus, and thank the authors of References 7 and 17 for communicating their results to us prior to their publication. This work was supported in part by the U. S. Army Research Office.

7. REFERENCES

1. K. H. Schoenbach, G. Schaeffer, M. Kristiansen, L. L. Hatfield, and A. H. Guenther, IEEE Trans. Plasma Sci. PS-10, 246 (1982).
2. L.G. Christophorou, S. R. Hunter, J. G. Carter, and R. A. Mathis, Appl. Phys. Lett. 41, 147 (1982).
3. P. Bletzinger, Proc. 4th. Pulse Power Conf. Albuquerque, 1983, p. 37.
4. M. J. Rossi, H. Helm, and D. C. Lorents, Appl. Phys. Lett. 47, 576 (1985). O. Kobayashi, T. Sasagawa, and M. Obara, Appl. Phys. Lett. 51, 2103 (1987).
5. L. G. Christophorou, S. R. Hunter, L. A. Pinnaduwage, J. G. Carter, A. A. Christodoulides, and S. M. Spyrou, Phys. Rev. Lett. 58, 1316 (1987).
6. C. L. Chen and P. J. Chantry, J. Chem. Phys. 71, 3897 (1979).
7. G. Schaefer, M. Giesselmann, B. Pashaie, and M. Kristiansen, "CO₂ Laser Enhanced Electron Attachment in Externally Sustained Diffuse Gas Discharges Containing Vinyl Chloride," submitted to J. Appl. Phys. (1988).
8. Matheson Gas Data Book.
9. M. V. Kurepa, 3rd Cz. Conf. Electr. Vac. Phys. (1965), p. 107.

10. J. T. Tate and P. T. Smith, *Phys. Rev.* 39, 270 (1930). See also Ref. 26.
11. S. R. Hunter and L. G. Christophorou, *J. Chem. Phys.* 80, 6150 (1984).
12. S. M. Spyrou and L. G. Christophorou, *J. Chem. Phys.* 83, 2829 (1985).
13. J. K. Oltoff, J. A. Tossell, and J. H. Moore, *J. Chem. Phys.* 83, 5627 (1985).
14. R. Dressler, M. Allan, and E. Haselbach, *CHIMIA* 39, 385 (1985).
15. R. Kaufel, E. Illenberger, and H. Baumgarter, *Chem. Phys. Lett.* 106, 342 (1984).
16. K. L. Stricklett, S. C. Chu and P. D. Burrow, *Chem. Phys. Lett.* 131, 279 (1986).
17. P. D. Burrow, A. Modelli, N. S. Chiu, and K. D. Jordan, *Chem. Phys. Lett.* 82, 270 (1981).
18. P. D. Burrow, private communication.
19. R. E. Fox, W. M. Hickam, D. J. Grove, and T. Kjeldaaas, *Rev. Sci. Instrum.* 26, 1101 (1955).
20. P. J. Chantry, *Rev. Sci. Instrum.* 40, 884 (1969).
21. P. J. Chantry, *J. Chem. Phys.* 57, 3180 (1972).
22. L. E. Kline, D. K. Davies, C. L. Chen, and P. J. Chantry, *J. Appl. Phys.* 50, 6789 (1979).
23. P. J. Chantry, in *Applied Atomic Collision Physics*, Vol. 3, *Gas Lasers*, E. W. McDaniel and W. L. Nighan, Eds. (Academic Press, 1982).

24. P. J. Chantry, J. Chem. Phys. 51, 3369 (1969).
25. D. Rapp and D. D. Briglia, J. Chem Phys. 43, 1480 (1965).
26. D. Rapp and P. Englander-Golden, J. Chem Phys. 43, 1464 (1965).
27. P. J. Chantry, J. Chem. Phys. 55, 2746 (1971); 65, 4412 (1976).
28. C. Lifshitz and R. Grajower, Int. J. Mass Spec. Ion Phys. 3, 211 (1969).
29. M. J. S. Dewar and S. D. Worley, J. Chem. Phys. 50, 654 (1969).

FIGURE CAPTIONS

Fig. 1. Collision chamber and related electrodes used for the room temperature measurements of the cross-section magnitudes. The electron beam (EB) is produced by an electron gun (not shown). The Repeller (Rep) and Attractor (Attr) electrodes form a parallel plate geometry for the total ion current measurements.

Fig. 2. An example of the total negative ion currents measured as a function of the collision chamber pressure in N_2O and C_3F_8 . In each case the electron beam energy is adjusted to the peak in the cross section. The ratio of the slopes gives the ratio of the peak cross sections.

Fig. 3. Composite figure showing the electron energy dependence of the negative-ion signal from C_3F_8 , the positive-ion signal from Xe, and the RPD electron beam current. The relative positions of the three curves are given directly by the measurements. The position of the scale zero is adjusted to coincide with the steepest part of the retarding curve.

Fig. 4. The total ionization cross section of C_3F_8 measured relative to the known cross section of Xe. In (a) the full curve shows the shape of

the cross section measured at a fixed pressure, normalized to the points at 40, 60, and 80 eV determined by measurements over a range of pressure of the type shown in Fig. 2. In (b) we show details of the threshold region.

Fig. 5. The total attachment cross section of C_3F_8 measured at 330°K relative to the known cross section of N_2O .

Fig. 6. Comparison of the present measurement of the room temperature attachment cross section in C_3F_8 with data of Spyrou and Christophorou (SC, Ref. 12), and of Hunter and Christophorou (HC, Ref. 11).

Fig. 7. The cross section for F^- production from C_3F_8 measured at the temperatures indicated, using the "High-Temperature Collision Chamber." The data of Spyrou and Christophorou (SC, ref. 12) is shown for comparison.

Fig. 8. The cross section for Cl^- production from C_2H_3Cl at room temperature (330°K).

Fig. 9. The cross section for Cl^- production from C_2H_3Cl measured at the temperatures indicated, using the "High-Temperature Collision Chamber." The highest temperature curve (970°K) is uncertain due to thermal dissociation effects.

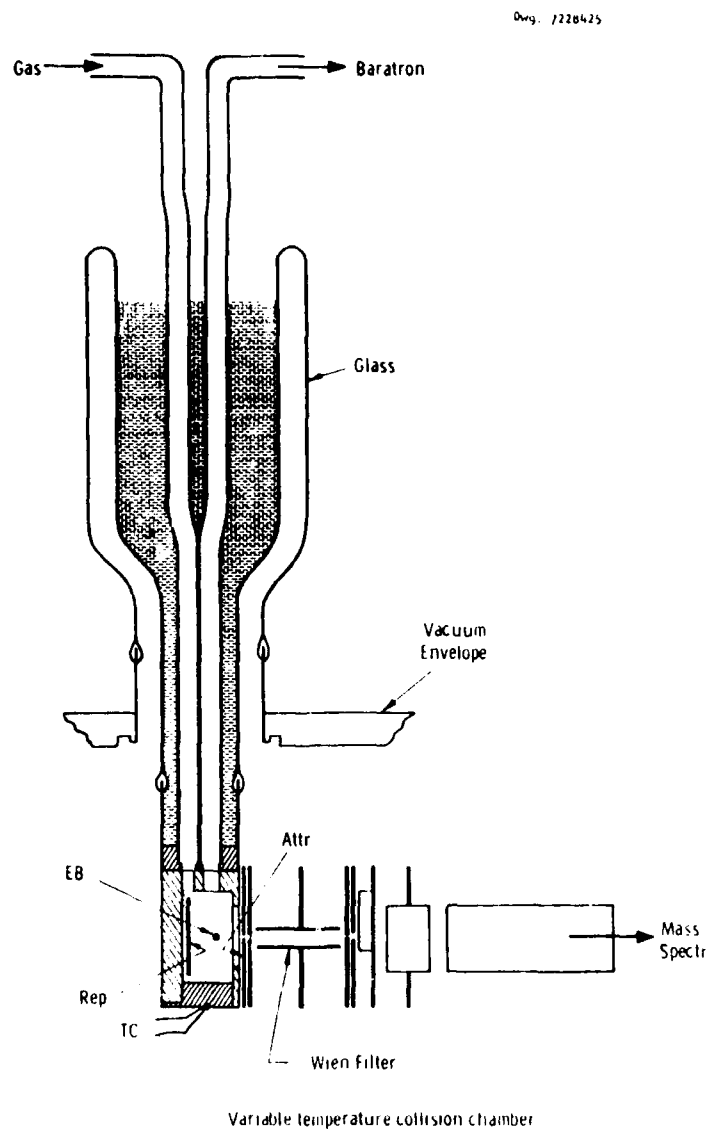


Figure 1 — Collision chamber and related electrodes used for the room temperature measurements of the cross-section magnitudes. The electron beam (EB) is produced by an electron gun (not shown). The Repeller (Rep) and Attractor (Attr) electrodes form a parallel plate geometry for the total ion current measurements.

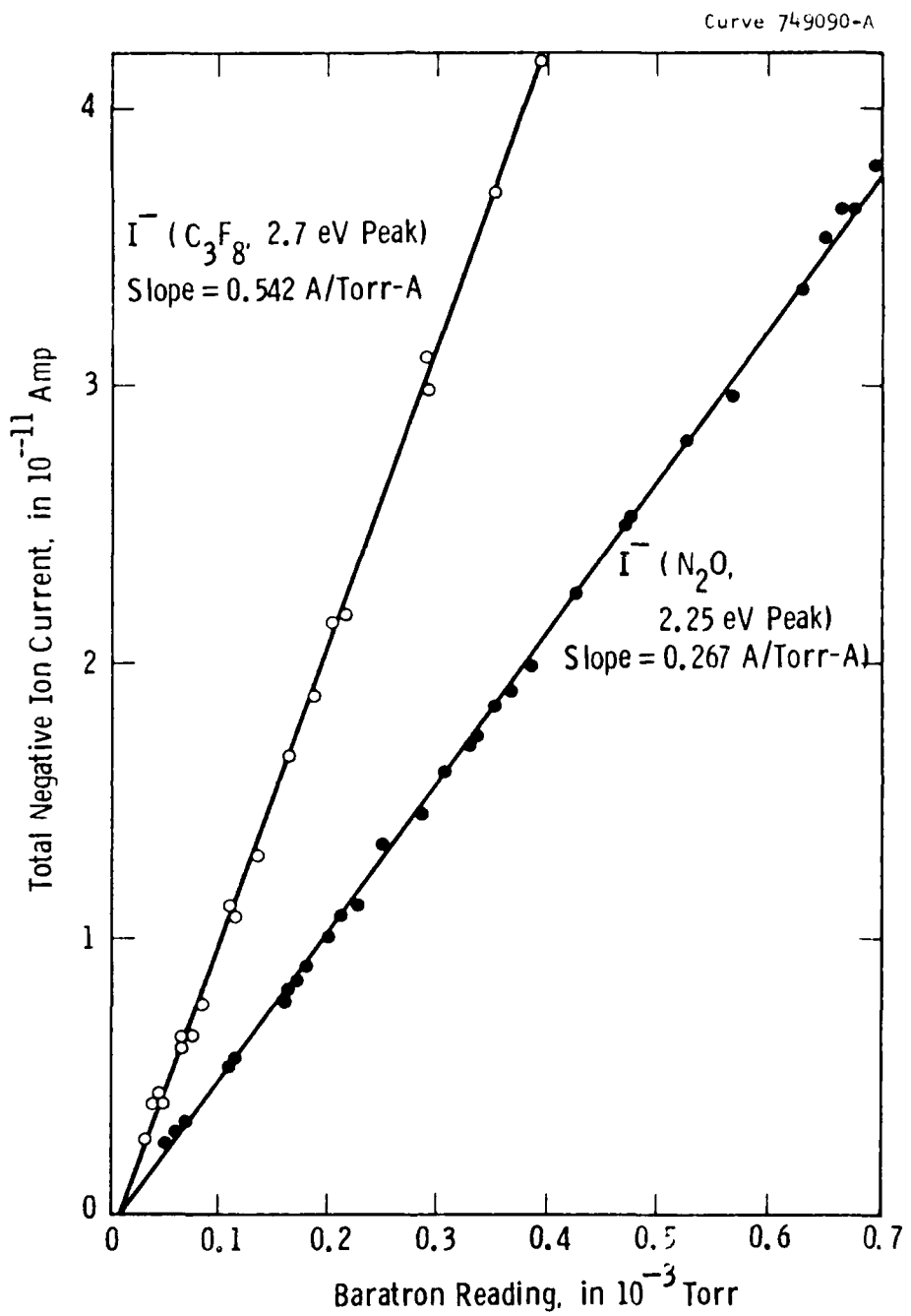


Figure 2 — An example of the total negative ion currents measured as a function of the collision chamber pressure in N_2O and C_3F_8 . In each case the electron beam energy is adjusted to the peak in the cross section. The ratio of the slopes gives the ratio of the peak cross sections.

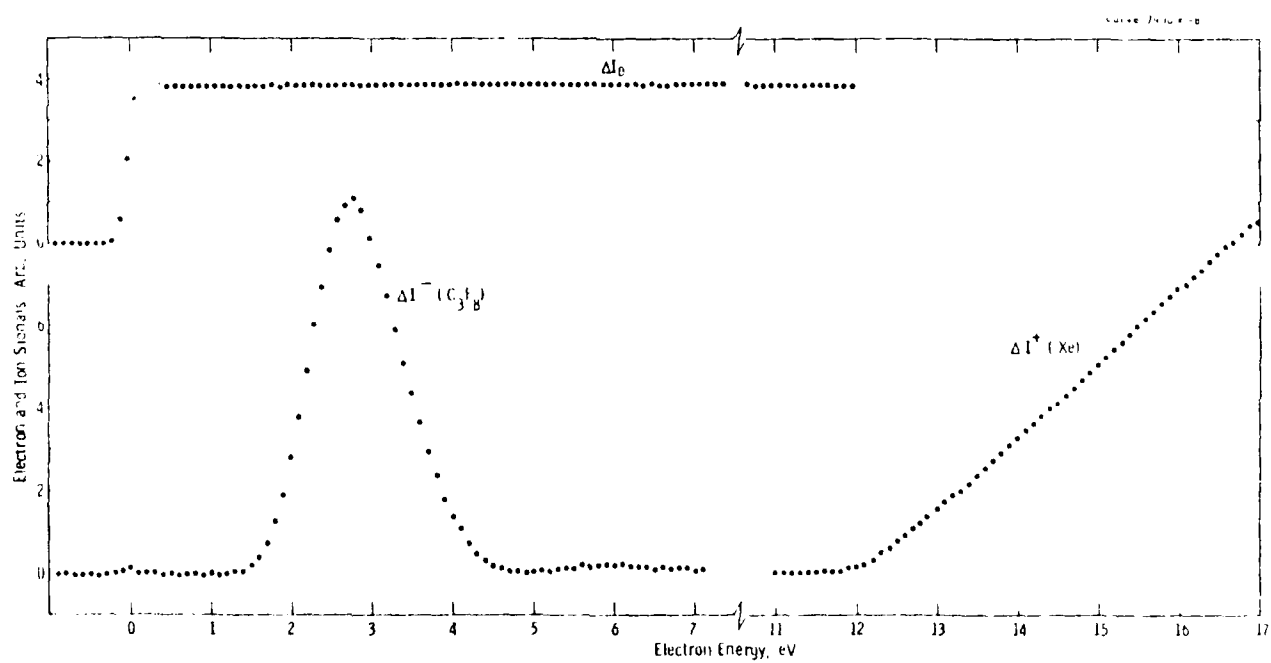


Figure 3 — Composite figure showing the electron energy dependence of the negative-ion signal from C_3F_8 , the positive-ion signal from Xe, and the RPD electron beam current. The relative positions of the three curves are given directly by the measurements. The position of the scale zero is adjusted to coincide with the steepest part of the retarding curve.

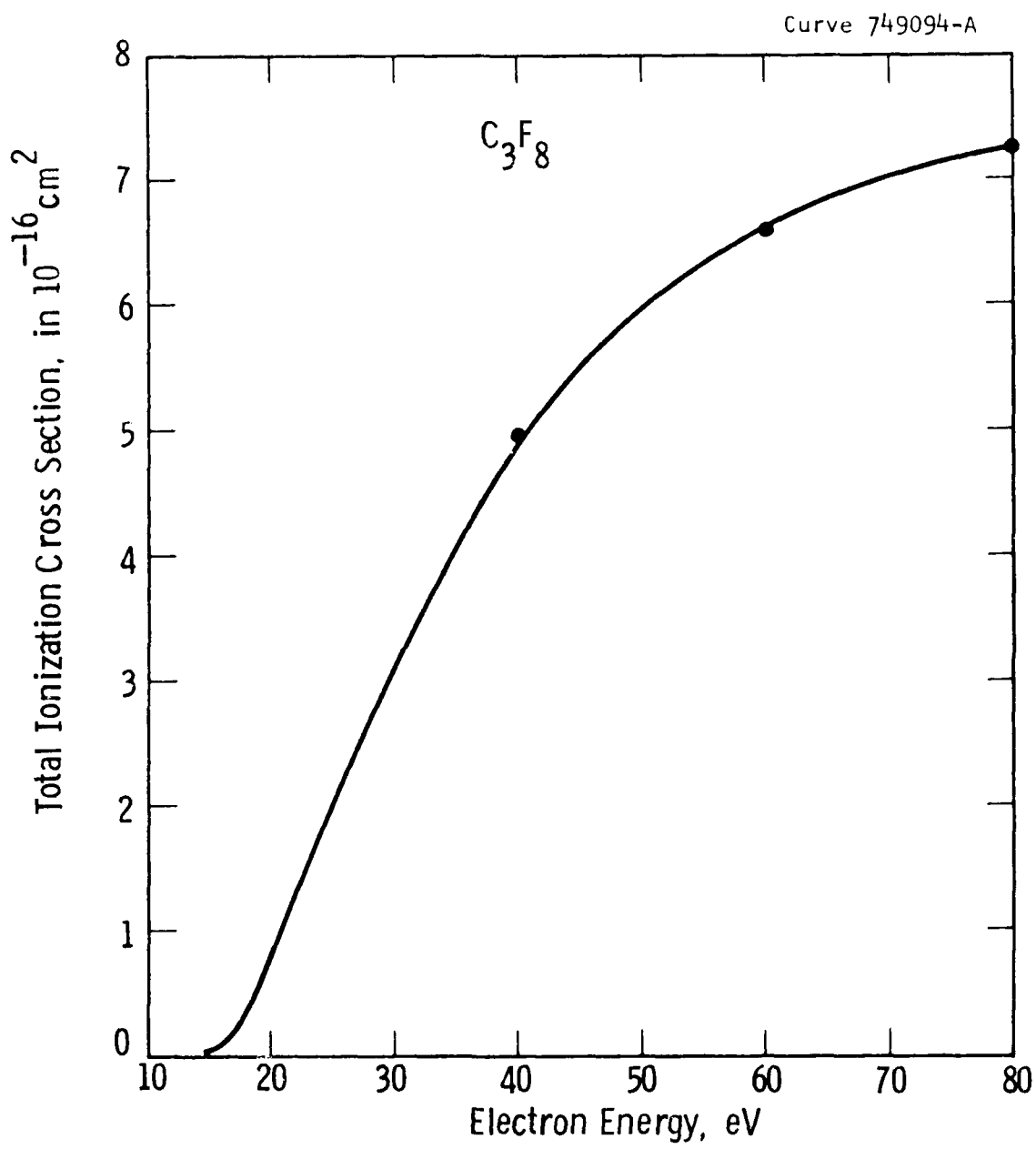


Figure 4(a) — The total ionization cross section of C_3F_8 measured relative to the known cross section of Xe. In (a) the full curve shows the shape of the cross section measured at a fixed pressure, normalized to the points at 40, 60, and 80 eV determined by measurements over a range of pressure of the type shown in Fig. 2.

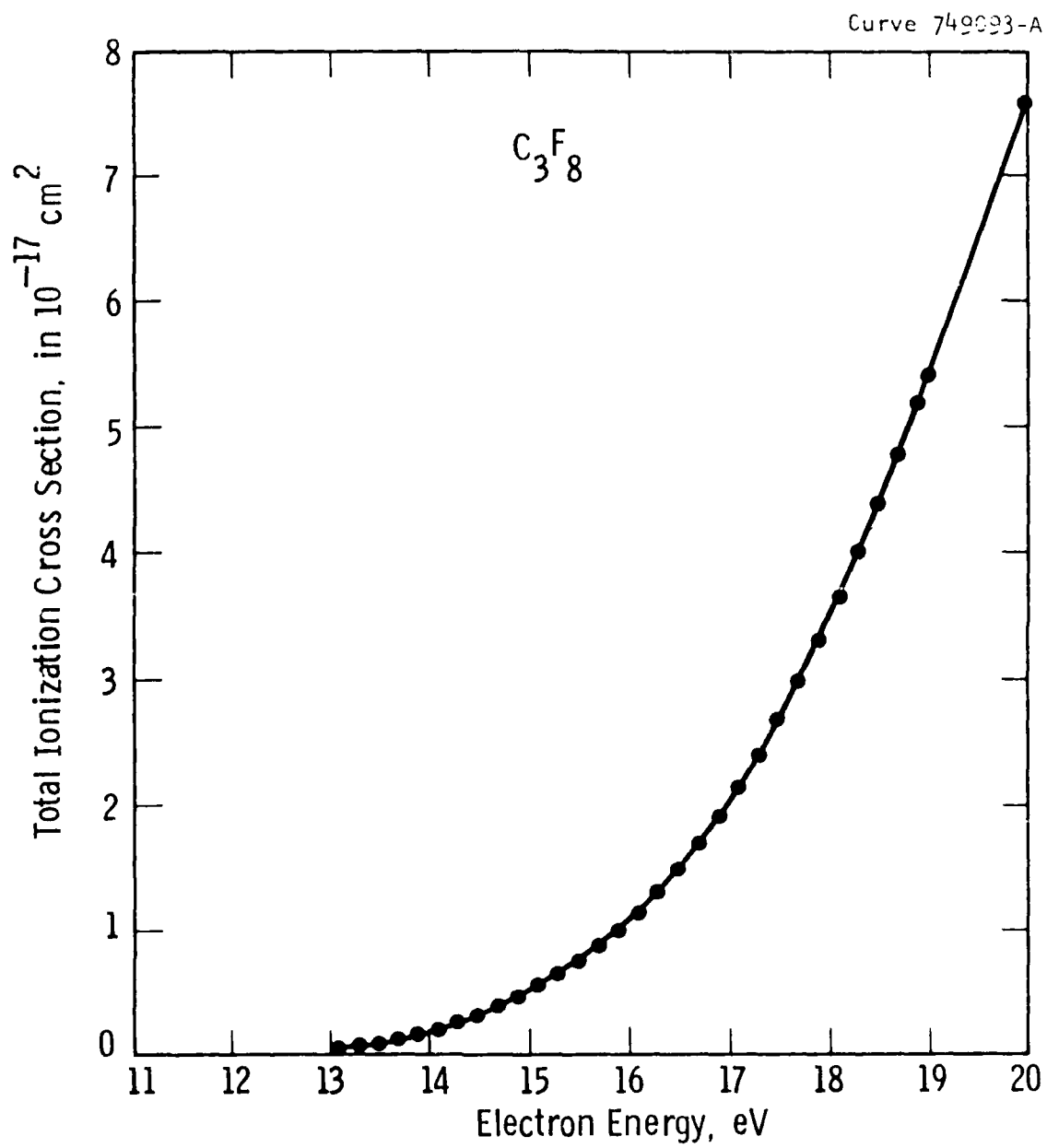


Figure 4(b) — The total ionization cross section of C_3F_8 measured relative to the known cross section of Xe. In (b) we show details of the threshold region.

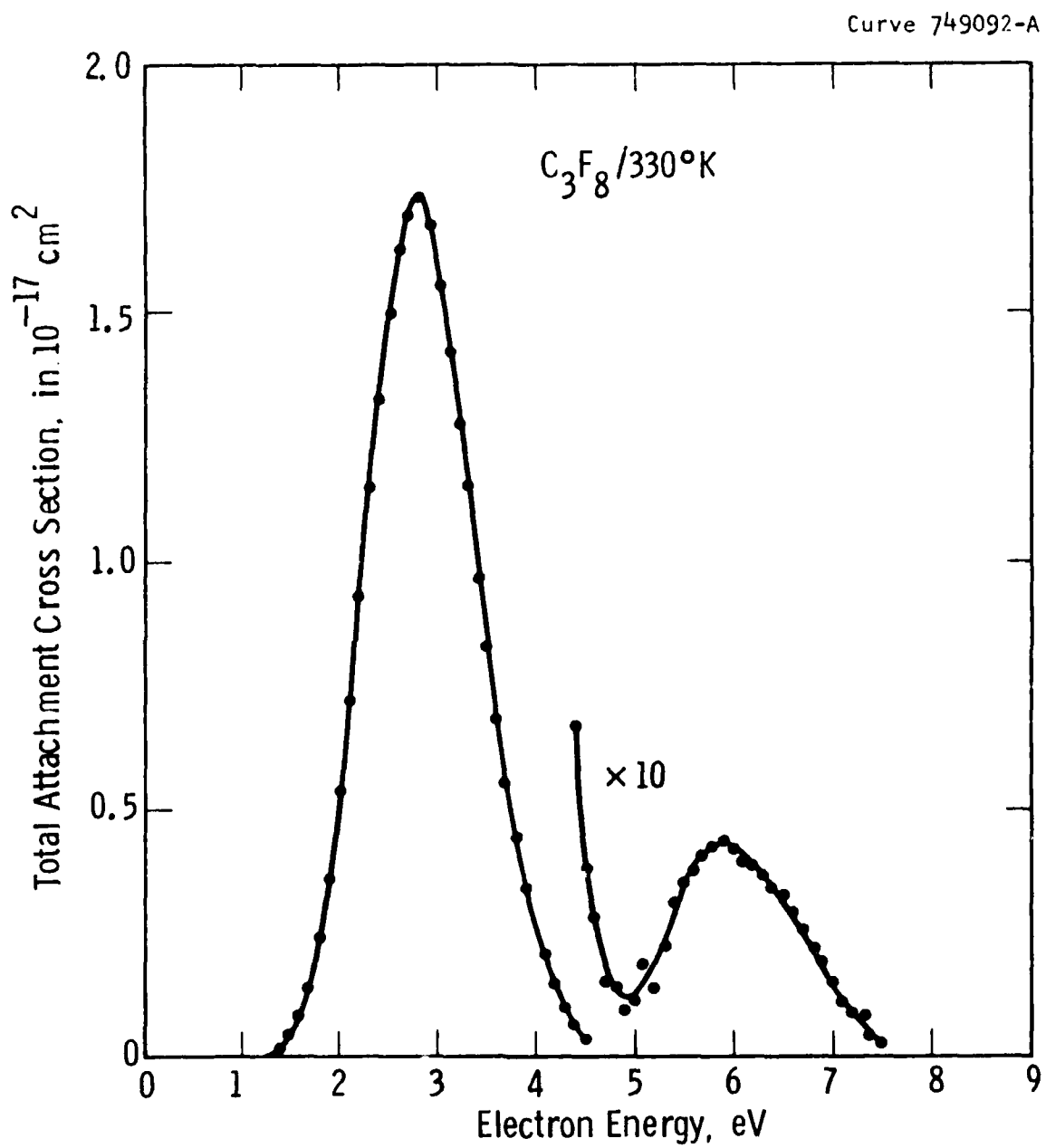


Figure 5 — The total attachment cross section of C_3F_8
measured at $330^\circ K$ relative to the known
cross section of N_2O .

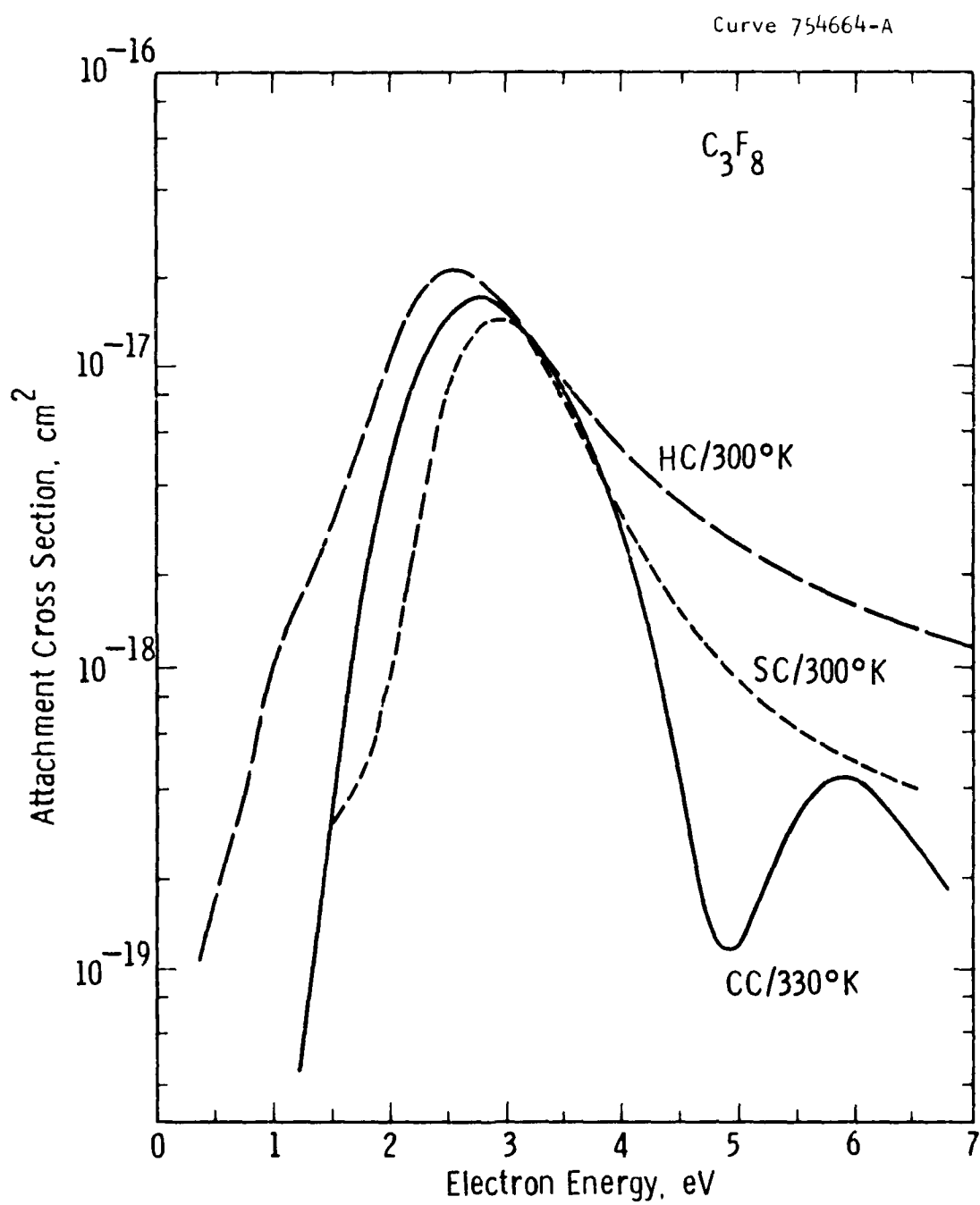


Figure 6 — Comparison of the present measurement of the room temperature attachment cross section in C_3F_8 with data of Spyrou and Christophorou (SC, Ref. 12), and of Hunter and Christophorou (HC, Ref. 11).

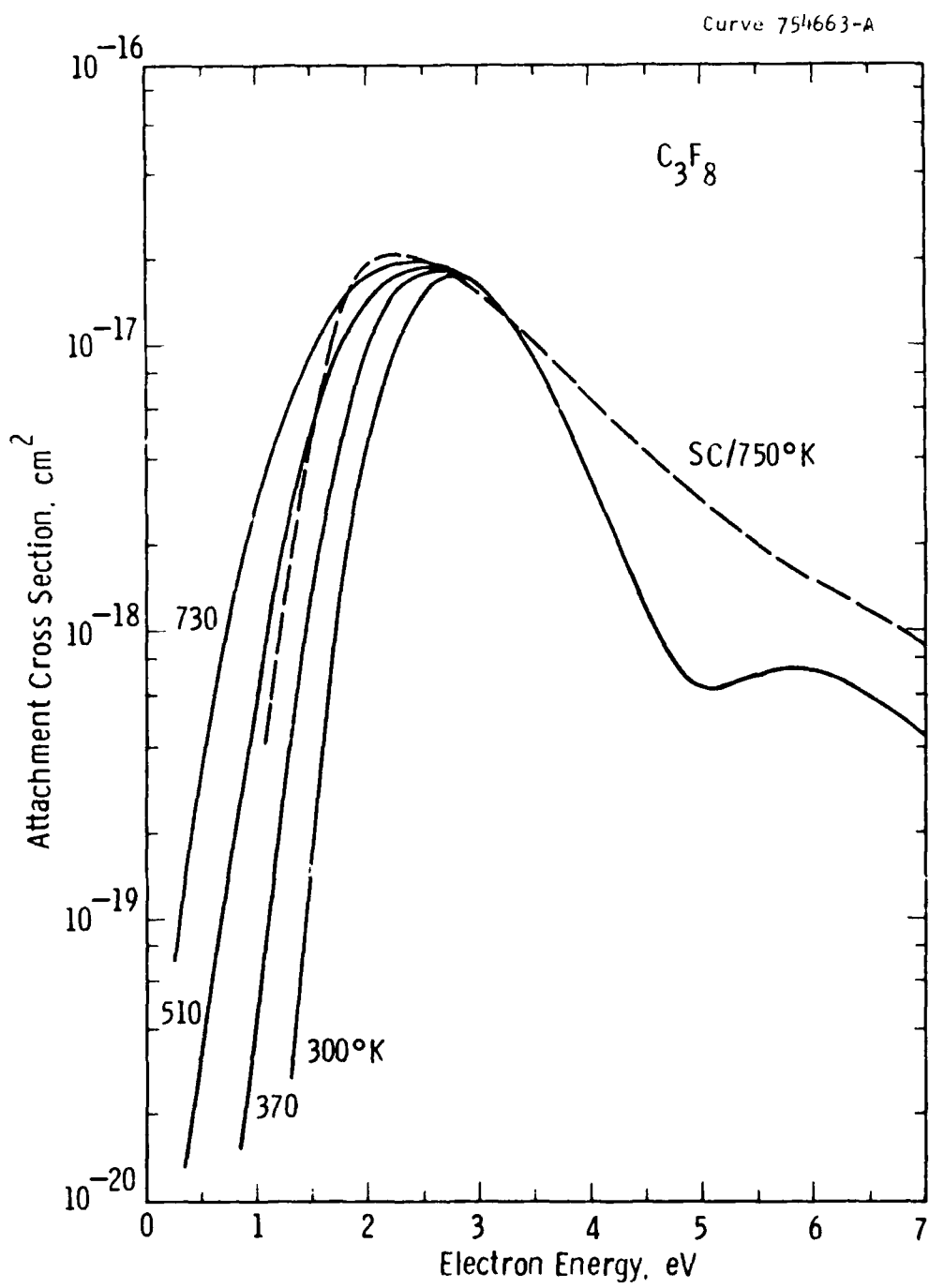


Figure 7 — The cross section for F^- production from C_3F_8 measured at the temperatures indicated, using the "High-Temperature Collision Chamber." The data of Spyrou and Christophorou (SC, Ref. 12) is shown for comparison.

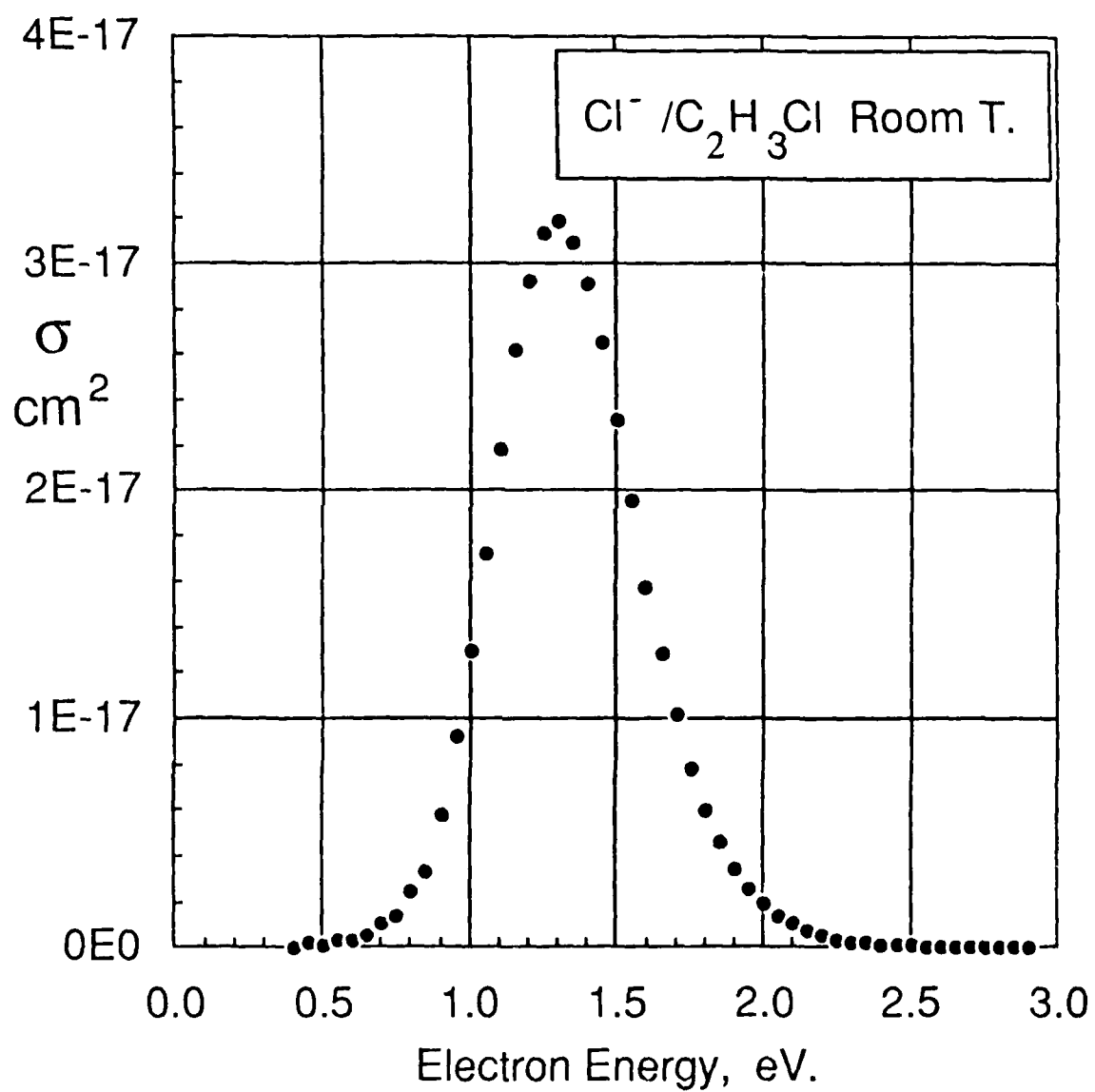


Figure 8 — The cross section for Cl⁻ production from C₂H₃Cl at room temperature (330°K).

Curve 754665-A

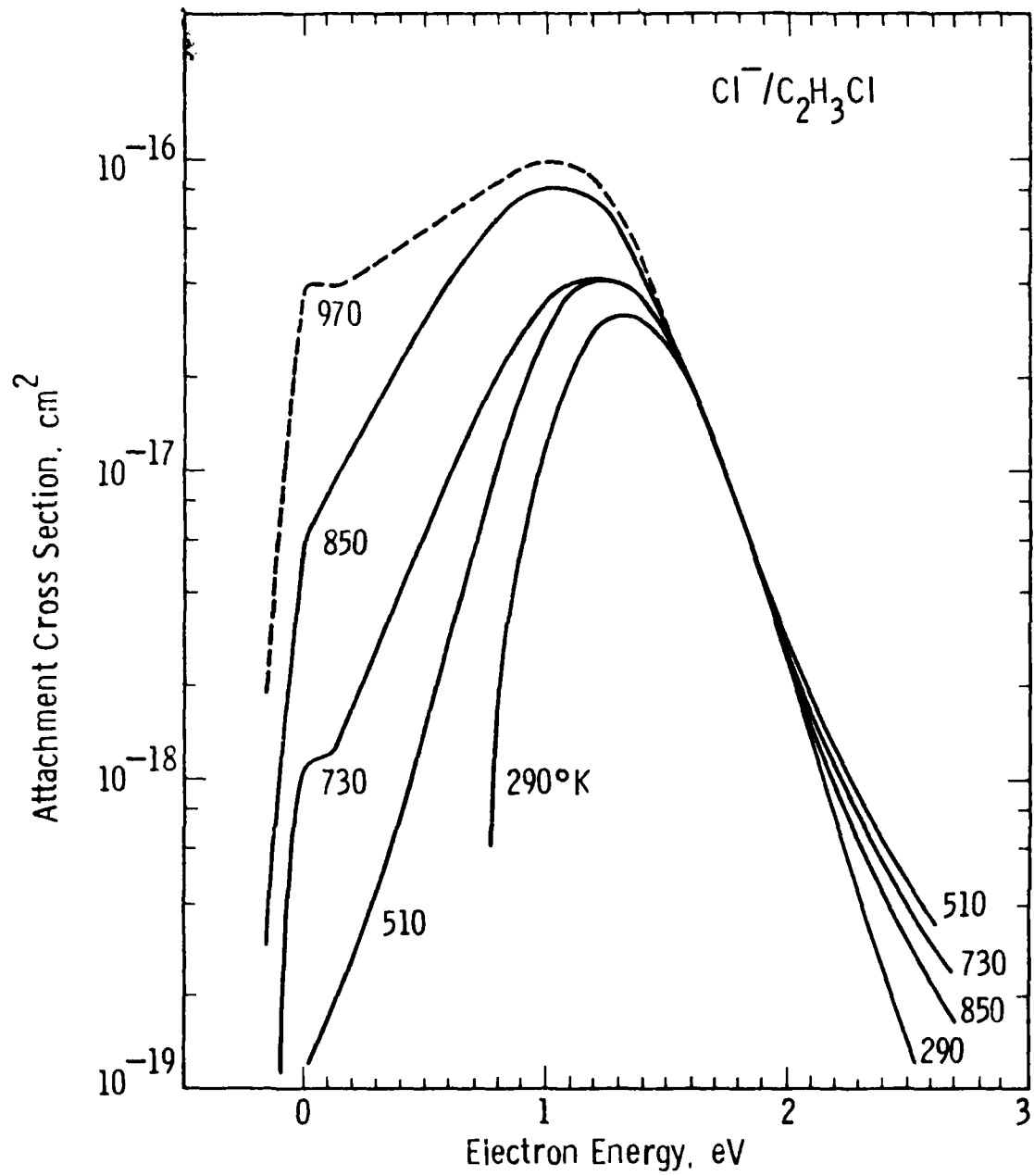


Figure 9 — The cross section for Cl⁻ production from C₂H₃Cl measured at the temperature indicated, using the "High-Temperature Collision Chamber." The highest temperature curve (970°K) is uncertain due to thermal dissociation effects.

APPENDIX 10.2

MEASUREMENTS OF SWARM PARAMETERS AND DERIVED ELECTRON COLLISION CROSS SECTIONS IN METHANE

D. K. Davies, L. E. Kline, and W. E. Bies

Westinghouse R&D Center, Pittsburgh, Pennsylvania 15235

ABSTRACT

A pulsed drift tube has been used to measure the electron drift velocity in methane over the range of E/N from 10 to 1000 Td. In addition, measurements of the positive ion mobility and ionization coefficient have been made over the range of E/N from 80 to 1000 Td. Within the experimental sensitivity, no evidence of attachment has been observed in this range. A set of electron collision cross sections has been assembled and used in Monte Carlo simulations to predict values of swarm parameters. The cross section set includes a momentum transfer cross section which is based primarily on the present and previous drift velocity measurements, cross sections for vibrational excitation and ionization based on published experimental cross section measurements, and a cross section for dissociation into neutral products obtained by subtracting a measured dissociative ionization cross section from a measured total dissociation cross section. Isotropic scattering is assumed for all types of collisions in the Monte Carlo simulations. Good agreement between the predicted and measured values of swarm parameters is obtained without making any adjustments to these cross sections. A two-term Boltzmann equation method has also been used to predict swarm parameters using the same cross sections as input. The two-term results are in poor agreement with experiment and confirm the well-known inadequacy of two-term methods in the case of methane.

PACS numbers: 34.80, 52.20

I. INTRODUCTION

Recently, there has been renewed interest in methane for application in diffuse discharge electrical switching¹ and in the thin-film, plasma-enhanced, chemical vapor deposition of hard carbon² and diamond.³ In order to model the behavior of such systems, a knowledge of the electron collision cross sections is necessary. To provide some of this data base, measurements of electron and positive-ion mobilities together with ionization coefficients have been carried out over the range of E/N from 10 to 1000 Td using a pulsed drift tube. This range of E/N values is relevant to the opening mode of diffuse discharge switches and covers the lower end of the E/N range observed in deposition systems.

Methane has been used as a test gas by several authors⁴⁻⁶ in developing methods for calculating electron energy distributions. Methane is a good test gas because the cross sections for vibrational excitation are comparable in magnitude to the elastic cross section in the energy range near the Ramsauer minimum. This feature of the methane cross sections is inconsistent with the use of a two-term spherical harmonic expansion to represent the distribution function. Model cross sections for methane have been used in Refs. 4-6 as a test case for multi-term solutions of the Boltzmann equation and for Monte Carlo calculations in the low E/N region (< 10 Td) where the electron behavior is dominated by the features just described. Recently, Haddad⁷, in a study similar to the one described here, has used a more complete and accurate cross section set to study the low E/N region. In Haddad's study, a multi-term method is used to solve the Boltzmann equation and predict swarm parameter values which are in good agreement with the measured values. Haddad has also shown that the use of the two-term approximation in solving the Boltzmann equation leads to large errors in predicted transport coefficient values for methane.

At high values of E/N, the first theoretical analysis of electron transport in methane is that reported by Kline⁸ using a two-term expansion solution of the Boltzmann equation. The assumptions underlying the two-term spherical harmonic expansion solution of the Boltzmann equation are also violated at high E/N because

the cross section for elastic scattering becomes a small fraction of the total cross section at high electron energies. Thus, Monte Carlo or multi-term techniques provide more accurate results for methane at high E/N. Al-Amin et al.⁹ and Ohmori et al.¹⁰ have used Monte Carlo techniques to study methane at high E/N. However, the earlier study of Al-Amin et al. was hampered by a lack of experimental cross section data. The most complete set of cross sections used so far is the cross section set of Ohmori et al. They have obtained good agreement between predicted and available experimental swarm data.

The theoretical calculations reported here are motivated by (i) the availability of our new swarm data, taken in the same apparatus over a wide range of E/N values, (ii) uncertainty about the ionization and attachment behavior in methane near the ionization threshold, and (iii) the availability of additional experimental cross section data. The calculations described here use a cross section set similar to that used by Ohmori et al¹⁰. The cross section set includes a momentum transfer cross section which is based primarily on the present and previous drift velocity measurements, cross sections for vibrational excitation and ionization based on published experimental cross section measurements, and a cross section for dissociation into neutral products (i.e., neutral dissociation) obtained by subtracting a measured dissociative ionization cross section from a measured total dissociation cross section. The neutral dissociation cross section is further divided into four components with thresholds at 9, 10, 11, and 12 eV, in order to give a better representation of the continuous electron energy loss spectrum in methane. Separate cross sections are used for CH_4^+ production and dissociative ionization. This more detailed representation of the neutral dissociation and ionization processes, compared with previous work, has been included for two reasons. First, these processes are the key processes in deposition discharges. Second, the shape of the cross sections for these processes near their thresholds affects the threshold behavior of the ionization coefficient.

Isotropic scattering has been assumed for all of the scattering processes in the Monte Carlo calculations. This assumption has been made in all of the previous Monte

Carlo calculations for methane except for those of Al-Amin et al.⁹ The published experimental differential cross section data for methane, which are briefly described in Section IV, show that forward scattering predominates in methane. The assumption of isotropic scattering has been made in this work to simplify the Monte Carlo calculations and to limit the amount of data required to describe the collision cross sections. We have made additional calculations for methane which include a full treatment of anisotropic scattering. The results of these calculations will be described in a separate paper.

The present cross section set has been tested by comparing predicted electron swarm parameters (i.e., drift velocity and ionization coefficient) with measured values. The transport coefficient values have been predicted both from Monte Carlo simulations and from two-term expansion solutions of the Boltzmann transport equation. The swarm parameter values predicted by the Monte Carlo simulations are in good agreement with the measured values. This good agreement confirms the self-consistency and validity of the cross section set. The swarm parameter values predicted by the two-term expansion solutions of the Boltzmann transport equation are in poor agreement with the measured values, as expected for methane.

The remainder of this paper is organized as follows. The next section describes the experimental apparatus and procedures and the third section describes the experimental results. The fourth section briefly describes the theoretical methods and discusses the cross section data which have been derived. The fifth section presents the theoretical results and compares the measured and predicted swarm data. The last section summarizes the results presented here.

II. EXPERIMENT

A. Apparatus

The drift tube together with the associated vacuum and gas-handling systems and complete experimental arrangement used for these measurements have been described in detail previously.¹¹ Thus, only the salient features of the facility will be given here for continuity in discussing the present results. A schematic diagram of the drift-tube arrangement is shown in Figure 1.

A uniform-field drift region is maintained between cathode and anode by a set of ten annular guard rings whose centers are spaced 0.5 cm apart. A chain of precision resistors across a bipolar dc power supply is used to derive the potentials applied to the drift tube, and the potential difference between cathode and anode is measured to better than $\pm 0.1\%$ using a digital voltmeter. Both anode and cathode are electrically shielded from the drift region by a highly transparent grid (87% optical transparency) located 0.1 cm from each electrode. The cathode contains a sapphire insert centered along the axis of the drift tube whose face adjacent to the drift region is coated with a thin gold film. The anode and its associated screen structure are coupled to the chamber envelope via a linear bellows drive enabling the drift distance to be varied. The tube is designed so that either cathode or anode may be connected to high potential, enabling current transients to be measured at either one.

The drift tube forms part of a bakeable ultra-high vacuum and gas-handling system which has a base residual pressure of 10^{-9} Torr. Research grade (Grade 4.2) methane, supplied by Airco, has been used for the measurements. The gas has a minimum specified purity of 99.992%, the major impurity constituents (in ppm) being nitrogen : 20, hydrogen : 10, carbon monoxide and carbon dioxide : 10, ethane : 10, and oxygen : 4. The gas pressure in the drift tube is measured using two Baratron gauges having a combined specified accuracy of $\pm 0.1\%$ over the range from 0.1 to 1000 Torr.

Back illumination of the semi-transparent cathode by a pulse of uv radiation from an externally mounted source releases a pulse of electrons into the drift region. The resulting time-resolved current collected at either the anode (using the arrangement

shown in Figure 1) or the cathode (connecting the measurement circuitry to the cathode and the anode to high potential) is amplified and fed to a waveform digitizer (Biomation Model 6500) and signal averager (Nicolet Model 1070) and stored on 9-track tape (Kennedy Model 9700). Data are accumulated in the signal averager at a repetition rate $\sim 30 - 100 \text{ s}^{-1}$ until the signal/noise ratio has attained a satisfactory value; typically, this requires the summation of between 10^4 and 10^5 digitized current waveforms.

Two different pulsed uv sources have been used in the present study. For the measurements of electron drift velocity, a spark source operating in air (Xenon Corp. Model 437A/N-789B) is used. The uv output from this source has a risetime of 10 ns and a halfwidth of 20 ns and liberates $\sim 10^5$ photoelectrons/pulse from the cathode. For the measurements of ion mobility, attachment, and ionization, a pulsed xenon lamp is used which produces a uv pulse having a risetime of 65 ns, a halfwidth of 145 ns, giving a cathode photoemission $\sim 10^6$ electrons/pulse. A photomultiplier which views a fraction of the output from the uv source is used to derive a trigger signal for the waveform digitizer. The residual systematic noise, which is coupled (despite careful shielding) into the measuring circuitry from the pulsed light source, is significantly reduced by arranging the transfer of data from the digitizer to the signal averager so that alternate pulses are added to and subtracted from the data already stored in the averager. A synchronized shutter between the pulsed light source and the drift tube is arranged so that during the add cycle the light pulse is allowed into the drift tube while during the subtract cycle it is blocked.

The currents measured at the electrically-shielded cathode and anode collectors are associated with the motion of charge carriers between each collector and its adjacent screen. Thus, in the general case where a mixture of electrons, negative ions, and positive ions are present in the drift region as a result of electron-molecule collisions, all three components of the total current can be resolved directly. At the anode, the attenuated or amplified (depending on E/N) electron signal together with the negative-ion signal are recorded while at the cathode the initial electron signal (produced as a result of the pulsed uv irradiation) and subsequent positive-ion signal

are recorded. Analysis of the recorded waveforms is simplified by making differential measurements at constant increments of drift distance. By making the incremental position of the collector screen coplanar with the center of a guard ring, distortions of the electric field are minimized. Thus, the drift distance is varied in increments of 0.5 cm from 0.7 cm to 5.2 cm.

B. Determination of swarm parameters

1. Anode electron current waveforms

The electron drift velocity is determined from the arrival time τ_e of the peak of the electron component of the total anode current as a function of drift distance d . From the solution of the continuity equation for electrons, the time τ_e is given to first order by^{12,13}

$$\tau_e \equiv (d/w_e) [1 - D_L/w_e d + 2D_L(\alpha - \eta)/w_e], \quad (1)$$

where D_L , α , η are the longitudinal diffusion, ionization, and attachment coefficients, respectively. By making measurements of τ_e as a function of d , errors due to the finite width of the cathode electron pulse, end effects, and (to first order) diffusion effects are eliminated. However, effects due to attachment and ionization are not removed so that the reciprocal of the slope of the linear plot of τ_e versus d is given by

$$w_e' = w_e/[1 + 2D_L(\alpha - \eta)/w_e]. \quad (2)$$

The values of electron drift velocity which we present in Section III correspond to the uncorrected w_e' values.

2. Ion current waveforms

The negative-ion drift velocity w_- is given directly by the reciprocal of the slope of the arrival time of the peak of the negative-ion component of the total anode current as a function of drift distance. Similarly, the positive-ion drift velocity w_+ is given directly by the reciprocal of the slope of the arrival time of the peak of the positive-ion

component of the total cathode current as a function of drift distance. The ion reduced mobilities μ_- and μ_+ are then determined from the corresponding drift velocities by

$$\mu_{\pm} = w_{\pm}/(E/N)N_0, \quad (3)$$

where N_0 ($=2.688 \times 10^{19} \text{ cm}^{-3}$) is the gas number density corresponding to 760 Torr at 273 K.

3. Charge waveforms

For complex molecules, the ion current spectra usually contain more than one ion species. Under these conditions, the attachment and net ionization coefficients are more conveniently determined from the charge (or time-integrated current) waveforms. In the analysis of the charge waveforms it is necessary to take into account the different transparencies of the grids to electrons and ions. Then, writing $y(A)_d$ and $y(A)_{d+\Delta d}$ for the ratio of the total charge to the electron charge collected by the anode at the drift distances d and $d+\Delta d$, respectively, it may be shown¹¹ that

$$y(A)_{d+\Delta d} = y(A)_d \exp -(\alpha - \eta)\Delta d + \{1 + (f_2/f_1)[\eta/(\alpha - \eta)]\} [1 - \exp -(\alpha - \eta)\Delta d], \quad (4)$$

where f_1 and f_2 are the fractions of electrons and ions, respectively, transmitted by each grid. Similarly, the ratio $y(C)_{d+\Delta d}$ of the total charge to the electron charge collected at the cathode at a drift distance $d+\Delta d$ may be expressed as

$$y(C)_{d+\Delta d} = y(C)_d \exp (\alpha - \eta)\Delta d + [1 - f_1 f_2 \alpha/(\alpha - \eta)] [1 - \exp (\alpha - \eta)\Delta d]. \quad (5)$$

In either case, the net ionization coefficient $(\alpha - \eta)$ is given from the slope of a linear plot of $y_{d+\Delta d}$ versus y_d . For perfectly transmitting grids, i. e., for $f_1 = f_2 = 1$, Equations (4) and (5) reduce to the well-known form describing spatial current growth between planar electrodes under steady-state conditions. Such a method of analysis has been shown¹⁴ to give unambiguous values of the net ionization coefficient even when electron detachment is occurring. In practice, it is more convenient to use the anode waveforms [Equation (4)] at values of E/N below the limiting value (i.e., the value at which $\alpha = \eta$) and the cathode waveforms [Equation (5)] above this limiting value. The

ratio α/η is given directly by the ratio of the positive ion charge collected at the cathode to the negative ion charge collected at the anode normalized to the same initial electron charge leaving the cathode.¹¹ Thus, knowing both $(\alpha - \eta)$ and α/η , both of the individual coefficients α and η are determined.

III. EXPERIMENTAL RESULTS

A. Electron drift velocity

The electron drift velocity is determined from the slope of a plot of the arrival time of the peak of the electron component of the anode current as a function of drift distance at each fixed value of E/N. For every plot analysed, the experimental points differ from a linear regression fit by less than 1%. We present our data uncorrected for ionization and attachment effects and identify our values with the quantity w' given by Equation (2). However, for values of $E/N < 300$ Td the correction is less than the experimental uncertainty and we identify the values with the true drift velocity. A summary of the values of w' are shown in Table I and also in Figure 2 where they are compared with previously published data.^{7,9,15-19} The estimated uncertainties in our measured values are $\pm 1\%$ for $E/N \leq 300$ Td and $\pm 2\%$ for $E/N > 300$ Td. In regions of overlap, the present data are in closest agreement (to within the combined uncertainties) with those of Haddad⁷ and of Pollock¹⁸. Also shown in Figure 2 are the predicted values (solid line) from Monte Carlo simulations using the set of electron collision cross sections discussed in Section IV.

B. Ion mobility

The positive-ion drift velocity is determined from the slope of a plot of the arrival time of the peak of the positive-ion component of the cathode current as a function of drift distance at each fixed value of E/N. For every plot analysed, the experimental points differ from a linear regression fit by less than $\pm 0.5\%$. The present data, which have been converted to mobility values according to Equation (3), have an estimated uncertainty of $\pm 1\%$, and are given in Table I and Figure 3 where they are compared with previous measurements.^{17,20}

The positive-ion waveforms do not exhibit a simple exponential time dependence indicating the presence of more than one ion specie or the occurrence of ion conversion reactions. It is known²¹ that the ions CH_4^+ , CH_3^+ , CH_2^+ , CH^+ , C^+ , H^+ , and H_2^+ are all formed by single electron impact on methane, although the first two comprise more than 85% of the total ionization for electron energies up to 100 eV.

Further, these primary ions can undergo ion-molecule reactions with methane at thermal reaction rates²² in excess of 10^{-9} cm³/s; in the case of the ions CH_4^+ and CH_3^+ , the product ions are CH_5^+ and C_2H_5^+ , respectively. Under our experimental conditions, the majority of the primary ions are expected to be converted to product ions before reaching the cathode. The present ion mobility values refer to the slowest ion (the only clearly resolvable ion), and probably to the more massive of the two dominant product ions, C_2H_5^+ . The discrepancy between the present mobility values and those of previous investigations may be due to the fact that they refer to different ions.

The anode current waveforms do not show any negative-ion component despite the fact that dissociative attachment has been observed²³ under single collision conditions leading to the formation of H^- and CH_2^- ions. We shall discuss the absence of significant attachment further in Sections IIIC and IV.

C. Net ionization coefficient

The net ionization coefficient ($\alpha - \eta$) has been determined from the electron and positive-ion charge waveforms collected at the cathode. A summary of the present values of $(\alpha - \eta)/N$ are given in Table I. Since we have been unable to detect significant attachment, we have labelled these values as the ionization coefficient α/N in Table I. The estimated uncertainties in these values are $\pm 3\%$ for $E/N \geq 100$ Td and $\pm 4\%$ for $E/N < 100$ Td. Our values are also plotted as a function of E/N in Figure 4 and of N/E in Figure 5 to more conveniently compare the data with previous measurements^{19, 24-27} at high and low E/N , respectively. In order to make this comparison meaningful, we have compared the net ionization coefficient of Hunter et al.¹⁹ with the values of α/N determined by other studies which, along with the present study, have not reported significant attachment but yet, strictly speaking, determine the net coefficient. Thus, we have labelled the ordinates of Figures 4 and 5 accordingly as $(\alpha - \eta)/N$. In Figure 4, we also show (by the solid line) the predictions of α/N from the Monte Carlo simulations using the set of electron collision cross sections discussed in

Section IV.

There is generally good agreement among the various measurements over the range $150 \leq E/N \leq 600$ Td. For $E/N > 600$ Td the present data lie up to 20% below previous values. However, of particular interest is the comparison of the data sets for $E/N < 150$ Td. In this region, Hunter et al.¹⁹ have recently reported significantly lower values of net ionization which they attribute to the occurrence of attachment. As noted in the previous section, we have been unable to detect a significant negative-ion current for values of E/N down to 80 Td, and for $E/N < 150$ Td our results are in good agreement with the only other previous^{26,27} measurements in this range.

It is of interest to note that these latter measurements of Cookson et al.²⁶ and Heylen²⁷ have been determined using the spatial current growth technique, i.e., a different technique to that used in the present study, and these authors^{26,27} have identified their derived coefficients as true ionization coefficients. However, although the experimental methods have been different, the analysis of the raw data which has been used by both Cookson et al. and Heylen is similar to that used in the present study, and also gives unambiguous values of the net ionization coefficient. On the other hand, Hunter et al. have used a curve fitting routine for extracting the coefficients α and η directly from the raw data. It is our contention that the discrepancies between the values of the ionization and attachment coefficients deduced by Hunter et al. compared with the present and previous^{26,27} values are largely due to the methods of analysis of the raw data. It has been pointed out previously¹¹ that the coefficient which is most accurately determined from either spatial or temporal current growth is the net ionization coefficient, i.e., the coefficient which appears in the exponent of the current growth expression, and that values of the individual coefficients are subject to much larger uncertainty, particularly in the range of E/N where the net coefficient becomes small.

From the present measurements of cathode and anode waveforms, which give the ratio of ionization to attachment coefficients directly, we place a conservative lower bound of 20 on the ratio α/η . This bound is the basis for the upper limit placed on the

attachment coefficient as a function of E/N shown in Figure 11 and corresponds, for example, to an upper bound for $\eta/N = 5 \times 10^{-21} \text{ cm}^2$ at $E/N = 80 \text{ Td}$, a factor of 21 less than that reported by Hunter et al.¹⁹ In fact, we note that, for $E/N = 80 \text{ Td}$, the value of the net ionization coefficient reported by Hunter et al. is negative (i.e., $\alpha < \eta$), which is completely incompatible with our raw data and evidently with those of Cookson et al. and Heylen. Thus, we identify our measurements of the net ionization coefficient with the true ionization coefficient α/N . In Figure 4, the predictions of the Monte Carlo simulations (shown by the solid line), using the set of electron collision cross sections discussed in Section IV, refer to the ionization coefficient.

Over the range of E/N from 80 to 600 Td, our values of α/N are represented to within $\pm 4\%$ by the expression

$$\alpha/N = 251 \exp[-624/(E/N)], \quad (6)$$

where α/N is expressed in units of 10^{-18} cm^2 and E/N is in Td.

IV. THEORY

The theoretical calculations carried out in this study use electron collision cross sections as input data and calculate the steady state electron energy distribution and the corresponding swarm (electron transport) parameter values. As discussed in Section I, two methods have been used to calculate electron energy distributions and predict swarm parameter values: (i) Monte Carlo simulations, and (ii) two-term spherical harmonic expansion solutions of the Boltzmann transport equation.

A. Monte Carlo simulation

The Monte Carlo simulations use the null-collision method.²⁸⁻³⁰ The Monte Carlo computer code is an extensively revised version of the code developed by Reid³¹ and has been corrected for the errors found by Reid³². The code has been modified to account for the loss of electrons in attachment and the production of secondary electrons in processes involving ionization. Isotropic scattering has been assumed for all collisional processes. The electron energy distribution function is obtained by sampling just before each electron-molecule collision. With the null-event method which uses a constant collision frequency, the distribution function, $f(\epsilon)$, found in this way is identical to the actual distribution function, $f(\epsilon)$.^{29,33}

The collision frequencies (and associated rate coefficients) are calculated by folding the cross section for each specific process with the electron distribution function, $f(\epsilon)$, according to the relation

$$\nu_j/N = \sum \sigma_j(\epsilon) v(\epsilon) f(\epsilon), \quad (7)$$

where ν_j is the frequency per electron for the j -th process, N is the gas number density, $\sigma_j(\epsilon)$ is the energy-dependent cross section for the j -th process, $v(\epsilon)$ is the electron velocity, and $f(\epsilon)$ is the electron energy distribution. The sum is taken over discrete energy bins in which the distribution function is accumulated during the course of the Monte Carlo simulation. The advantage of this approach compared with estimation by

direct counting lies in its ability to return good estimates of collisional frequencies for low-probability processes. We find empirically that the values of the rate coefficients for high-probability processes (e.g., vibrational and dissociation) derived in this manner from the Monte Carlo distribution function agree with those found by direct counting of collisions.

We now discuss the definitions of the transport coefficients used in the Monte Carlo simulation. Two estimates of the electron drift velocity have been calculated. The first, w_z , is the average velocity of the centroid of the electron swarm. Differential values of w_z for successive time bins are given by

$$w_z = \Delta \langle z \rangle / \Delta t, \quad (8)$$

where the notation $\langle z \rangle$ indicates an average over all of the simulation particles. The final value of w_z is computed by performing a linear regression over all of the time bins. The sampling is started at a time far enough into the simulation to allow any initial transients to settle down. The second estimate of the electron drift velocity, $w_{\Delta z}$, is

$$w_{\Delta z} = \langle \Delta z \rangle / \tau, \quad (9)$$

where Δz is the average of the change in z between each collision and τ is the mean time between collisions. The two estimates of drift velocity agree for $E/N < 150$ Td, where the number of electrons is conserved. However, at high E/N , where ionization is the dominant collisional process, the center-of-mass drift velocity, w_z , exceeds $w_{\Delta z}$. This occurs because the spatial distribution of the electron swarm becomes skewed towards the forward direction as a result of the faster ionization rate due to the more energetic electrons at the front of the swarm.³⁴ The w_z values correspond approximately to the experimental drift velocity values. Therefore, the w_z values are used in the theory-experiment comparisons reported in this paper.

The transverse (D_T) and longitudinal (D_L) diffusion coefficients have been determined from the expressions

$$D_T = \langle r^2 \rangle / 4\Delta t = \langle x^2 + y^2 \rangle / 4\Delta t, \quad (10)$$

$$D_L = \langle (z - \langle z \rangle)^2 \rangle / 4\Delta t. \quad (11)$$

Again, the quantities $\langle r^2 \rangle$ and $\langle (z - \langle z \rangle)^2 \rangle$ are recorded in time bins during the course of the Monte Carlo calculation, starting at a time far enough into the simulation to allow any initial transients to have settled down. When the simulation is completed, a linear least-squares fit is used to obtain the transverse and longitudinal diffusion coefficients.

B. Boltzmann equation solutions

In order to quantify the errors due to the use of the two-term spherical harmonic expansion we have also calculated distribution functions and transport coefficients using two different methods which are based on the two-term spherical harmonic expansion. The formulations which we have used are: (i) a backward integration method described by Frost and Phelps³⁵, and (ii) a relaxation method described by Rockwood.³⁶

In both formulations, the collision frequencies and rate coefficients are calculated by folding the cross section for each process with the electron distribution function, $f(\epsilon)$, according to Equation (7) where the summation in these cases is taken over the discrete energy mesh used. The formulations used to calculate the drift velocity and transverse diffusion coefficient in both of the Boltzmann equation methods are those described previously.^{35,36} The formulation used to calculate the longitudinal diffusion coefficient in the backward integration method is that described by Parker and Lowke.³⁷

C. Collision cross section data

We now discuss the set of electron collision cross sections for CH_4 which we have employed in the theoretical calculations. All of the cross sections used here are given in Tables II, III, and IV. Isotropic scattering has been assumed for all of the scattering processes in the Monte Carlo calculations. The published experimental differential cross section data given by Vuskovic and Trajmar³⁸ show that forward

scattering predominates in methane. The assumption of isotropic scattering has been made in this work to simplify the Monte Carlo calculations and to limit the amount of data required to describe the collision cross sections.

The total scattering cross section given in Table II is similar to the total cross section of Ohmori et al.¹⁰ except that we have increased their cross section at energies above 20 eV in order to obtain better agreement between our measured and predicted drift velocities. This cross section is assumed to be the momentum transfer cross section in the Boltzmann calculations which implicitly include the effects of isotropic scattering via the $(1 - \cos \vartheta)$ weighting in the momentum transfer cross section. However, it should be noted that the two-term representation of the electron energy distribution in the Boltzmann calculations reported here is unable to accurately represent the electron energy distribution in methane where forward scattering predominates.

The vibrational excitation cross sections given in Table III are those of Ohmori et al.¹⁰ These cross sections have been obtained from the limited experimental data which is available as described in Ref. 10.

There are no known bound electronic states of CH_4 . All electronic excitation leads to dissociation where two or more fragments are produced. We have estimated the cross section for neutral dissociation, i.e. dissociation of CH_4 into neutral fragments, by subtracting the total dissociative ionization cross section of Chatham et al.²¹ from the total dissociation cross section of Winters.³⁹ The threshold for neutral dissociation has been set to 9 eV based on the electron energy-loss spectra for CH_4 reported by Vuskovic and Trajmar³⁸ and Dillon et al.⁴⁰ The neutral dissociation cross section obtained in this way is much larger than the individual measured cross sections⁴¹ for dissociation processes where one of the neutral fragments is in a radiating excited state or a metastable excited state. Furthermore, the number of possible dissociation processes is very large. Thus, estimation of the total neutral dissociation cross section by adding the cross sections for all possible channels is impractical. The total dissociation cross section has been approximated by a straight line starting at the 9 eV

threshold and increasing to $2 \times 10^{-15} \text{ cm}^2$ at 20 eV. This approximation agrees well with the measured values of Winters for $14 < \epsilon < 20$ eV and is somewhat higher for lower energies. As an approximation of the continuous energy loss spectrum in CH_4 , we have divided the total neutral dissociation cross section into four partial cross sections with thresholds at 9, 10, 11, and 12 eV. These four cross sections, which are shown in Figure 6, are chosen so that their sum is equal to the total neutral dissociation cross section described above. The predicted values of the ionization coefficient for $E/N < 150 \text{ Td}$ are very sensitive to the assumed ionization and dissociation cross sections near threshold, as discussed below. Thus, the threshold shape of the total neutral dissociation cross section can be determined by comparing predicted and measured ionization coefficients if we accept the measured ionization cross section shape.

We have used the ionization cross section values of Chatham et al.²¹ for energies above 14.3 eV and those of Rapp and Englander-Golden⁴² for energies between 12.6 and 14.3 eV. We have found that taking account of the upcurving of the ionization cross section shape measured by Rapp and Englander-Golden in this energy range has a large effect on the predicted ionization coefficient, as discussed in Section V.

The total dissociative attachment cross section which we have used is that measured by Sharp and Dowell.²³ The total cross section comprises two components corresponding to formation of H^- and CH_2^- , which are not completely resolved in the measurements. In order to estimate the contributions of each process to the total attachment coefficient we have estimated the individual H^- and CH_2^- cross sections as follows. From the total cross section for dissociative attachment of Sharp and Dowell²³ which represents the sum of the H^- and CH_2^- contributions, we subtract an estimate for the H^- cross section based on the shape of the D^- (from CD_4) cross section of Sharp and Dowell²³, yielding the H^- and CH_2^- cross sections shown in Figure 7. The H^- cross section rises to a flattened peak of $7.6 \times 10^{-20} \text{ cm}^2$ from 9 eV to 10 eV, whereas

the CH_2^- cross section has a peak of $4.3 \times 10^{-20} \text{ cm}^2$ at 10.8 eV. The effect of our model of attachment is to favor the production of H^- over CH_2^- . However, we note that the total cross section for attachment in CH_4 is sufficiently small that it has little influence on the electron energy distribution function.

V. SIMULATION RESULTS

A. Electron drift velocity

We present our theoretical results for drift velocity in Figure 8 where we have plotted the ratio of the various theoretical values to our measured values in order to show the small differences between theory and experiment more clearly. The experimental determination of drift velocity is based on the arrival time of the peak of the electron component of the total anode current; it corresponds, approximately, to the calculated w_z in the Monte Carlo calculations. Agreement between experimental and Monte Carlo values is within 15% over the entire range of E/N and is much closer for most of the E/N range. Without modification of the momentum transfer cross section of Ohmori et al.,¹⁰ the disagreement between predicted and measured values would be as large as 20% at high E/N . The values of w_z and $w_{\Delta z}$ predicted from the Monte Carlo calculations agree to within 1% for $E/N < 150$ Td, where ionization is negligible. The $w_{\Delta z}$ values are smaller at higher values of E/N as shown in Figure 9. The drift velocity values calculated by numerically solving the Boltzmann equation correspond to $w_{\Delta z}$. However, the Boltzmann drift velocity values differ from the experimental and Monte Carlo values because the two-term expansion is not an adequate representation of the distribution function, especially at high E/N , as shown in Figure 8. The backward integration results are also in error at high E/N because the secondary electrons produced in ionizing collisions are not taken into account in the backward integration computer code.

B. Ionization and attachment coefficients

Our theoretical results for the ionization coefficient are shown in Figure 10. We have again plotted the ratio of the various theoretical values to the measured values reported above because the differences between theory and experiment are again small. The Monte Carlo values are within 12% of the experimental values over the entire range of E/N where the dynamic range of the α/N values is more than three

orders of magnitude. The α/N values predicted from the Boltzmann code are well above the experimental and Monte Carlo values over the entire E/N range as shown in Figure 10. This large disagreement is again an indication of the inability of the two-term expansion to represent the distribution function in CH_4 . The backward integration Boltzmann results are much larger than the relaxation Boltzmann results at high E/N because secondary electrons are neglected in the backward integration computer code.

As noted in Section IIIC, we have been unable to detect any evidence of attachment in our experimental measurements and estimate an experimental upper bound on $\eta/N = 5 \times 10^{-21} \text{ cm}^2$ at $E/N = 80 \text{ Td}$, the lowest E/N where we are able to make accurate measurements of the net ionization coefficient. Figure 11 shows the attachment coefficient values which we predict using the H^- and CH_2^- cross sections shown in Figure 7. Note that the predicted η/N values due to CH_2^- alone are below our experimentally estimated upper bound except near the threshold region where the predicted values of η/N lie above the experimental detection threshold. However, the predicted values of η/N due to H^- are larger than our upper bound for values of $E/N < 150 \text{ Td}$. If the attachment cross section is assumed to be accurate, the only plausible explanation for the absence of an observable negative-ion current in the drift-tube measurements is that the negative ions suffer collisional detachment in a swarm environment. Collisional detachment is more likely to occur in the case of H^- species since they can readily gain energy from the applied field and are likely to be produced with appreciable kinetic energy. In fact, if the H^- ions are assumed to suffer collisional detachment reactions, then the Monte Carlo predictions are consistent with the experimental data, except near the onset region of the $\eta(\text{CH}_2^-)/N$ curve, where the corresponding threshold region in the interpolated CH_2^- cross section is subject to the largest uncertainty.

C. Electron diffusion/mobility ratio

The available experimentally measured values of the transverse^{9,43-45} and longitudinal^{9,46-48} diffusion coefficients divided by mobility, D_T/μ and D_L/μ , are compared with our calculated values in Figures 12 and 13. There is considerable scatter in the experimental values as shown by the experimental data in these figures. There is also considerably larger scatter in the Monte Carlo results for the diffusion coefficients as shown by the Monte Carlo values in the figures. However, the Monte Carlo D_T/μ values are in generally good agreement with the experimental values of Hunter et al.⁴⁴ at low E/N and Al-Amin et al.⁹ at high E/N. The D_T/μ values from the backward integration and relaxation Boltzmann calculations agree well with each other but are well above the measured and Monte Carlo values over the entire range of E/N as shown in Figure 12. The scatter in the experimental D_L/μ values is very large as shown in Figure 13. The calculated Monte Carlo and backward integration Boltzmann D_L/μ values agree well except at high E/N. The calculated Monte Carlo D_L/μ values are also in good to reasonable agreement with the experimental values of Al-Amin et al.⁹ over the entire range of E/N examined here.

The comparison between theory and experiment shown in Figures 12 and 13 suggests that both the theoretical calculation and experimental measurement of D/μ should be improved. One approach to this problem would be to compare the actual measured and calculated transverse and longitudinal distributions of electrons vs. position at different times. This approach would have the advantage of eliminating the relatively involved procedures which are used to estimate diffusion coefficient values from the experimental data.

VI. SUMMARY

In this paper, we have presented measurements of the electron drift velocity, positive-ion mobility, and ionization coefficient over a wide range of E/N , carried out in the same pulsed drift tube apparatus. The values of electron drift velocity are in generally good agreement with previously reported values. Our values of the ionization coefficient are in reasonably good agreement with those of Cookson et al.²⁶ and of Heylen²⁷ but differ significantly from the recent net ionization coefficient data of Hunter et al.¹⁹ in the threshold region of E/N . Further, in keeping with the earlier studies of Cookson et al. and Heylen and in contrast to the results reported by Hunter et al., we have not detected the presence of significant attachment in methane.

Numerical calculations of the electron drift velocity and ionization coefficient have been carried out for methane using a Monte Carlo simulation method and two different approaches to the solution of the Boltzmann transport equation both of which utilise a two-term expansion of the electron energy distribution function. The input data for these calculations is a set of electron collision cross sections. The cross section set includes a total momentum transfer cross section which is based primarily on the present and previous drift velocity measurements. The total momentum transfer cross section is interpreted as the total cross section in the Monte Carlo calculations since isotropic scattering is assumed in the Monte Carlo calculations. The remaining cross sections are cross sections for vibrational excitation and ionization based on published experimental cross section measurements, and a cross section for dissociation into neutral products obtained by subtracting a measured dissociative ionization cross section from a measured total dissociation cross section. This total neutral dissociation cross section has been sub-divided into four partial cross sections in order to approximately represent the continuous electron energy loss spectrum which is observed experimentally in CH_4 . We think that our derived cross section set is the most realistic one proposed to date since it reflects available experimental data and also yields predicted values of electron drift velocity and ionization coefficient from Monte Carlo simulations which agree with our measured values to within 15%. On the other hand, predicted values of the swarm parameters from numerical solutions of the

Boltzmann equation using this same cross section set are in poor agreement with experimental values. We conclude, in agreement with previous authors that, in the case of methane, the two-term expansion is not an adequate description of the electron energy distribution function for the reasons discussed in Section V.

As far as the attachment situation is concerned, the values of the total attachment coefficient predicted from the Monte Carlo simulations are significantly larger than the upper limit set by our measurements. At present, the only plausible explanation for this disagreement is that most of the negative ions formed suffer collisional detachment in a swarm environment. From our interpolation of the measurements of Sharp and Dowell,²³ it appears that the cross section for H⁻ formation is larger and the threshold energy lower than that for CH₂⁻ formation. Thus, the predicted contribution of H⁻ formation to the total attachment coefficient is larger than that of CH₂⁻ by more than a factor of four for E/N < 150 Td. If it is assumed that only the H⁻ ions suffer detachment then our predicted and measured attachment coefficients are self consistent except near the threshold region where the predicted values may be subject to large uncertainty as a result of our interpolation. The H⁻ ions are particularly susceptible to detachment since they have a relatively low binding energy, are probably formed with appreciable kinetic energy, and can readily gain energy from the applied field. Further mass and fragment-energy resolved measurements of the attachment cross section would be desirable to clarify this question.

The small discrepancy remaining between predicted and measured swarm parameters could be reduced by further fine adjustment of the cross sections. However, we do not feel that additional effort in this direction is justified in view of our assumption of isotropic scattering in the numerical simulations. In fact, it is known that with the notable exception of vibrational excitation, other elastic and inelastic scattering collisions in methane are anisotropic. We have performed additional calculations to study the influence of anisotropic angular scattering in methane on the predicted electron energy distribution and the predicted swarm parameters. The results of these calculations will be reported in a separate paper.

ACKNOWLEDGMENTS

We are grateful to P. J. Chantry for many fruitful discussions. We also thank L. D. Kurtz for technical support. This work was supported in part by the Army Research Office Contract DAAG29-84-C-003.

REFERENCES

1. J. F. Lowry, L. E. Kline, and J. V. R. Heberlein, IEEE Trans. on Plasma Sci. PS-14, 454 (1986).
2. L. E. Kline, W. D. Partlow, and W. E. Bies, Proc. 6th Electrochemical Soc. Symp. on Plasma Processing (Pennington, 1987), ECS Vol 87-6, p. 289.
3. M. Kamo, Y. Sato, S. Matsumoto, and N. Setaka, J. Cryst. Growth, 62, 642 (1983); Y. Mitsuda, Y. Kojima, T. Yoshida, and K. Akashi, J. Mat. Sci. 22, 1557 (1987).
4. S. L. Lin, R. E. Robson, and E. A. Mason, J. Chem. Phys. 71, 3483 (1979).
5. L. C. Pitchford, S. V. O'Neil, and J. R. Rumble, Jr., Phys. Rev. A: 23, 294 (1981).
6. G. L. Braglia, J. Chem. Phys. 74, 2990 (1981).
7. G. N. Haddad, Aust. J. Phys. 38, 677 (1985).
8. L. E. Kline, IEEE Trans. on Plasma Sci. PS-10, 224 (1982).
9. S. A. J. Al-Amin, H. N. Kucukarpaci, and J. Lucas, J. Phys. D: 18, 1781 (1985).
10. Y. Ohmori, K. Kitamori, M. Shimozuma, and H. Tagashira, J. Phys. D: 19, 437 (1986).
11. D. K. Davies, submitted to Rev. Sci. Instrum.
12. G. S. Hurst, L. B. O'Kelly, E. B. Wagner, and J. A. Stockdale, J. Chem. Phys. 39, 1341 (1963).
13. J. Lucas, Int. J. Electron. 17, 43 (1964).
14. D. K. Davies, J. Appl. Phys. 47, 1916 (1976).
15. L. Frommhold, Z. Phys. 156, 144 (1959).
16. H. Tholl, Z. Phys. 178, 183 (1964).
17. A. H. Cookson, Br. J. Appl. Phys. 17, 1069 (1966).
18. W. J. Pollock, Trans. Faraday Soc. 64, 2919 (1968).
19. S. R. Hunter, J. G. Carter, and L. G. Christophorou, J. Appl. Phys. 60, 24 (1986).
20. H. Schlumbohm, Z. Phys. 182, 317 (1965).
21. H. Chatham, D. Hills, R. Robertson, and A. Gallagher, J. Chem. Phys. 81, 1770 (1984).
22. D. Albritton, Atomic Data and Nuclear Tables, 22, 1 (1978).
23. T. E. Sharp and J. T. Dowell, J. Chem. Phys. 46, 1530 (1967).

24. H. Schlumbohm, *Z. Angew. Phys.* 11, 156 (1959); *Z. Phys.* 184, 492 (1965).
25. D. K. Davies and E. Jones, *Proc. Phys. Soc. London*, 82, 537 (1963).
26. A. H. Cookson, B. W. Ward, and T. J. Lewis, *Br. J. Appl. Phys.* 17, 891 (1966).
27. A. E. D. Heylen, *Int. J. Electron.* 39, 653 (1975).
28. S. L. Lin and J. N. Bardsley, *J. Chem. Phys.* 66, 435 (1977).
29. G. L. Braglia, *Lett. Nuovo Cimento* 31, 183 (1981); *Contrib. Plasma Phys.* 25, 567 (1985).
30. P. J. Price, *Semiconductors and Semimetals* (Academic Press, New York, 1979), Vol. 14, Ch. 4.
31. I. D. Reid, *Aust. J. Phys.* 32, 231 (1979).
32. I. D. Reid, *Aust. J. Phys.* 35, 473 (1982).
33. L. Friedland, *Phys. Fluids*, 20, 1461 (1977).
34. Y. Sakai, H. Tagashira, and S. Sakamoto, *J. Phys. D*: 10, 1035 (1977).
35. L. S. Frost and A. V. Phelps, *Phys. Rev.* 127, 1621 (1962).
36. S. D. Rockwood, *Phys. Rev. A*: 8, 2348 (1973).
37. J. H. Parker and J. J. Lowke, *Phys. Rev.* 181, 290 (1969).
38. L. Vuskovic and S. Trajmar, *J. Chem. Phys.* 78, 4947 (1983).
39. H. F. Winters, *J. Chem. Phys.* 63, 3462 (1975); *Private communication of tabulated cross sections* (1985).
40. M. A. Dillon, R. G. Wang, and D. Spence, *J. Chem. Phys.* 80, 5581 (1984).
41. See, for example, J. A. Schiavone, D. E. Donohue, and R. S. Freund, *J. Chem. Phys.* 67, 759 (1977) and the references therein.
42. D. Rapp and P. Englander-Golden, *J. Chem. Phys.* 43, 1464 (1965).
43. C. S. Lakshminarasimha and J. Lucas, *J. Phys. D*: 10, 313 (1977).
44. S. R. Hunter, J. G. Carter, and L. G. Christophorou, *J. Appl. Phys.* 58, 3001 (1985).
45. P. G. Millican and I. C. Walker, *J. Phys. D*: 20, 193 (1987).
46. X. Fink and P. Huber, *Helv. Phys. Acta* 38, 717 (1965).
47. H. Schlumbohm, *Z. Phys.* 182, 306 (1965).
48. L. Frommhold, *Z. Phys.* 160, 554 (1960).

TABLE I. Summary of the experimental (Expt.) values and Monte Carlo (MC) predictions of swarm parameters in methane.

E/N 10^{-17}V cm^2	$w_e, 10^6 \text{cm/s}$			μ_+ $\text{cm}^2/\text{V s}$	$\alpha/N, 10^{-18} \text{cm}^2$		$\eta/N, 10^{-18} \text{cm}^2$		$D_T/\mu, \text{V}$	$D_L/\mu, \text{V}$
	Expt. w'	MC w_z	MC $w_{\Delta z}$		Expt.	MC	MC H^-	MC CH_2^-	MC	MC
10.00	7.92	7.42	7.50						0.86	0.15
12.50	6.84									
15.00	6.37									
17.50	5.76									
20.00	5.49	5.56	5.46						2.09	0.26
25.00	5.35									
30.00	5.27	5.23	5.17						3.02	0.40
35.00	5.16									
40.0	5.25									
50.0	5.38	5.34	5.32				0.0135	0.0015	3.88	0.76
60.0	5.45	5.59							4.56	1.07
70.0	5.81	6.02	5.73			0.032	0.062	0.0090	4.59	1.44
80.0	6.40	6.53	6.29	2.49	0.102	0.110	0.085	0.015	4.79	1.77
90.0	6.83	7.12	6.85	2.64	0.241	0.260	0.103	0.019	4.95	2.00
100.0	7.40	7.61	7.34	2.76	0.50	0.55	0.118	0.024	4.87	2.10
112.5	8.14	8.39	8.09	2.85	0.96	1.03	0.126	0.029	4.76	2.18
125.0	8.86	9.07	8.85	2.97	1.71	1.74	0.136	0.032	5.06	2.52
150.0	10.2	10.6	10.3	3.16	4.05	3.66	0.140	0.037	5.02	2.62
175.0	11.6			3.31	7.29					
200.0	13.2	13.8	13.0	3.40	10.8	9.49	0.130	0.039	5.24	2.78
250.0	16.3			3.42	19.8					
300.0	19.9	19.6	18.0	3.35	31.0	26.6	0.105	0.037	4.71	3.70
400	26.6			3.18	52					
500	33.1	32.7	27.4	3.05	72	67.6	0.067	0.026	5.28	4.63
600	40.0			2.93	92					
700	46.3	46.9	36.7	2.82	111	106	0.046	0.019	5.50	4.30
800	52.3			2.71	125					
900	58.7			2.63	134					
1000	66.2	67.5	50.6	2.52	145	162	0.029	0.013	5.60	7.23

TABLE II. Values of the momentum transfer cross section, Q_m , in units of 10^{-16} cm^2 as a function of electron energy, ϵ , in eV used in the numerical simulations.

ϵ	Q_m	ϵ	Q_m	ϵ	Q_m	ϵ	Q_m
0.000	50.0	0.200	0.700	6.00	14.7	150	1.07
0.010	40.0	0.300	0.560	8.00	16.1	200	0.900
0.015	24.4	0.400	0.650	10.00	15.5	300	0.714
0.020	17.0	0.600	0.953	15.0	12.6	400	0.612
0.030	10.2	0.800	1.40	20.0	8.80	600	0.496
0.040	7.30	1.00	1.90	30.0	4.76	800	0.430
0.060	4.60	1.50	3.10	40.0	3.26	1000	0.384
0.080	2.90	2.00	4.40	60.0	2.13	3000	0.120
0.100	2.00	3.00	7.20	80.0	1.67	10000	0.0360
0.150	0.990	4.00	10.5	100.0	1.43		

TABLE III. Values of the inelastic cross section, in units of 10^{-16} cm^2 , for vibrational excitation, Q_v , as a function of electron energy, ϵ , in eV used in the numerical simulations. The energy losses assigned to the 2-4 and 1-3 cross sections are 0.162 eV and 0.361 eV, respectively.

ϵ	Q_v		ϵ	Q_v	
	2-4	1-3		2-4	1-3
0.16	0.000		2.50	0.257	0.182
0.20	0.130		3.00	0.302	0.241
0.25	0.553		4.00	0.416	0.423
0.30	0.689		5.00	0.585	0.650
0.36		0.000	6.00	0.793	0.910
0.40	0.754		6.50	0.923	
0.45		0.130	7.00	1.080	1.170
0.50	0.702	0.208	7.50	1.140	1.200
0.60	0.604	0.299	8.00	1.110	1.157
0.66		0.312	9.00	0.923	0.884
0.75		0.299	10.0	0.793	0.728
0.80	0.436		15.0	0.520	0.364
0.84		0.260	20.0	0.468	0.286
0.90		0.238	40.0	0.345	0.169
1.00	0.312	0.208	70.0	0.208	0.065
1.20	0.247	0.175	100	0.130	0.039
1.50	0.221	0.153	150	0.060	0.000
1.80		0.143	200	0.000	
2.00	0.225	0.147			

TABLE IV. Values of the inelastic cross sections, in units of 10^{-16} cm^2 , for attachment, Q_- , dissociation, Q_d , and ionization, Q_i , as a function of electron energy, ϵ , in eV used in the numerical simulations. The energy corresponding to the first entry in each cross section column is the energy loss assigned to that process.

ϵ	Q_-		Q_d				Q_i	
	H^-	CH_2^-	1	2	3	4	CH_4^+	CH_3^+
7.70	0.0000							
9.00	0.0008	0.0000	0.000					
10.0	0.0008		0.300	0.000				
10.8		0.0004						
11.0				0.300	0.000			
12.0	0.0000				0.300	0.000		
12.6							0.000	
13.0			0.300	0.300	0.300	0.300		
13.2		0.0000						
13.5							0.034	
14.0							0.074	
14.3								0.000
14.5							0.130	
15.0			0.400	0.400	0.400	0.400	0.170	0.035
20.0			0.540	0.540	0.540	0.540	0.680	0.390
25.0			0.540	0.540	0.540	0.540		
30.0							1.260	1.040
50.0							1.690	1.610
70.0							1.780	1.780
100			0.540	0.540	0.540	0.540	1.780	1.780
150			0.485	0.485	0.485	0.485		
200			0.450	0.450	0.450	0.450	1.510	1.510
300			0.400	0.400	0.400	0.400	1.190	1.190
400			0.375	0.375	0.375	0.375	1.000	1.000
500			0.350	0.350	0.350	0.350	0.900	0.900
1000			0.150	0.150	0.150	0.150	0.450	0.450
2000			0.075	0.075	0.075	0.075	0.225	0.225
5000			0.030	0.030	0.030	0.030	0.090	0.090
10000			0.015	0.015	0.015	0.015	0.045	0.045

FIGURE CAPTIONS

Figure 1. Schematic diagram of the experimental arrangement.

Figure 2. Comparison of the present experimental values of electron drift velocity as a function of E/N in methane with previous measurements and with the Monte Carlo predictions.

Figure 3. Comparison of the present measurements of positive-ion mobility as a function of E/N with previous values.

Figure 4. Comparison of the present values of the net ionization coefficient as a function of E/N with previous measurements and with the predictions of the Monte Carlo simulations. As discussed in the text, these values are to be identified with the true ionization coefficient α/N , with the exception of those of Ref. 19.

Figure 5. Comparison of the present values of the net ionization coefficient as a function of N/E with previous measurements. As discussed in the text, these values are to be identified with the true ionization coefficient α/N , with the exception of those of Ref. 19. The line denotes the fit to the data by the expression $\alpha/N = 2.51 \times 10^{-16} \exp[-624/(E/N)]$.

Figure 6. The dissociation cross sections assumed for the numerical simulations.

Figure 7. Dissociative attachment cross sections for H^- and CH_2^- formation from CH_4 deduced from the measurements of Sharp and Dowell for use in the numerical simulations.

Figure 8. Ratio of the Monte Carlo and Boltzmann numerical predictions of electron drift velocity as a function of E/N to the present measurements. ■ Monte Carlo; ◆ Boltzmann, method of Ref. 35; ▲ Boltzmann, method of Ref. 36.

Figure 9. Comparison of the center of mass (■) and average (◆) electron drift velocity as a function of E/N predicted from the Monte Carlo simulations.

Figure 10. Ratio of the Monte Carlo and Boltzmann numerical predictions of the ionization coefficient as a function of E/N to the present measurements. The symbols are the same as in Figure 8.

Figure 11. Comparison of the Monte Carlo numerical predictions of attachment coefficient for H^- (◆), CH_2^- (▲), and total (■) as a function of E/N with the estimated upper limit of the present measurements (□) and the previous data of Hunter et al. (△).

Figure 12. Comparison of the Monte Carlo (■) and Boltzmann (▲) numerical predictions of the ratio D_T/μ as a function of E/N with the previous measurements of Ref. 43 (x), Ref. 9 (+), and Ref. 44 (▲). The data of Ref. 45 agree with those of Ref. 44 to within a few percent.

Figure 13. Comparison of the Monte Carlo (■) and Boltzmann (▲) numerical predictions of the ratio D_L/μ as a function of E/N with the previous measurements of Ref. 9 (+), Ref. 46 (▲), Ref. 47 (x), and Ref. 48 (■).

Dwg. 1716897

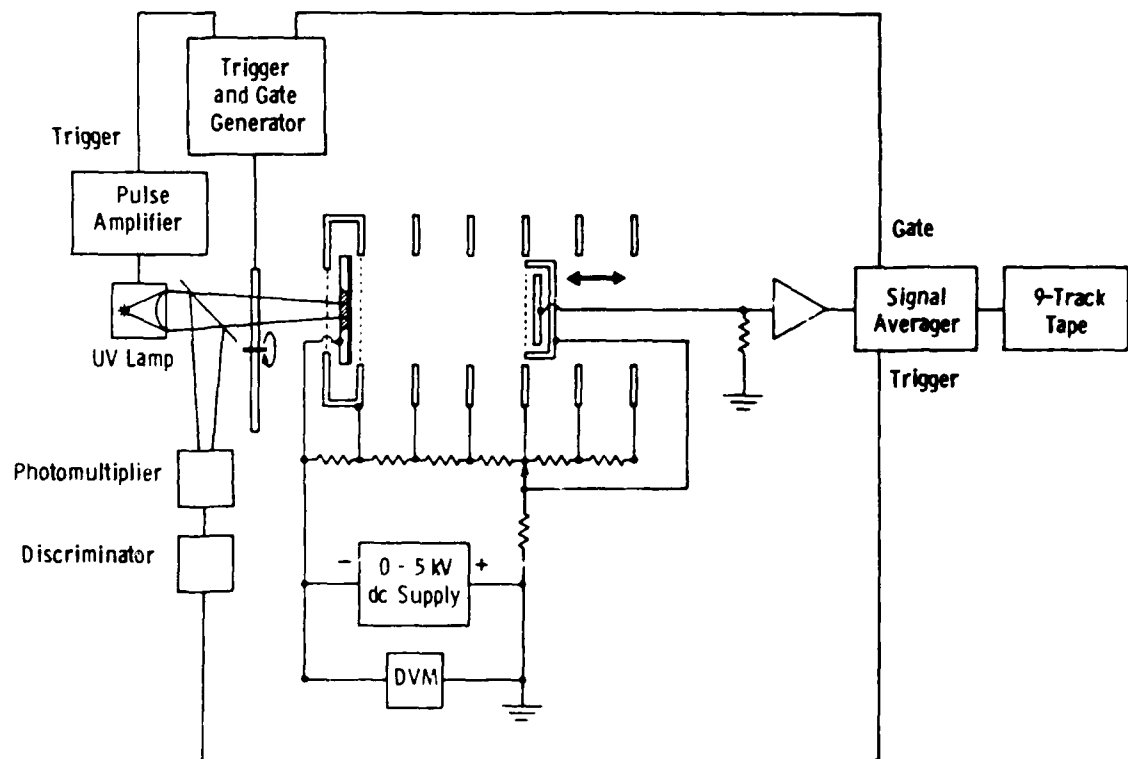


Figure 1. Schematic diagram of the experimental arrangement.

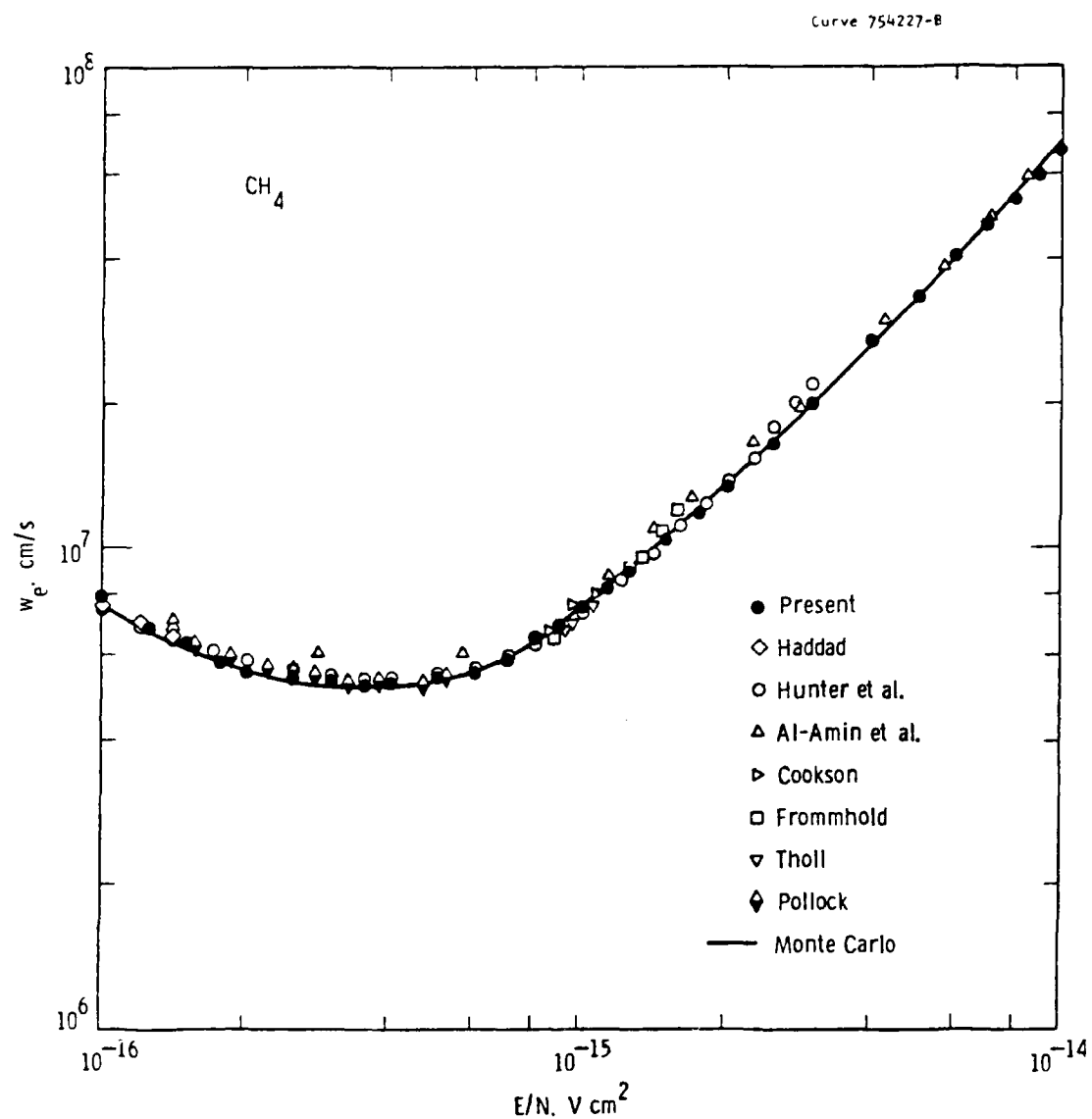


Figure 2. Comparison of the present experimental values of electron drift velocity as a function of E/N in methane with previous measurements and with the Monte Carlo predictions.

Curve 754222-A

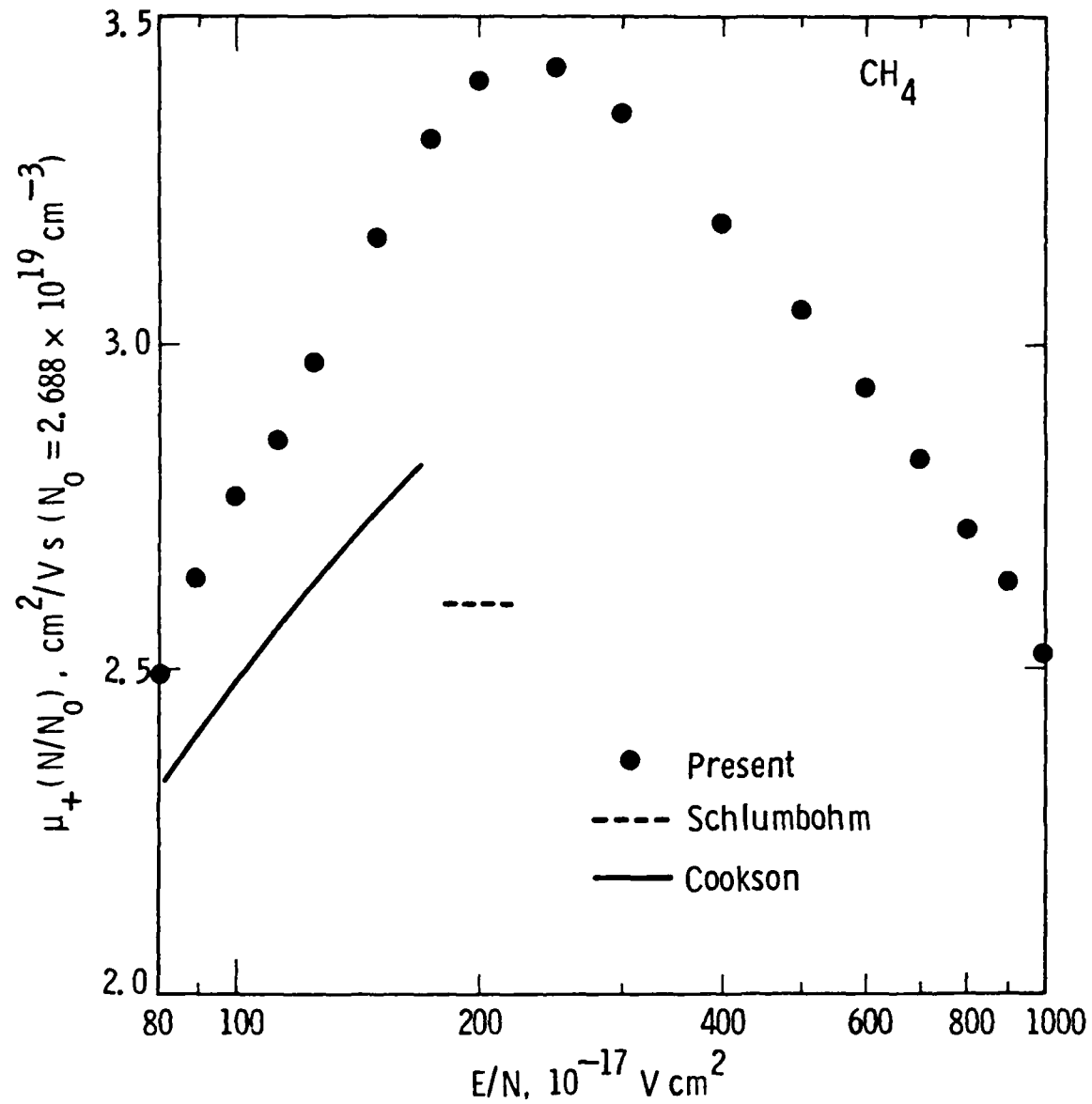


Figure 3. Comparison of the present measurements of positive-ion mobility as a function of E/N with previous values.

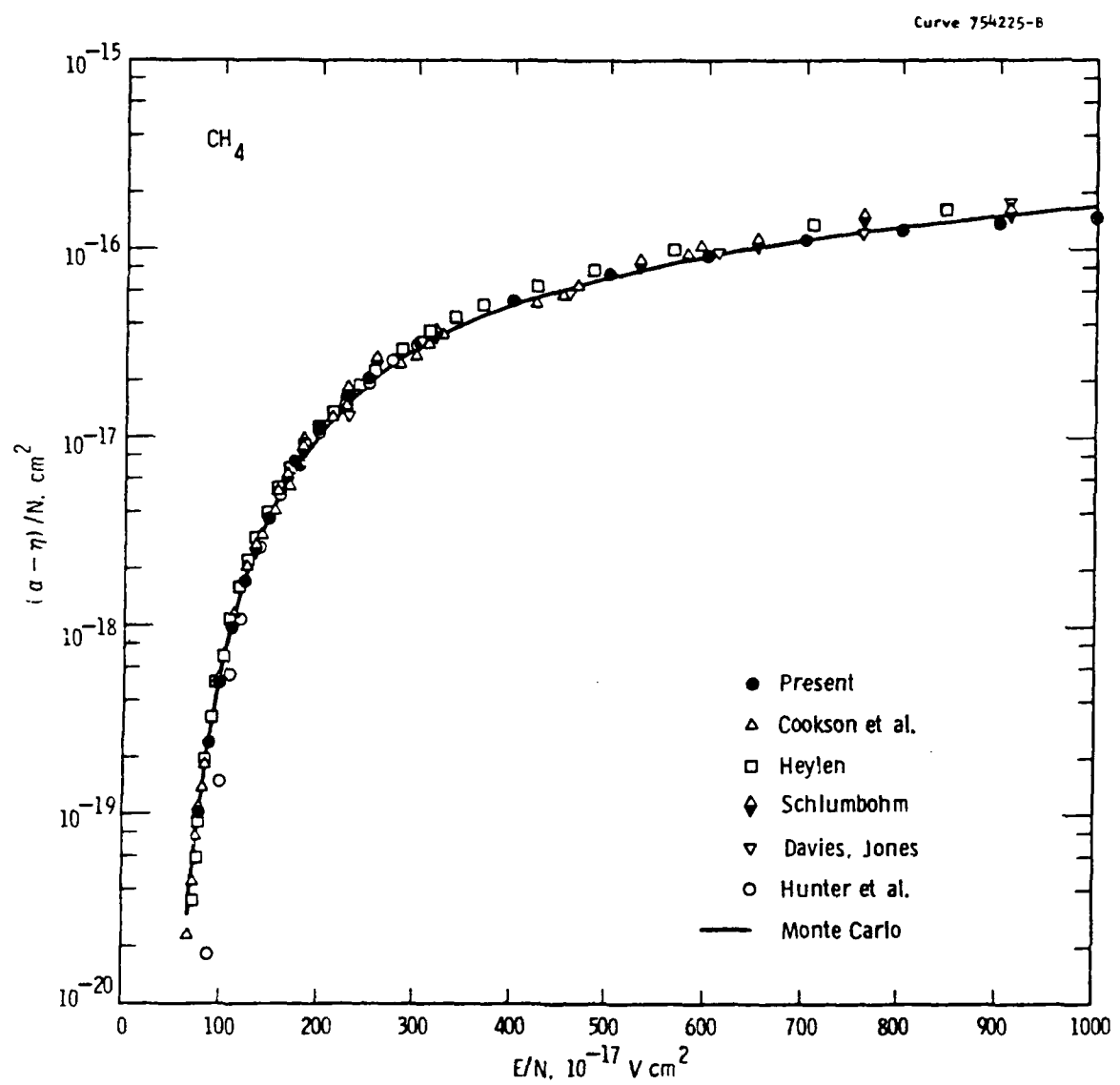


Figure 4. Comparison of the present values of the net ionization coefficient as a function of E/N with previous measurements and with the predictions of the Monte Carlo simulations. As discussed in the text, these values are to be identified with the true ionization coefficient α/N , with the exception of those of Ref. 19.

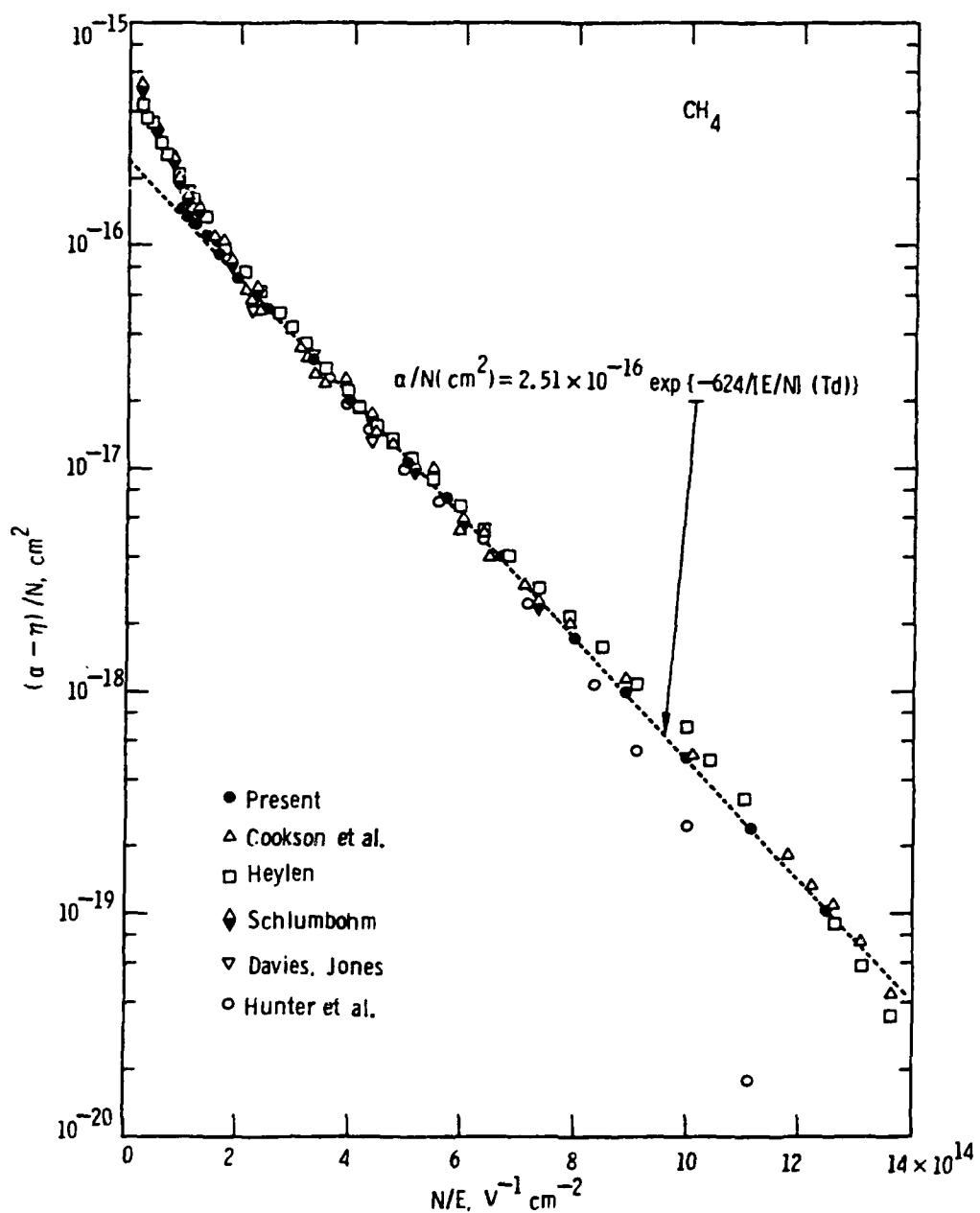


Figure 5. Comparison of the present values of the net ionization coefficient as a function of N/E with previous measurements. As discussed in the text, these values are to be identified with the true ionization coefficient α/N , with the exception of those of Ref. 19. The line denotes the fit to the data by the expression $\alpha/N = 2.51 \times 10^{-16} \exp[-624/(E/N)]$.

Curve 755666-A

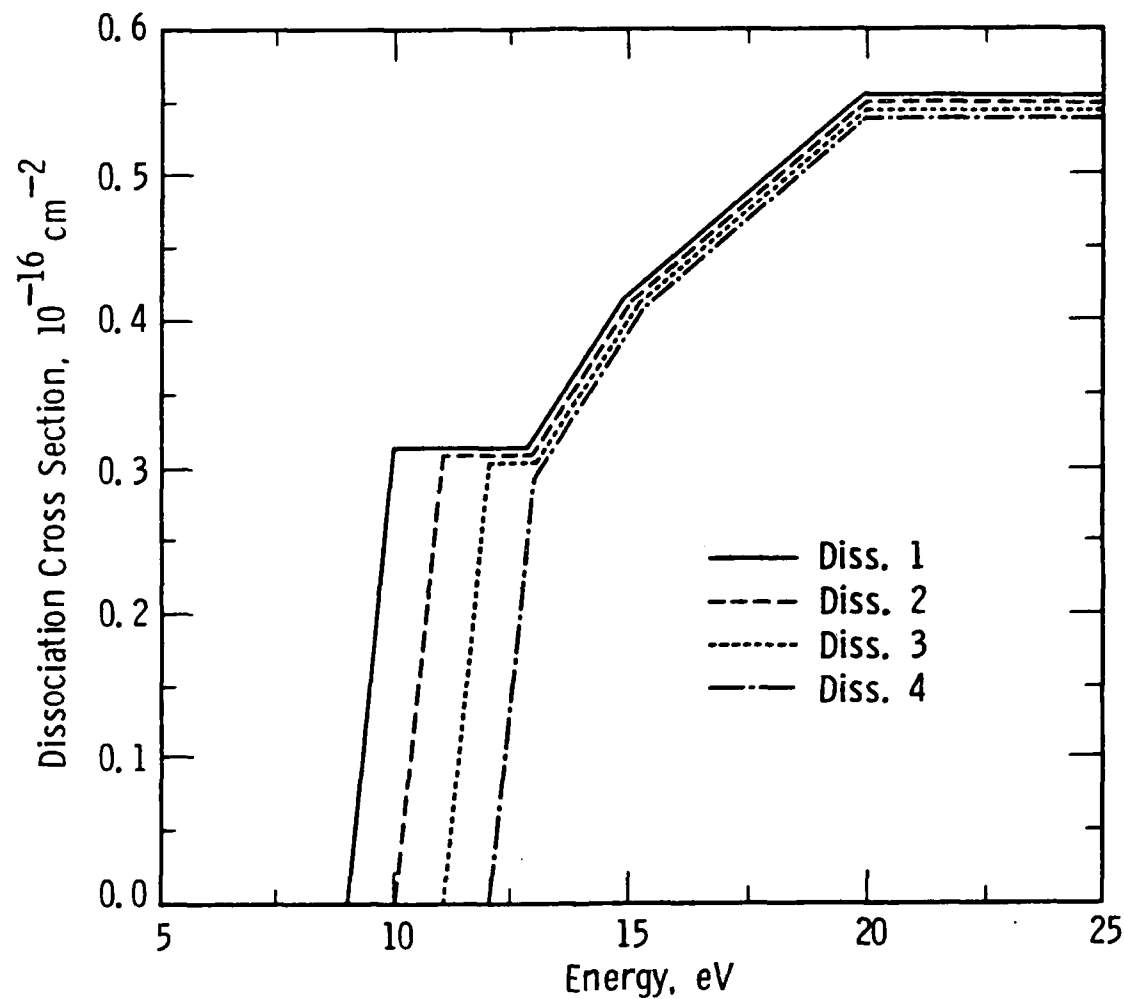


Figure 6. The dissociation cross sections assumed for the numerical simulations.

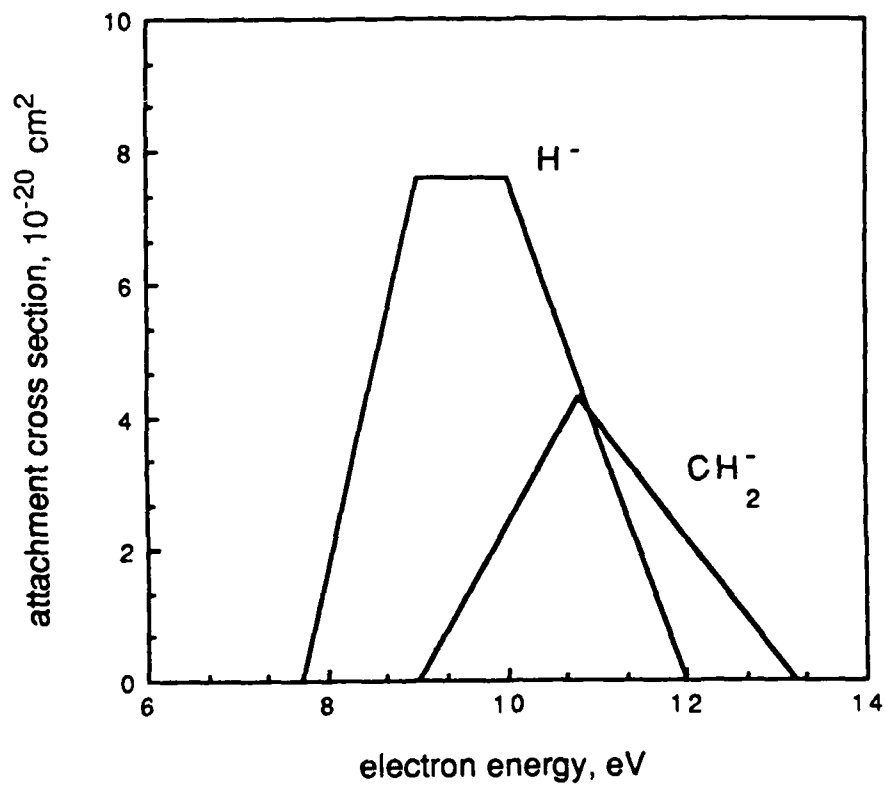


Figure 7. Dissociative attachment cross sections for H^- and CH_2^- formation from CH_4 deduced from the measurements of Sharp and Dowell for use in the numerical simulations.

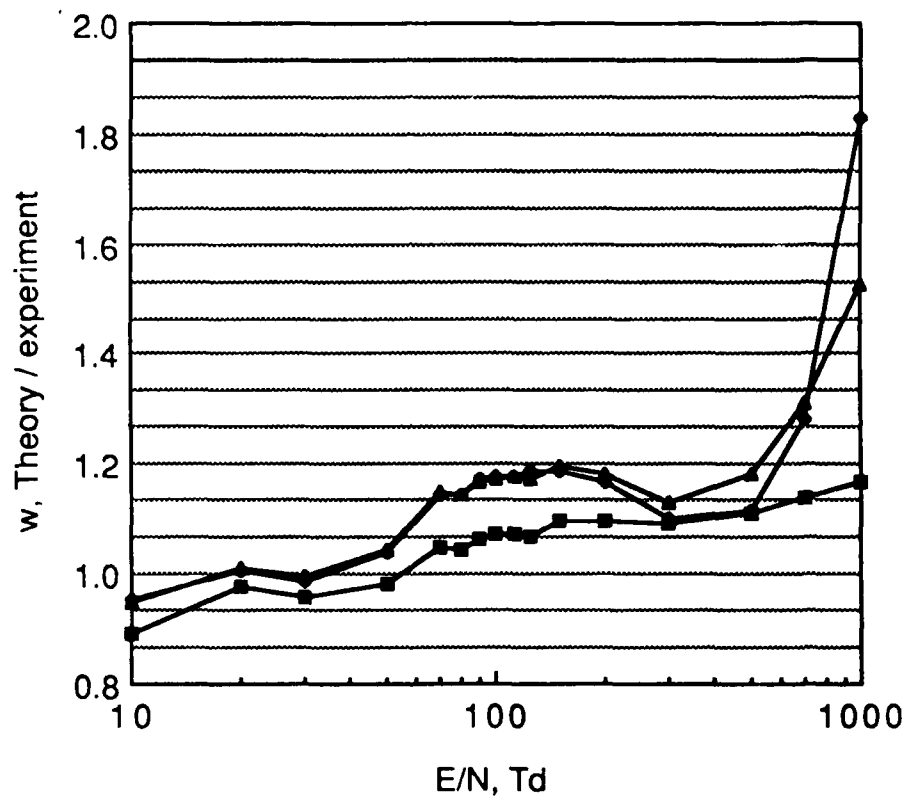


Figure 8. Ratio of the Monte Carlo and Boltzmann numerical predictions of electron drift velocity as a function of E/N to the present measurements. ■ Monte Carlo; ◆ Boltzmann, method of Ref. 35; ▲ Boltzmann, method of Ref. 36.

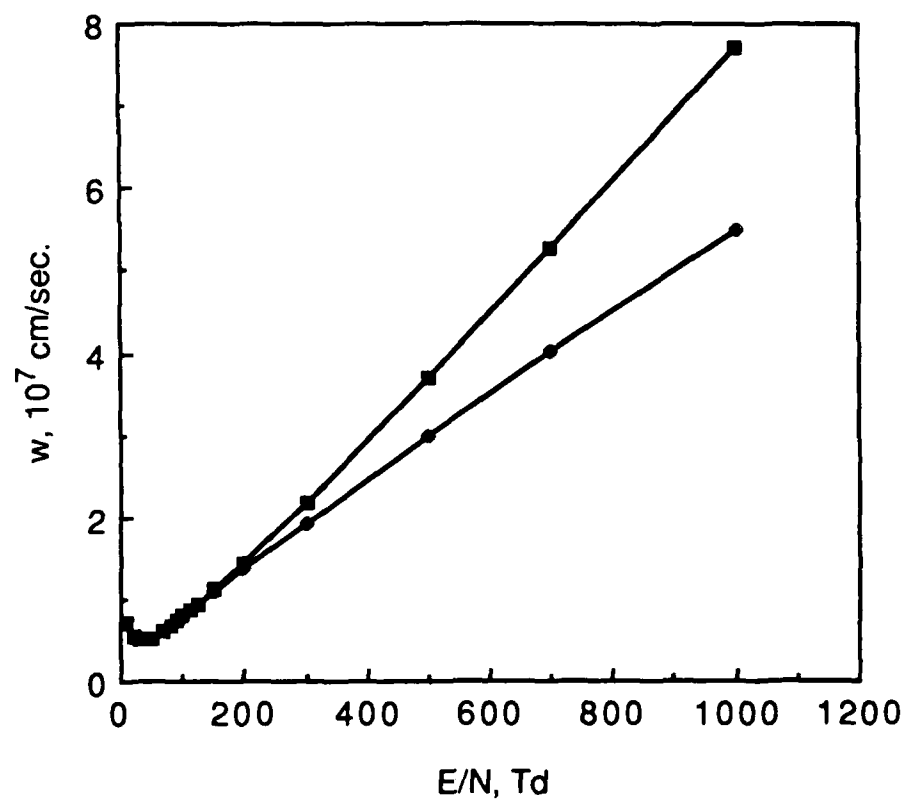


Figure 9. Comparison of the center of mass (■) and average (◆) electron drift velocity as a function of E/N predicted from the Monte Carlo simulations.

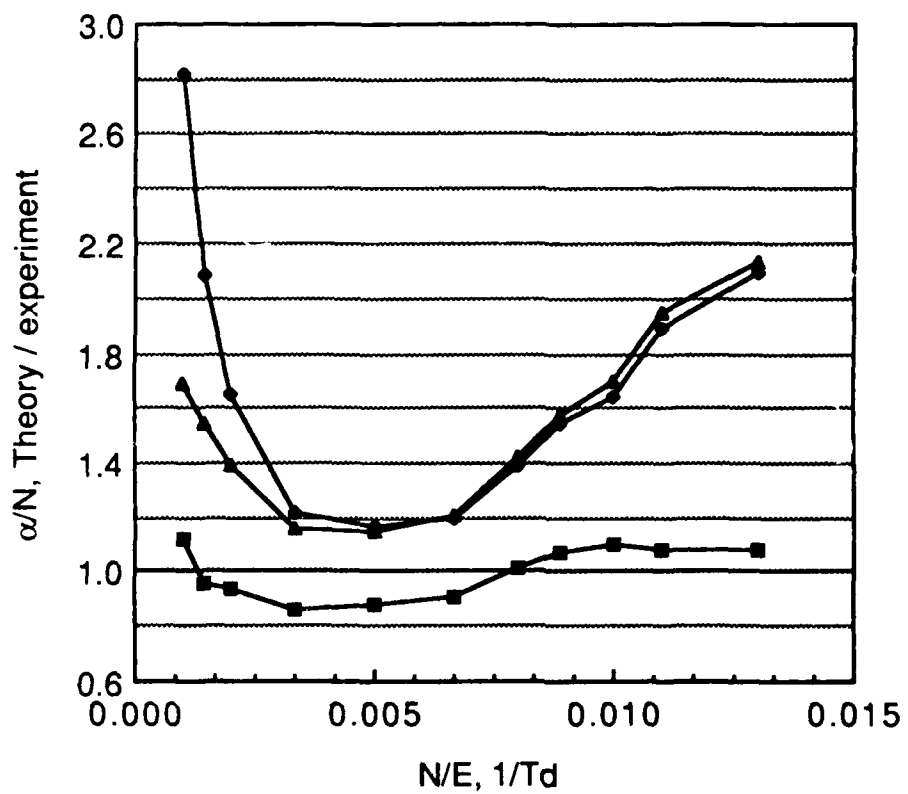


Figure 10. Ratio of the Monte Carlo and Boltzmann numerical predictions of the ionization coefficient as a function of E/N to the present measurements. The symbols are the same as in Figure 8.

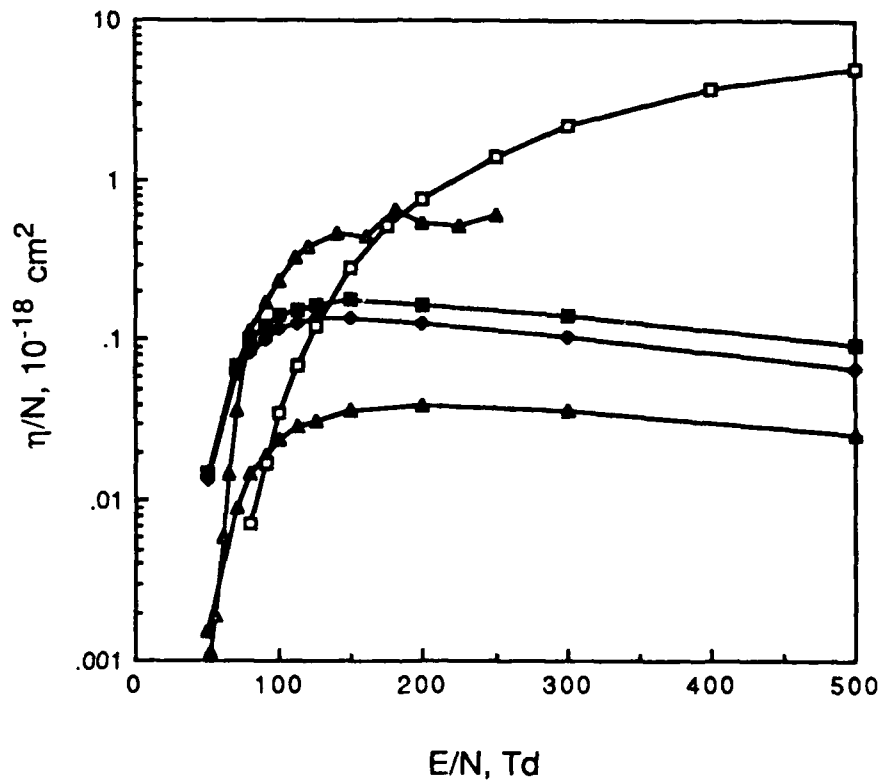


Figure 11. Comparison of the Monte Carlo numerical predictions of attachment coefficient for H^- (♦), CH_2^- (▲), and total (■) as a function of E/N with the estimated upper limit of the present measurements (□) and the previous data of Hunter et al. (△).

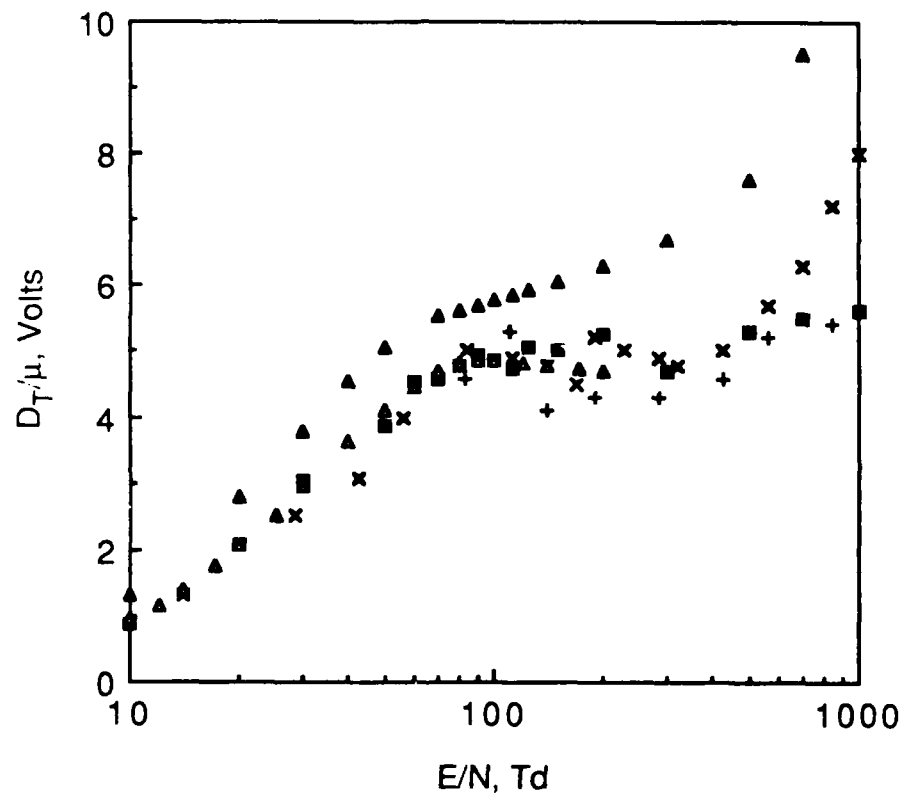


Figure 12. Comparison of the Monte Carlo (■) and Boltzmann (▲) numerical predictions of the ratio D_T/μ as a function of E/N with the previous measurements of Ref. 43 (×), Ref. 9 (+), and Ref. 44 (Δ). The data of Ref. 45 agree with those of Ref. 44 to within a few percent.

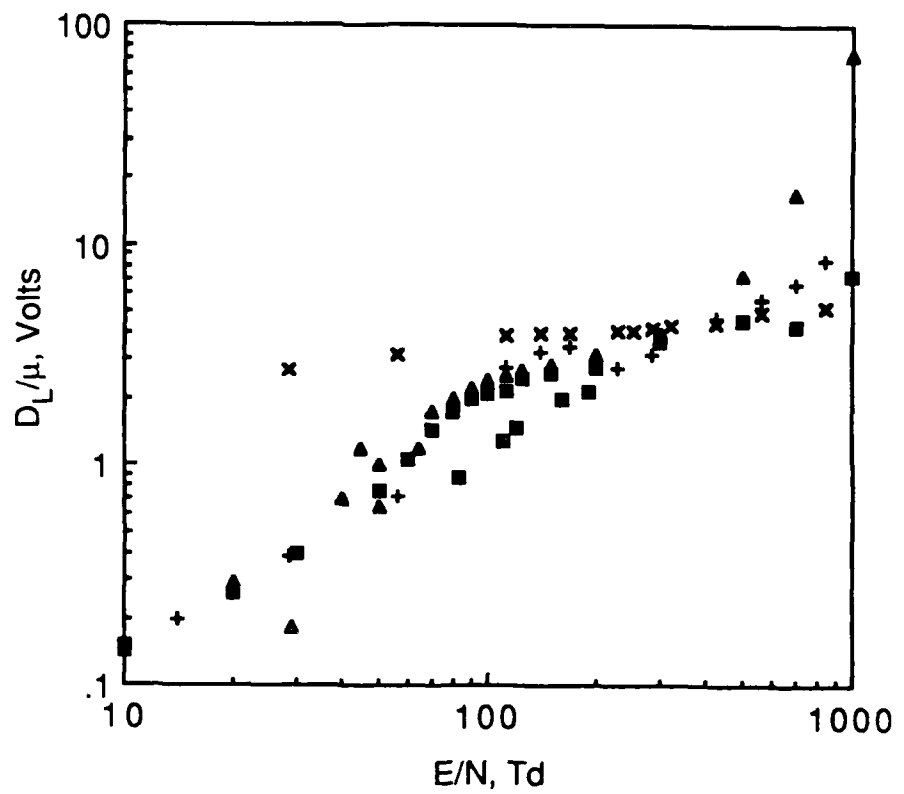


Figure 13. Comparison of the Monte Carlo (■) and Boltzmann (▲) numerical predictions of the ratio D_L/μ as a function of E/N with the previous measurements of Ref. 9 (+), Ref. 46 (Δ), Ref. 47 (x), and Ref. 48 (■).